A retinal imaging tool for assessment of the parapapillary atrophy and the optic disc

Cheng-Kai Lu

A thesis submitted for the degree of Doctor of Philosophy.
The University of Edinburgh.
January 2012

Abstract

Ophthalmic diseases such as glaucoma are associated with progressive changes in the structure of the optic disc (OD) and parapapillary atrophy (PPA). These structural changes may therefore have relevance to other systemic diseases. The size and location of OD and PPA can be used as registration landmarks for monitoring changes in features of the fundus of the eye. Retinal vessel evaluation, for example, can be used as a biomarker for the effects of multiple systemic diseases, or co-morbidities. This thesis presents the first computer-aided measuring tool that detects and quantifies the progression of PPA automatically on a 2D retinal fundus image in the presence of image noise. An automated segmentation system is described that can detect features of the optic nerve. Three novel approaches are explored that extract the PPA and OD region approximately from a 2D fundus image. The OD region is segmented using (i) a combination of active contour and morphological operations, (ii) a modified Chan-Vese algorithm and (iii) a combination of edge detection and ellipse fitting methods. The PPA region is identified from the presence of bright pixels in the temporal zone of the OD, and segmented using a sequence of techniques, including a modified Chan-Vese approach, thresholding, scanning filter and multi-seed region growing methods. The work demonstrates for the first time how the OD and PPA regions can be identified and quantified from 2D fundus images using a standard fundus camera.

Declaration of originality

I hereby declare that the research recorded in this thesis and the thesis itself was composed and originated entirely by myself in the School of Engineering at The University of Edinburgh.

Cheng-Kai Lu

Acknowledgements

I would like to express my deepest gratitude to all who have contributed to the completion of this thesis.

First of all, I would like to thank my supervisor, Professor. Alan F. Murray, for the guidance and invaluable suggestions he provided continuously during the period of my PhD study.

I would also like to thank Dr. Tong Boon Tang, for his great ideas, opinions and advice regarding the progress of my research.

A special thank goes to two medics who were in this collaborative project- Professor. Baljean Dhillon (Scotland) and Dr. Augustinus Laude (Singapore), for giving me access to their fundus image database. I would like to acknowledge the use of the LBC database and associated documentation in order to test my methods.

I thank my fellow research colleagues in the IMNS group for an interesting and rewarding experience during my PhD study. They are Zhijun Yang (China), Katherine Cameron (Scotland), Hugo Monteiro (Portugal), Thomas Koickal (India), Simeon A. Bamford (England), Shiwei Wang (China), Andrew Angus (Scotalnd), Andrew Cogman (England). I would like to express my gratitude to Zhuli Peng (China) and Miho (Japan) who has been incredibly supportive during the final stage of this work. Thanks you!!

Finally, I would like to thank my family members, grandparents, dad and mum, and my younger brother, Da-Wei Lu, for their encouragements and care over the years.

Contents

List of figures

List of tables

Acronyms and abbreviations

OD	Optic Disc
PPA	Parapapillary Atrophy
RPE	Retinal Pigment Epithelium
RNFL	Retinal Nerve Fibre Layer
HRT	Heidelberg Retina Tomography
OCT	Optical Coherence Tomography
LBC	Lothian Birth Cohort
ROI	Regions of Interest
PANDORA	Parapapillary atrophy AND Optic disc Regions Assessment
H.T.	Hough Transform
LSR	Least Square Regression
PCA	Principal component analysis
MM	Mathematical Morphology
UHR	Ultra High Resolution
TAN	Topological Active Nets
C-V	Chan Vese Snake
PAMELA	Pathological Myopia Detection Through Peripapillary Atrophy
SVM	Support Vector Machine
DCP	Distance to the Closest Point
MDCP	Mean Distance to the Closest Point
AF	Average Filter
MF	Median Filter
JSEG	J value SEGmentation
GVF	Gradient Vector Flow
MOCV	Morphological Operation and Chan-Vese
MULIPT	MULtiple Image Processing Techniques

Chapter 1
Introduction

1.1 Background and Motivation

This PhD study brings together optic disc (OD) and parapapillary atrophy (PPA) segmentation and quantification. The OD is the site where ganglion cell axons leave the eye to yield the optic nerve and the PPA is an abnormal retinal tissue, adjacent to the OD. As the focus is on developing a software system to deal with optic nerve features extraction, this section will provide a brief overview of image processing techniques on OD detection and segmentation and the need to pre-process. The research interests behind the investigation of the PPA region are also provided in this section.

1.1.1 Importance of undertaking detection and segmentation of the OD region

The 2D colour retinal fundus images not only provide information about different eye conditions and ophthalmic diseases (e.g. myopia, macular degeneration and glaucoma), but could also show signs of systemic diseases such as diabetes [3–6]. Hence, automated retinal fundus image processing has become a primary screening tool for early detection of ophthalmological and systemic diseases. In terms of analysis of the retinal image, optic nerve features (e.g. OD) are the fundamental features of interest. The segmentation of OD region is an essential task for the processing of retinal fundus images (i.e. automated measurements for diabetic retinopathy diagnosis or treatment evaluation). There are therefore abundant surveys about OD detection and segmentation reported in the literature.

The OD is located anatomically at the distal end of optic nerve (Figure 1.1), which is the region where ganglion cell axons exit the eye to form the optic nerve through which visual information is transmitted to the brain. The OD is the entry point for the main blood vessels that supply the retina. It is composed of two distinct parts: the cup, a central bright area of the OD, and the neuroretinal rim, a peripheral area where the nerve fibres bend into the cup region (Figure 1.2).

The OD region appears as a bright yellowish-white ellipse partially-overshadowed by retinal
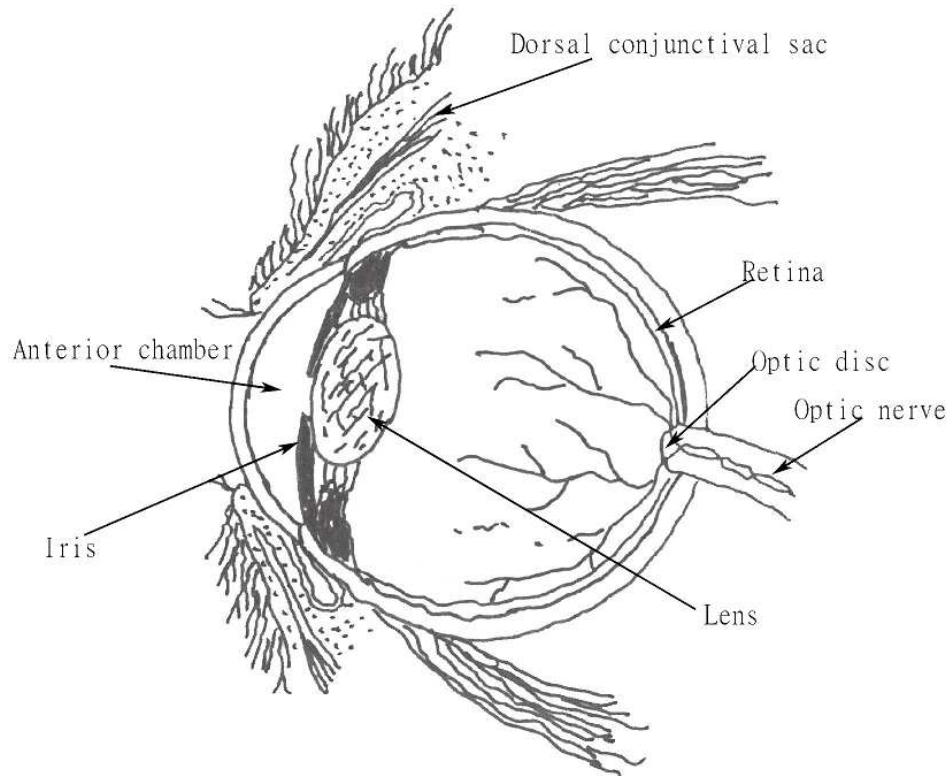
Figure 1.1: *The sagittal section of the eye ball. The optic disc is situated anatomically at the distal end of optic nerve.*

blood vessels in the fundus image. Segmenting the OD is not a trivial task owing to light artefacts, blood vessels and often ill-defined boundaries, particularly in the presence of PPA.

1.1.2   Growing Interest in the PPA region

Certain ophthalmic diseases (e.g. progressive glaucoma) and eye conditions (e.g. myopia) have been associated with the development of retinal pigment epithelium (RPE) PPA [3].

The reason why PPA develops has remained unclear but the progression of PPA, which is a result of degeneration in retinal nerve fibre layer (RNFL) in the eye, has been linked to degenerative myopia [7] as well as glaucoma [8], both of which can result in sight loss.

Although degeneration and thinning in retinal tissue are in general irreversible, early detection and medical intervention may offer an opportunity to reduce or limit their progression [9].
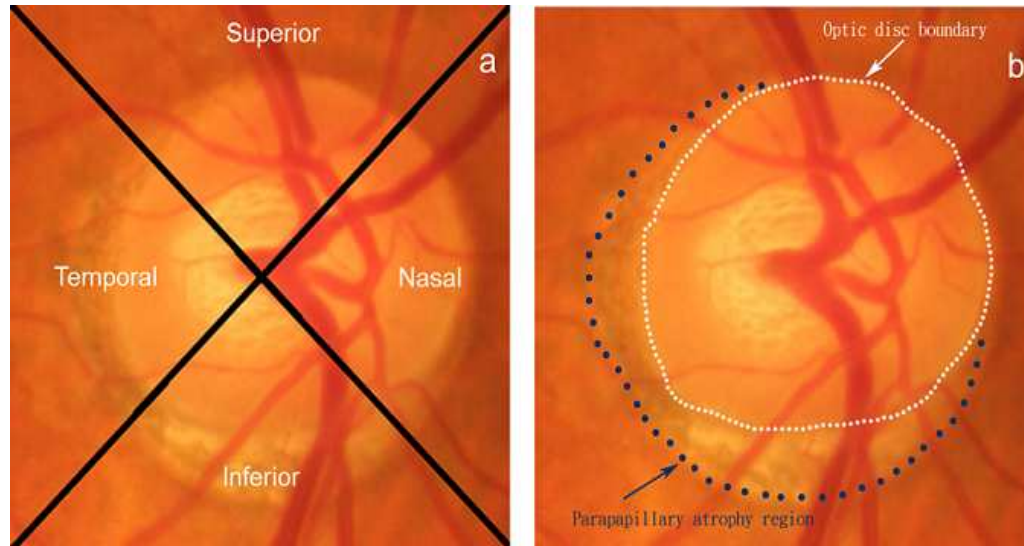
Figure 1.2: *a) Original colour retinal fundus image; Annotations describe the four different zones of the optic disc; b) the optic disc boundary and the ParaPapillary Atrophy region.*

More recently, there is therefore a growing interest in the potential role of PPA in detecting eye diseases at an early stage [10–16].

PPA can clinically be categorised into and the 'alpha' (α) zone and 'beta' (β) zone PPA and large choroidal vessels although the division is slightly artificial [17, 18]. α-zone PPA is the outer peripheral zone of PPA with irregular hyper-and hypo-pigmented areas in the retinal pigment epithelium (RPE), either on their own or surrounding zone β-PPA. In addition, β-zone PPA is the central zone of atrophy, next to the OD, is supposed to be complete RPE atrophy. Such kind of classification has now been accepted into common use, initiating studies to better understand the progression of the PPA. For example, the association between β-zone PPA with the rate of retinal nerve fibre layer (RNFL) thickness change has been studied. Glaucomatous eyes with β-zone PPA are at increased risk for progressive RNFL thinning [19]. The relationship between PPA and primary open-angle glaucoma with early focal visual field loss has also been investigated. Patients with such symptoms, and the patient with presence of β-zone PPA and neuroretinal rim thinning are in good correspondence [20]. Healey *et al.* investigated the association between β-PPA and both environment and genes. The presence of β-PPA appears to be under strong genetic control, with only a fraction of this genetic effect shared with genes involved in myopia [10]. The relationship between PPA and the OD in patients with glaucoma or visual field damage by manually quantifying the size of PPA and the OD regions has been investigated [11]. The presence and the progression of PPA were discovered to be associated

with subsequent OD or visual field changes in patients with ocular hypertension. Honrubia and Calonge further found that, in patients with such symptoms, the presence of PPA could imply a risk of glaucomatous deterioration as it has a statistical association with the presence of defects in the retinal nerve fibre layer (RNFL) [12].

The association of PPA with glaucoma in a population-based study has been studied by Xu *et al*. It has been found that β-PPA appears to be larger and occurs more frequently in glaucomatous eyes than in normal eyes of Chinese adults, but no significant difference was found between primary open angle glaucoma and closed angle glaucoma [13].

A commercial software package Photoshop (Adobe Systems Inc., San Jose, CA, USA) was utilised to measure the size of PPA and the OD regions in assessing how closely PPA is related to structural and functional glaucomatous optic nerve damage [14]. Uhm *et al.* discovered that the severity of glaucomatous optic nerve damage and visual field defects were related to the increases in the size of PPA and concluded that PPA could be useful for the diagnosis and progression of glaucomatous nerve damage [14]. There exist ophthalmic techniques such as the Heidelberg Retina Tomography (HRT) and Optical Coherence Tomography (OCT) which can provide a colourless or pseudo-colour 3D visualisation of the PPA and the OD [21]. They require a trained technician or ophthalmologist to identify manually the OD boundary on the image before the PPA and OD variables can be estimated from the image contour based on 3D depth information [15]. Furthermore, the HRT and the OCT have been employed in several studies about the PPA. One example application is to investigate the association between PPA and the progression of glaucoma [6]. However, 2D colour fundus imaging may be preferred by many clinicians for estimating the size of OD and PPA because the image from HRT or OCT is generated via computer processing rather than a direct recording of the object of interest.

An alternative tool to detect and quantify the PPA and the OD automatically from colour fundus images would reduce the workload of the human assessor and could facilitate a wider investigation about the potential importance of PPA in ophthalmic disease diagnosis involving facilities where access to HRT or OCT is limited. Moreover, in large clinical studies and pathological monitoring programs, such a computerised tool can also improve the repeatability therefore avoiding problems associated with fatigue and habituation, and tend to be more cost-effective.

1.2   Objective of this study

At its core, this thesis sets out to explore the suggestion that

An automated optic nerve feature detection and segmentation system based upon a combination of image processing techniques to emulate a human expert can approach the performance of the human visual system.

1.3   Definition of Problems

Many difficulties had to be overcome during this work. It is insufficient to estimate only OD positions and segmentation for the model based representation of the OD. It is necessary to fit the contours of the features so that important information, such as the transverse and conjugate diameter of OD, can be provided. These problems must be tackled under the assumption that the OD is an object with elliptical or with round shape. An approach to eliminating the influence resulting from the crossing blood vessels and the presence of PPA is also required. Three attempts based on a combination of image processing techniques have been proposed in this thesis to deal with these difficulties. In addition, PPA may have research value for ophthalmologists and researchers. It is therefore necessary to develop the software capable of both detecting and quantifying the region of PPA.

1.4   Fundus Image Database

All the colour fundus images for the assessment of the imaging tools we developed in this PhD project were randomly drawn from the database of the Lothian Birth Cohort (LBC) 1936 study [22]. The LBC study included the living members of the 1947 Scottish Mental Survey (n=70,805) who were born in 1936 and currently reside in the Edinburgh area (Lothian) of Scotland. Three hundred and twelve individuals were tracked successfully and had their retinal photos taken at the Wellcome Trust Clinical Research Facility, Western General Hospital, NHS Lothian, Scotland. Their mean age at the time of the photo-taking was 72 years old. The research complied with the Declaration of Helsinki and was approved by the Lothian (Scotland A) Research Ethics Committee.

5

The type of images in the LBC database is diverse. It comprises different types of shape of PPA (See Figure 1.3) so that the differentiation of different kinds of PPA could be considered in the trials executed by this PhD project.

1.4.1 Experimental protocols

Figure 1.4 illustrates the experimental protocols of developing software tools in this PhD project, which can be divided into four phases: Firstly, without knowing race and gender demographics, N fundus images were randomly drawn from the database of the LBC database by Cheng-Kai Lu. Here, N is a positive number. For the images used in Chapter 5, Chapter 6 and Chapter 7, N is given as 20, 94 and 50 respectively. All fundus images were first cropped manually to the Region of Interest (ROI), and the ROI size was set from 700×700 to 1200×1200. The ground truth were drawn by an ophthalmologist (Dr. Augustinus Laude, AL). The poor quality images were also determined by AL. Secondly, all algorithms described in this PhD project were invented and then implemented in MATLAB (Mathworks Inc., Natick, MA, USA). Thirdly, the software tools was modified according to analytic outcome (done by Cheng-Kai Lu) on unacceptable sample results which are determined by an ophthalmologist, AL. Lastly, the all segmentation results validated by different validation methods described in detail in Chapter 2, Chapter 5, Chapter 6 and Chapter 7, respectively.

1.5   Structure of the Thesis

The previous sections in Chapter 1 presented the aims of this thesis which include developing a software tool for automated detection and quantification of both the OD and PPA regions in 2D colour retinal fundus images. Related works on OD detection and segmentation that have been done in the past using active contour techniques and a few using Hugh Transform techniques have been discussed. There has been some work on the computer analysis on PPA detection and PPA segmentation because not much effort has been done on PPA detection and quantification.

Chapter 2 introduces and reviews (i) image processing techniques applied in OD detection and segmentation, (ii) a current approach to detect the presence of PPA and (iii) existing evaluation measures on the segmentation of optic nerves features.

Chapter 3 gives background information on some necessary image pre-processing techniques
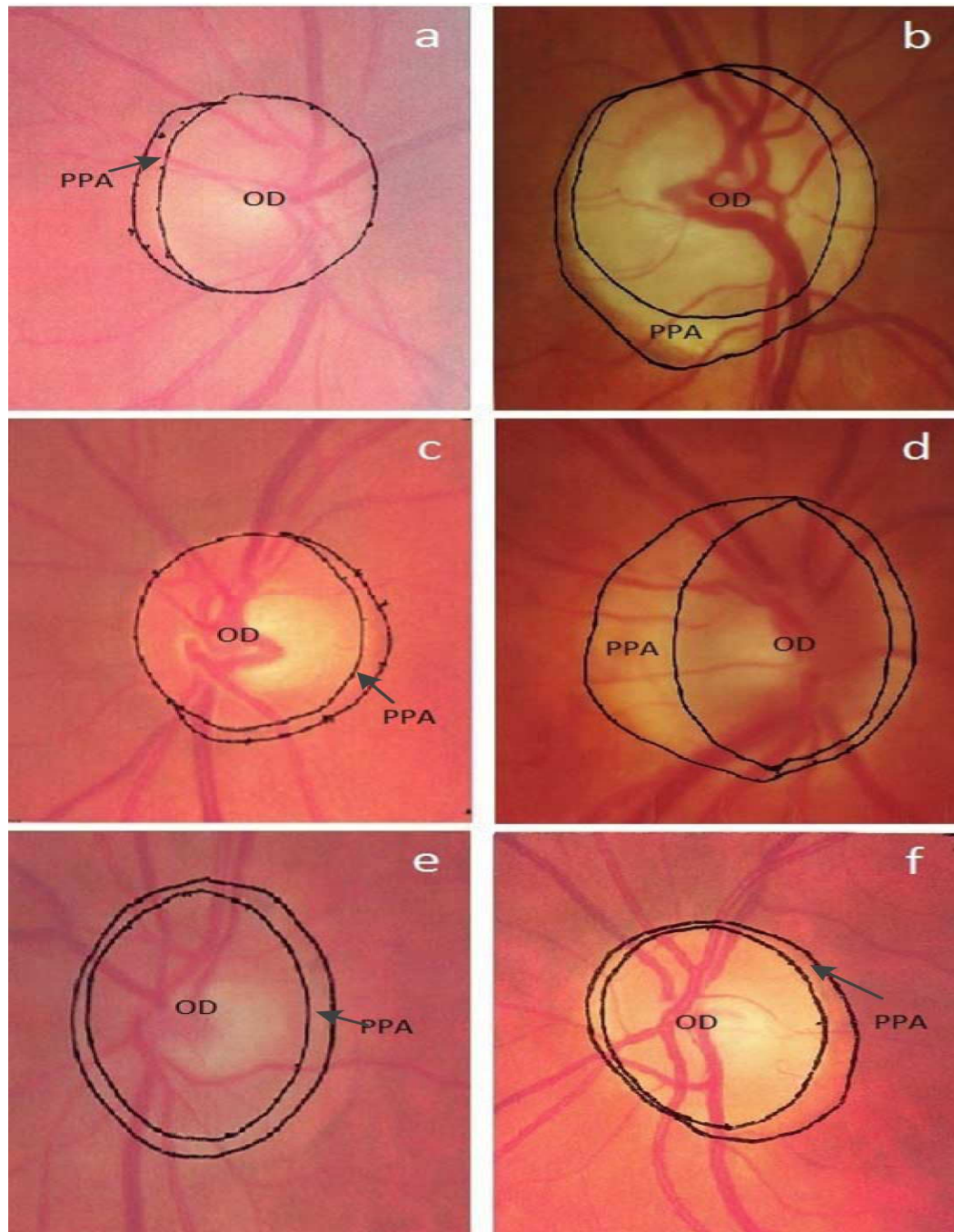
Figure 1.3: *Different types of PPA: (a) a right-eye image with a crescent shape PPA (b) and (c) shown a right- and left-eye image with a U-shape PPA, respectively (d), (e) and (f) shown a right-,left-,left-eye image with round shape PPA, respectively.*

N fundus images randomly selected

Images manually cropped to the Region of Interest (ROI)

Ground truths (G.T.) were drawn by an ophthalmologist

Phase 1: Image selection

Develop algorithms and implement the software tool for detection and segmentation of Optic Disc and Parapapillary atrophy

Phase 2: Algorithms invention and software tool implementation

Phase 3: Software tool modification

Samples of Segmentation results (S.S.R.)

S.S.R. vs. G.T. Acceptable or not ? (Determined by an ophthalmologist)

No

Analyse the reasons of unacceptable results

Segmentation Results vs. G.T.

Phase 4: Validation

Figure 1.4: *Experimental protocols of developing software tool for both detection and segmentation of the OD and PPA.*

and theories which are often used in bio-medical images. It is split into three main parts. The first part reviews the basic image processing theory such as Digital Image, Binary Morphological Operation, Image Filters and Colour Space and Colour Transform. The second part of Chapter 3 provides a quick look at image enhancement including contrast enhancement and histogram modification. The final part of this chapter introduces the edge detection techniques.

Chapter 4 gives a brief review of several image segmentation techniques including thresholding, region growing and active contours.

Chapter 5 describes the two different algorithms for the OD region segmentation in detail. A novel approach to segment the OD and PPA automatically is also introduced. The introduced method exploits both the red and blue channels of the image to maximise the information on features (PPA) whilst keeping interference (blood vessels) to a minimum. A technique named "snake without edges" is used to estimate the boundary of the OD and PPA. The proposed approach is evaluated against the reference boundary drawn by an ophthalmologist. Experimental results show the method can repeatedly detect the boundary automatically which is a major improvement from the results reported in the literature.

Chapter 6 describes a computer-aided measuring tool to automatically detect and quantify both the PPA and the OD regions in 2D colour fundus images of the retina. The outcome shows a possible means to quantify the size of PPA on 2D fundus image for the first time. The proposed tool is capable of detecting and quantifying PPA and OD regions repeatedly with sufficient accuracy and could also provide additional information, namely the transverse and conjugate diameter of the OD, which may be useful for eye screening purpose.

Chapter 7 describes a novel retinal imaging tool, Parapapillary atrophy AND Optic disc Regions Assessment (**PANDORA**), for assessment of the OD and PPA in detail. The tool is implemented by a combination of edge detection, ellipse fitting methods, modified Chan-Vese approach, thresholding, scanning filter and multi-seed region growing methods. The clinical-knowledge also has been exploited to develop this tool. The results show the developed system is more robust against various non-trivial conditions.

Chapter 8 first presents a summary of the achievement, then draws some limitations of the works and conclusions and eventually proposes several possible extensions of this research.

Chapter 2
Literature Review

This chapter aims to provide the essential background to this work and a review of relevant literature in order to identify a possible solution to the application. Firstly, Section 2.1 introduces the existing image processing techniques applied to optic disc (OD) detection and segmentation. Section 2.2 presents current solutions available for parapapillary atrophy (PPA) detection. This chapter is concluded with a survey evaluating the performance of methods of PPA detection and OD segmentation in Section 2.3.

2.1 Optic Disc (OD) Detection and Segmentation

The OD is an important parameter in glaucoma diagnosis [23, 24], very useful in proliferative diabetic retinopathy [25, 26] and a common landmark when locating regions of interest such as the macula [26, 27]. As a result, various methods have been investigated for the detection of the OD but the focus of those works is either to locate the centre of OD [28] or to detect the boundary of OD on fundus images without consideration for the conditions of PPA. The detection and segmentation of the OD region has been performed using 2D fundus images directly [28, 29] and 3D planimetric images generated from multi-modal imaging systems [30]. Figure 2.1 demonstrates the summary of the works of the detection of the OD. Normally, there are two/ three phases of the OD detection: pre-processing phase (noise reduction/ OD location), an estimation phase /and an optimisation phase.

Several methods reported in the literature are briefly introduced as follows:

2.1.1 Shape fitting based techniques

Shape or data fitting techniques (e.g. Hough Transform (H.T.) and least square regression (LSR)) are introduced to fit the OD because the OD is elliptical or round structure.

The traditional H.T. was designed to identify lines in the image, but later the H.T. has been extended to identifying circles or ellipses (Figure 2.2a). In the field of data fitting, the least-

Objectives   Used Features   Techniques

| Optic Disc centre detection |
| Retinal blood vessels information |
| Geometrical parametric model |

Techniques

Pre-processing   Estimates the OD   Estimated or Optimised the OD

| Morphological Operation |
| Pyramidal Techniques |
| Wavelet Transform |
| Histogram Equalisation |

Literature Review on Optic Disc detection works

Circular or elliptical fitting

Snakes

| Shape |

| Hough Transform |
| Least Square & Edge detection |
| Template matching |

| Chan-Vese and Level set methods |
| Traditional Snakes |

| Optic Disc boundary detection |

| High intensity variation | Clustering | 3D multi-modal image techniques |

| High intensity cluster | Local threshold |
| | PCA method |

Watershed

Figure 2.1: *Summarise the works of OD region detection and segmentation.*

squares minimise the sum of squared residuals to obtain the best fit. One data fitting example is given in Figure 2.2b.

(a) A result of fitting the OD region via Circular Hough Transform

(b) A result of data fitting via least square regression.
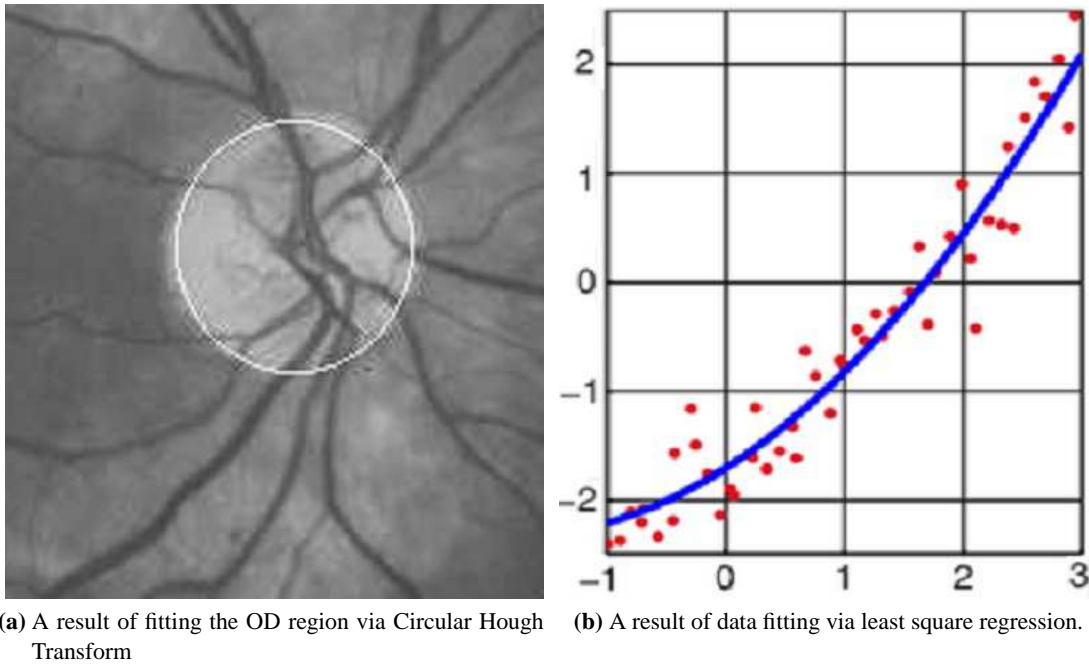
Figure 2.2: Samples of shape or data fitting based techniques.

In [31–33], an area-thresholding algorithm is used to firstly localise the OD, before detecting its boundary by the means of H.T., i.e. best fitting a circle based on the gradient information of the image. However, this approach proved to be time consuming.

In another investigation conducted by Abdel-Ghafar *et al.* [34], the green space of the retinal fundus image was suitable for the OD detection and segmentation because there is significant contrast between the OD and the retinal tissue in these images. In the pre-processing phase, a morphological closing operation removed the retinal blood vessels across the OD region. By estimating the OD centre, 24 evenly distributed radial vectors were then defined. The images were resampled along these 24 vectors to produce a representation for later processing. The Sobel operator (described in detail in Section 3.3.1) was applied first on these images and the threshold value was then obtained by computing the local variance and mean. Subsequently, the residual points were input to a Circular Hough Transform the biggest round shape was identified consistently with the corresponding OD. This method only applied on the images with less anatomical contrasts and only achieved at the success rate of 65% , with specificity and sensitivity rates of 84% and 60% respectively.

Figure 2.3: *An edge map resulting from applying Sobel edge on the OD region.*

On the other hand, the OD region detection is executed in the red channel in three phases: identification of candidate region, Sobel edge detection and an estimation phase. The candidate region is located and then neighbouring pixels are merged into clusters by a clustering algorithm [35]. The centre of the candidate region is regarded as the centre of gravity of the largest cluster. The edge detector, Sobel, is then used to estimate the contour of the OD (e.g. Figure 2.3). The outcome is not good enough because of noise. LSR is thereafter employed to determine the best circle that fits the OD region on the Sobel edge map.

2.1.2 Clustering and PCA based Techniques

The basic concept of a clustering technique is the approach of grouping a set of objects with similar features into clusters (shown in Figure 2.4). The OD can be detected either by finding a large cluster of pixels with high intensity [31, 36] or by searching a region with the most intensity variation at gray level [37, 38]. However such methods are susceptive to retinal lesions (e.g. exudates) which can also appear bright in fundus images and artefacts (e.g. intensity gradient across the image).

In addition, principal component analysis (PCA) is a mathematical procedure. Figure 2.5 il-
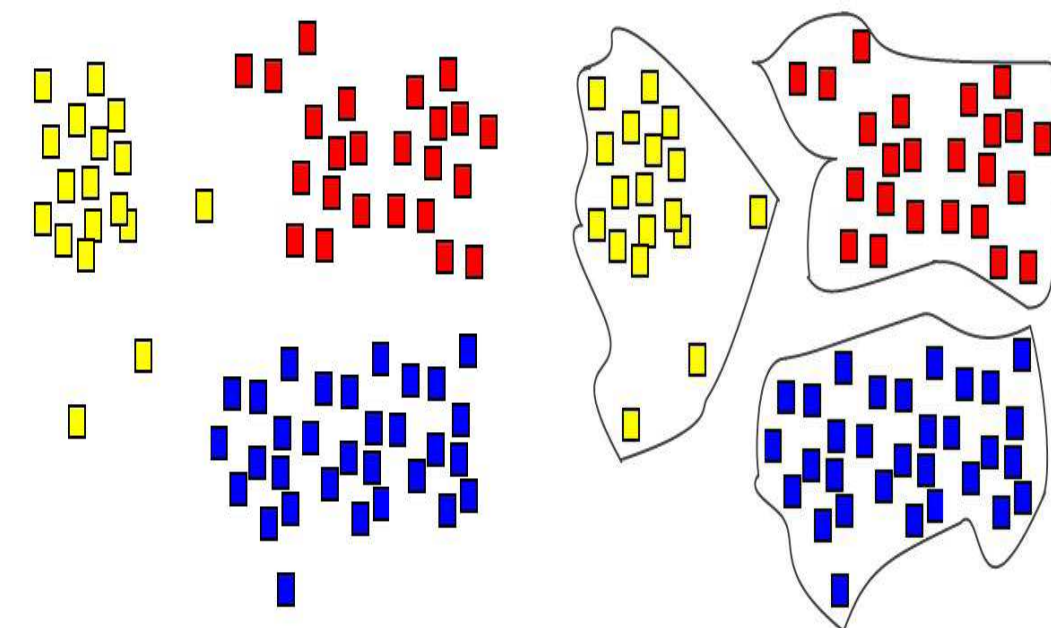
(a) Three different colour (red, yellow and blue) of the squares

(b) A result of the clustering technique.

Figure 2.4: *An example of a clustering technique shown as the colour (red, yellow and blue) of the squares into three groups.*

lustrates how to take a picture to capture the most information of the object. PCA can first find the longest axis (shown as a red line in Figure 2.5e). It then seeks the second longest axis (shown as a green line in Figure 2.5e) by rotating the teapot (e.g. Figure 2.5 a, b, c and d) as the longest axis is fixed. These two axes obtained are the first and the second principal component, respectively. The extends in average along the axes are called eigenvalues. Therefore, PCA can be applied to reduce the noise and get a significant feature of the data.

PCA for automatic detection of the OD region has been reported [39, 40]. The PCA, in their study, is employed only on the regions of pixels with the highest gray level to lock the OD. This method is applied with presence of large area of light lesions and could be used even in the presence of bright lesions on the fundus image, although this approach could also be time-consuming.

(a) Teapot.

(b) Top view of the teapot.

(c) Bottom view of the teapot.

(d) Side view of the teapot after rotation.
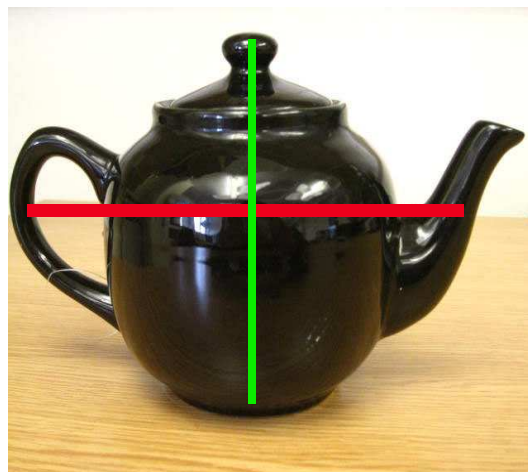
(e) Best view detected by PCA. PCA first find the longest axis depicted as red line and then the second longest axis (green line) is detected.

Figure 2.5: *Brief introduction of PCA.*

15

2.1.3   Pyramidal, wavelet transform and template matching Techniques

The contour information is essential to identify the macula precisely for successful grading of a pathological condition of the macula such as diabetic maculopathy. However, the extreme variation of the intensity within the OD or close to the OD boundary resulting from the presence of blood vessels and PPA increases the complexity of OD detection. The OD was tracked by a pyramidal decomposition (multi-scale analysis) technique exploiting a simple Haar-Based wavelet transform (shown in Figure 2.6) [28, 41] and its region was segmented by a Hausdorff-based template matching approach on an edge map obtained from a Canny edge detector. In their 40 trials of various visual quality [28], the OD centre positioning achieved an average error of 7%, with no false detection. Their proposed model could serve as a preparation stage for the task of segmenting of the OD.

Figure 2.6: *An example of pyramid representation of the fundus image, which is directly extracted from a paper. [1].*

In addition, the OD boundary detection rate was improved by using wavelet transform and an intensity-based template [42]. This method produces quite robust segmentation results in cases where the intensity of the OD region is extremely non-homogenous. The OD boundary is detected from the outline of the OD by using an ellipse fitting technique.

2.1.4 Geometric parametric model

The geometric relationship between retinal blood vessels across OD region and OD can be used to identify the location of OD [43–45]. The OD location can be utilised to initialise the disc boundary once it has been identified and the geometric features of retinal vessels can be used to locate the OD position (shown in Figure 2.7). For example, the origin of the retinal blood vessel network was determined by a novel algorithm using fuzzy convergence [43]. The coordinates of the OD centre were also estimated by using a geometrical parametric model [45].

(a) A fundus image.

(b) A result of vessel segmentation. The red cross denotes a candidate OD centre
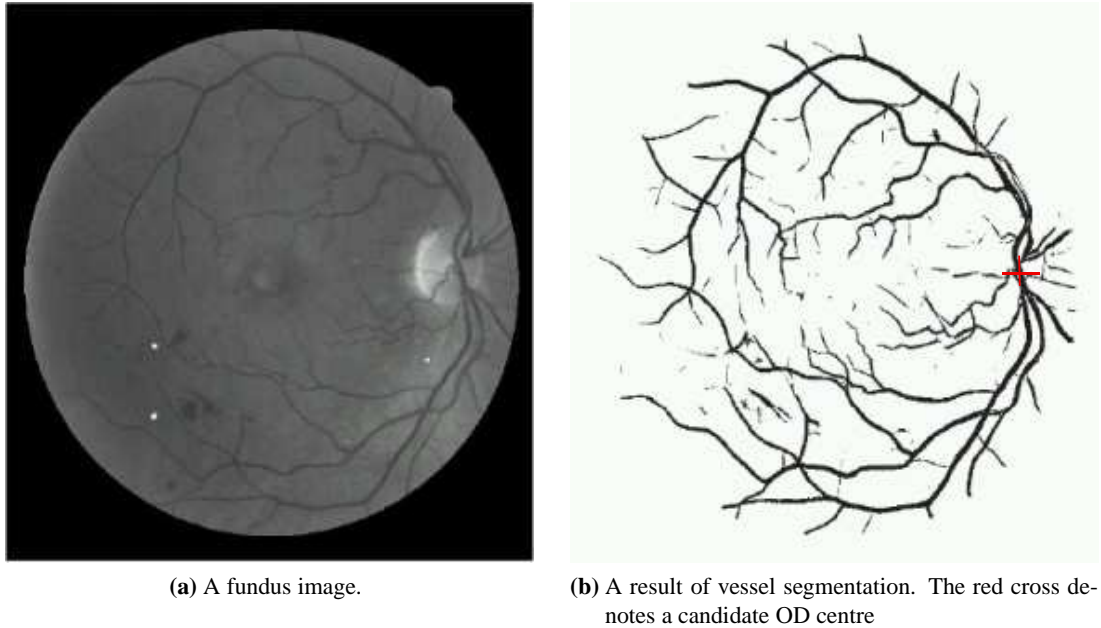
Figure 2.7: Geometric relationship between retinal blood vessels and OD centre.

In another attempt to locate the OD position, Trucco and Kamat [44] utilised a set of plausible candidates for main vessels, OD, and macula to search the space of possible triplets and then yield a proper location of the OD satisfying prior anatomical constraints. These approaches locate the OD with reasonable success although the detection of blood vessels is a very complex operation.

In addition, the direction of retinal vessels originating from the OD was depicted by a geometrical parametric model [46] and two parameters of the proposed model are just the coordinates of the OD centre. In the literature, Ruggeri *et al.* extracted retinal vessels by a vessel tracking procedure and then identified the model parameters by using a simulated annealing optimisation technique. The algorithm Ruggeri *et al.* proposed was employed in a set of forty images of

17

both abnormal and normal subjects. In all these images, the coordinates of the OD centre could be produced, even in rather severe pathological situations.

2.1.5 Watershed and morphological filtering

The morphological filtering (described in detail in Section 3.1.2) is a useful tool for noise reduction in shape-based image processing. The watershed transformation is often used as a regional image segmentation technique in a field of image processing and analysis. The fundamental concept of watershed is to simulate the flood drowned a rugged terrain gradually and the construction of dams to prevent the lake the process of merging. Figure 2.8 demonstrates the example of watershed segmentation. Original image and topographic view are shown in Figure 2.8a and Figure 2.8b, respectively. There are then three stages of flooding (Figure 2.8c, d and e). After merging process (Figure 2.8f and g), segmentation result shows in Figure 2.8h.

A combined approach of watershed transformation and morphological filtering to detect OD was developed by Walter *et al.* [47]. The proposed model achieves a mean sensitivity rate of 92.8% and a mean predictive rate of 92.4% in detecting the OD region. By altering the parameters of the model, the robustness of the model has been also evaluated. The results presented in the paper are encouraging, but obstructions such as retinal vessels are difficult to remove completely without introducing significant distortion and loss to the fundus image.

2.1.6 3D multi-modal image techniques

Several feasibility studies exist using Heidelberg Retina Tomography (HRT), Optical Coherence Tomography (OCT) and Ultra High Resolution (UHR) OCT can offer a pseudo-colour 3D multi-modal imaging systems of the PPA and OD [21, 30, 48, 49].

Although these techniques achieved reasonable success, they still have four main limitations [50]. Firstly, these techniques are not widely used in ophthalmology clinics because they operate with more expensive and specialised lasers [51, 52]. Secondly, trained technicians or photographers with an intimate understanding of retinal anatomy are required for operating OCT properly and acquiring a high enough quality OCT image. Thirdly, the patient has to be turned to a particular direction to aim the instrument at the right place and then has to remain motionless for a long time waiting for the scanning line procedures executed by OCT, in order to avoid artifacts resulting from eye movement. Fourthly, they are probably not good for visualising changes in

(a) Original image.

(b) Topographic view of the image.

(c) First stages of flooding.

(d) Second stages of flooding.

(e) Third stages of flooding.

(f) Merging of water from two catchment basins.

(g) Result of further merging.

(h) Segmentation result (lines).
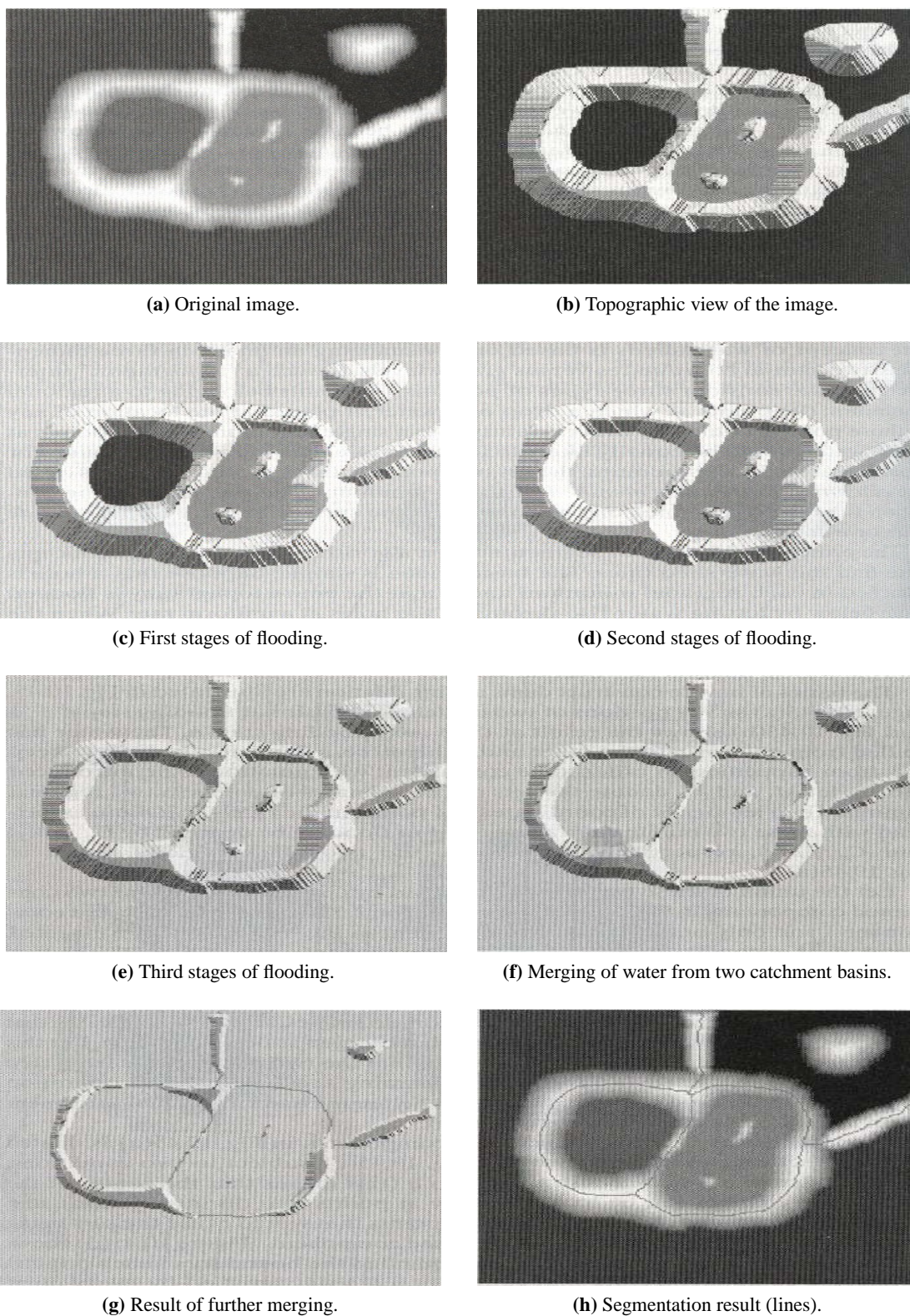
Figure 2.8: *An example of watershed segmentation. (a) original image (b) topographic view of the image. (c), (d) and (e) are then three stages of flooding. After merging process shown in (f) and (g), (h) shows the segmentation result.*

19

(a)   (b)   (c)
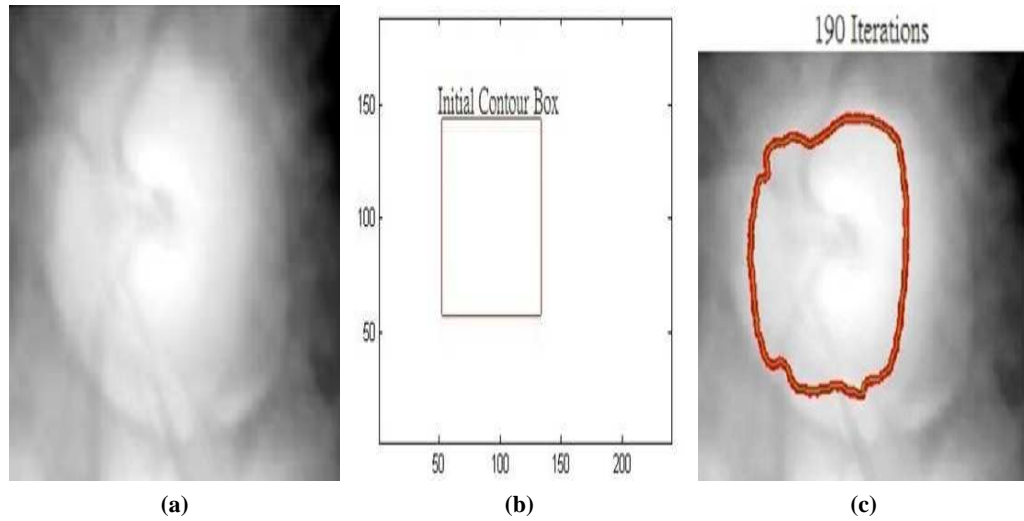
Figure 2.9: *A Sample of working process of the snake: (a) Input image; (b) Giving initial contour; (c) An example of the OD boundary detection after 190 iterations.*

disease progression. For example, the existing software for OCT would not allow clients to view the acquired images from the previous examinations with the current image on the screen immediately. Moreover, it is unlikely that such an expensive solution built around OCT instruments would be adopted for a large-scale screening program [52]. In addition to this, this approach requires a trained technician or ophthalmologist to identify the OD boundary manually on the image before the PPA and OD variables can be estimated from the image contour according to 3D depth information [15, 52].

2.1.7   Active Contour (Snake) based techniques

The active Contour is a deformable image segmentation model which evolves like snake (described in detail in Section 4.4). In practice, active contours normally starts after given an initial contour. Figure 2.9 gives an example of using snakes to estimate the OD region.

In this sub-section, several snake based techniques to detect and segment the OD region reported in the literature are stated as follows.

First, histogram equalisation (described in detail in Section 3.2.2) was applied to enhance the retinal images. Pre-processing was then implemented by using a pyramid edge detector to the contrast enhanced image. After that the pixels of the pyramid data structure were averaged by

4-pixels subgroups improving the noise resistance. The edge strength and Cholesky algorithm [1] were used to fit a snake to the OD border. The success of this model is very contingent upon pre-processing the images to improve the contrast between the OD and the retina, but locking the snake onto the OD border in the upper right quadrant was unsuccessful in their trials.

Second, PCA is utilised to locate the OD by means of detecting the candidate regions at various scales. The centre of the OD could be indicated by calculating the minimum distance between the fundus image and its projection onto disc space. The Hough transform was therefore adopted for the round shape detection because the shape of the OD is a round or elliptical structure [53]. The centre and radius of a circle estimated by the margin of OD after using the Hough transform detection. In addition, Topological Active Nets (TAN) was proposed by Novo *et al.* [54] to segment the OD region. This is a deformable model which could describe the inner topology of the targeted object boundaries. Both active nets, optimised by a genetic algorithm and energy term, have been applied to segment the OD, without any pre-processing of the image.

Third, both the application of morphological operations and the automatic initialisation of the active contour in Lab colour space were exploited to locate the OD region in a retinal image [55]. Previously reported work in the literature was focused on detecting the centre of the OD region [38]. Osareh *et al.* [55], removed retinal blood vessels by means of colour morphology and used template matching to initialise the OD margin automatically. It is almost impossible to remove retinal blood vessels completely, although the morphology pre-processing (e.g. opening/closing) helps to diminish the effects of retinal blood vessels. In addition, the snake can deform to the wrong place if the initial mask for snake is far from the disc margin. Moreover, such processing blurs the OD boundary, making the boundary detection unreliable.

Fourth, in [37], Xu *et al.* proposed a deformable model based technique to estimate the OD boundary in retinal fundus images. They improved and extended the original snake by clustering and smoothing update techniques. The OD boundary points are first self-classified into two groups, edge point group or uncertain point group, via clustering techniques after every snake evolution. These boundary points of the OD are then automatically updated by different criteria obtained both from the global and local information. This approach works well, but only if there is no or very little PPA. The presence of the PPA complicates the detection of the

OD as it also appears bright in the fundus images.

Fifth, Chan-Vese (C-V) method [56] and level set methods [57] have also been applied to OD boundary segmentation. The main merit of these methods is their ability to compensate for discontinuities in the targeted region boundary of image features to be located. These approaches however suffers from major drawbacks, e.g. the segmentation process is likely to be time-consuming, C-V requires an accurate initial "guess" of the OD boundary and it is likely to achieve good results only when the OD region is of homogenous intensity.

Sixth, stereo imaging techniques have also been exploited using a "Snake" algorithm, together with p-tile thresholding on an edge map, to outline the OD boundary [58]. This method was implemented via 80 retinal image pairs, including 55 non-glaucomatous, and 25 glaucomatous eyes. The OD was estimated via the snake with the information of the edge and brightness. Their proposed method was then tested on a new set of stereo images which consisted of 98 pairs including 60 and 30 pairs with and without signs of glaucoma, respectively. The testing result shows the potential value of the automated estimation of the OD region. The presence of PPA however remains a problem. One possible solution is to pre-determine the presence of PPA and subsequently devise a corresponding strategy to segment the OD region.

2.2 Parapapillary Atrophy (PPA) Detection

PPA is one of the optic nerve features, which has been associated to eye conditions or diseases (e.g. myopia and glaucoma). It is important to detect ophthalmic diseases early in order to take potential interventional measures. However, previous studies were limited to the detection of PPA. Most existing methods for the detection and quantification of PPA are subjective and manual [6, 10].

Only one software tool PAMELA (Pathological Myopia Detection Through Peripapillary Atrophy) has been developed to automatically evaluate 2D fundus image of pathological myopia [7, 59]. It utilises the texture analysis component of PAMELA and clinical image context to extract PPA features and applies an artificial neural network known as a Support Vector Machine (SVM) to perform binary classification (e.g. PPA present or not). This system involves segmentation of the OD, generation of texture features, integration of these features

into clinically-relevant zones, and a SVM classifier trained for classification on the detection of PPA. The presence of PPA is detected with 87.5% accuracy in 40 images from the Singapore Eye Research Institute. The sensitivity and specificity of PPA detection are 0.85 and 0.90 respectively.

Their results show good promise for PAMELA; however, their system has the following drawbacks: Firstly, both the accuracy of the OD detection and segmentation need to be improved. Secondly, the system can only detect certain types of PPA so that the differentiation of different kinds of PPA has to be considered in this system. Thirdly, their proposed system can not quantify the extent and hence describe the development of PPA.

2.3 Evaluation Measures reported in the literature

There are two main issues that fall into the scope of this project: to establish and implement methods to determine the presence of PPA, and further to quantify the area of PPA and OD. Therefore, in this section we briefly introduce the evaluation measures (either for evaluating detection or for evaluating segmentation): Firstly, we introduce the rules for evaluating the performance of detection. Mean accuracy, Specificity and Sensitivity have been adopted to evaluate the performance of PPA detection [7, 59]. The Specificity, defined as the number of true negatives divided by the sum of false positives and true negatives indicates how well a tool can correctly identify negatives. The Sensitivity, defined as the number of true positives divided by the sum of false negatives and true positives indicates how well a tool can identify actual positives. In terms of area estimation, several existing evaluation methods for assessing the overall performance of the OD region segmentation are reported in the literature. These evaluation methods are based on the similarity either in the estimated boundary or in the estimated area when compared to a "groundtruth" drawn by a human expert.

Segment of detected contour against the segment of contour of the groundtruth drawn by human experts

The boundary-based estimation can be evaluated by measuring the distance between two closed boundary curves. This helps evaluate the accuracy of targeted object contour localisation. Therefore, this method has been used to measure the average distance from the estimated OD contour point to the ground estimate [37]. $\widehat{s}(n)=[u(n),v(n)]$ denotes the final estimated contour, $1 \leq n \leq N$. The ground estimate, represented by A, is comprise of an individual pixel a_i, 1

$\leq i \leq M$, where M denotes the amount of the pixel on the ground estimate contour. For each individual contour point n of all points N of the contour, the distance to the closest point (DCP) of ground estimate is defined as

$$DCP(\widehat{s}(n), A) = min \parallel \widehat{s}(n) - a_i \parallel, \ 1 \leq i \leq M \tag{2.1}$$

The accuracy of the estimated contour is assessed by the Mean Distance to the Closest Point (MDCP) shown as follows:

$$MDCP(\widehat{s}, A) = \frac{1}{N} \sum_{n=1}^{N} DCP(\widehat{s}(n), A) \tag{2.2}$$

By definition, the smaller the MDCP is, the closer the computed contour is to the ground estimate.

Segmented region against the region of groundtruth drawn by human experts

An effective measure (M) of the match between estimated region and groundtruth region has been adopted by Osareh *et al.* [55]:

$$M = \frac{N(R \cap T)}{N(R \cup T)} \tag{2.3}$$

here R and T are equivalent to the ground estimate and the detected OD region respectively and *N(.)* represents the number of pixels in the targeted object region.

In addition, Joshi *et al.* [52] further compute the pixel-wise recall and precision values from the overlap area between the ground estimate and the computed region. These are defined as:

$$Recall = \frac{tp}{tp + fn} \tag{2.4}$$

$$Precision = \frac{tp}{tp + fp} \tag{2.5}$$

here *tp* denotes the number of true positive pixels, *fn* denotes the number of false negative pixels

and *fp* denotes the number of false positive pixels.

$$F = 2\frac{Recall \times Precision}{Recall + Precision} \tag{2.6}$$

where F(namely traditional F-score or F_1 score) denotes the harmonic mean of recall and precision. Here, the F-score value lies between 0 and 1. Here, the higher F-score is, the more accurate mode is to the ground estimate.

2.4 Chapter Summary

In this chapter, some techniques surrounding OD centre localisation, OD region detection and segmentation reported in the literature are presented initially. These techniques are based upon features of the OD region (e.g. the region with large cluster of high intensity, the region with most intensity variation and texture information) or using geometrical features of retinal vessels across the OD region. In Section 2.2, the software tool, PAMELA, using SVM and texture information for PPA detection is reviewed. The PPA detection rate of PAMELA is 87.5% with a sensitivity and specificity of 0.85 and 0.9, respectively. The experimental results were reasonable; however, the tool Liu *et al.* developed can only detect a few types of PPA and it can not describe the progression of the PPA region. In Section 2.3, one statistical analysis is performed to assess the performance of PPA detection and three common evaluation measures (including contour to contour, region to region and F-score) for PPA or OD region detection or OD region segmentation are introduced.

Chapter 3
Review of Major Image Pre-processing Techniques

Image pre-processing is an essential step because segmentation of bio-medical images is an arduous task often complicated by sampling artefacts and noise. It is highly recommended to understand them before moving onto advanced methods and new ideas. A number of necessary image processing techniques and theories which are commonly mentioned and adopted in this thesis are introduced briefly in this chapter.

3.1 Basic Theory of Image Pre-processing Techniques

3.1.1 Digital Image

The term digital image normally refers to raster image, or bitmap, which is composed of a set of numeric data structures or pixels. It is technically depicted by the width and height of the image in pixels and by the number of bits per pixel. Pixels are the smallest individual element in an image, indicating quantised values that represent the brightness of a given colour (or intensity for grayscale) at any specific point. For example, an 8-bit grayscale image denotes that each pixel of the image can have one of 256 shades, from the lowest (black) to highest (white) intensity value. It is essential to provide three colour channels for each pixel for visually acceptable results. Each colour channel resembles a grayscale image, offering shades of the colour. The blend of three channels leads to the colour of the pixel, which can be constructed as coordinates in some colour space. The colour space and its transformation will be discussed later in this section.

3.1.2 Binary Morphological Operation

The morphological operation is an essential tool for shape-based image processing, particularly for filtering purposes. Therefore, we introduce it here briefly. For a general scientific perspective, the term morphology refers to the study of structures and forms. Applying this concept

to image processing, morphological image processing is usually called mathematical morphology (MM), which is the name of a specific methodology for analysing the geometric structure inherent within an image. The MM was initially developed for "binary" images, and was then extended to gray-scale images and functions.

In binary morphology, an image is regarded as a subset of the integer grid ($\mathbf{Z}^d$) or a Euclidean space ($\mathbf{R}^d$), for some dimension d. The fundamental concept in binary morphology is the use of a simple "structuring element" (also known as a kernel) to investigate if a predefined shape fits or misses the shapes found in an image. Two examples of commonly used kernels, marked as $\boldsymbol{B}$, are shown as follows:

A. Let $E=Z^2$; $\boldsymbol{B}$ is a 3x3 square defined by: $\boldsymbol{B}$=(-1,-1), (-1,0), (-1,1), (0,-1), (0,0), (0,1), (1,-1), (1,0), (1,1) (shown as in Figure 3.1a).
B. Let $E=Z^2$; $\boldsymbol{B}$ is a cross defined by: $\boldsymbol{B}$ =(-1,0), (0,-1), (0,0), (0,1), (1,0) (shown as in Figure 3.1b).

(-1,1)　(0,1)　(1,1)　　　　(0,1)

(-1,0)　(0,0)　(1,0)　　(-1,0)　(0,0)　(1,0)

(-1,-1)　(0,-1)　(1,-1)　　　　(0,-1)

(a) A common used square kernel.　　　　**(b)** A common used cross kernel.
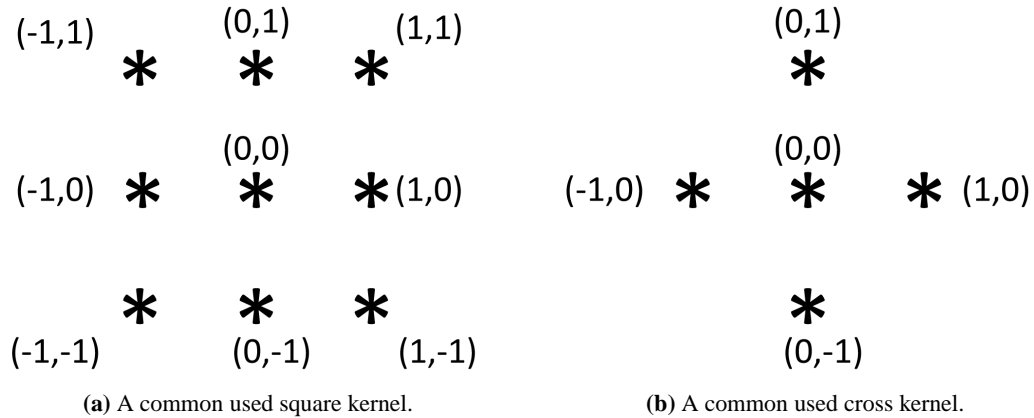
Figure 3.1: *Samples of common used kernels. Grid point $*$ denotes "1".*

There are four key binary morphology operators [60]: erosion, dilation, closing and opening. In a binary image, erosion "thins" the black pixels and dilation "smears" the black pixels (as shown in Figure 3.2). These two basic operators are mutually coupled as an erosion of the black pixels is equivalent to a dilation of the white pixels. In addition, they are translation invariant and strongly related to Minkowski addition.

a) Erosion (See Figure 3.2b)

27
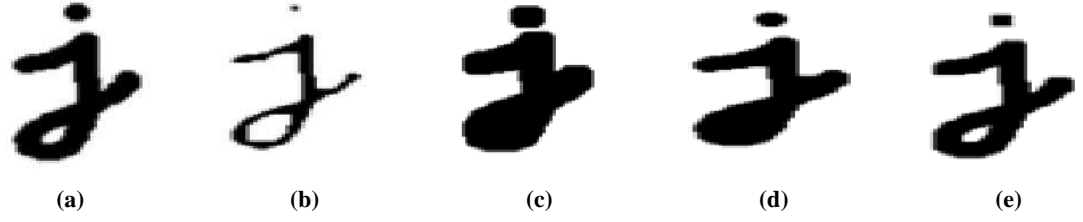
Figure 3.2: *Samples of executing binary image morphology: (a) original image; (b) erosion; (c) dilation; (d) closing; (e) opening.*

Let E be ($\mathbf{Z}^d$) or ($\mathbf{R}^d$), and A represents a binary image in E. Erosion operator is given by:

$$A \odot B = \{z\epsilon E | B_z \subseteq A\} \qquad (3.1)$$

Where (B^z) is the translation of B by the vector z, for example:

$$B_z = \{b + z | b\epsilon B\}, \forall_z \epsilon E \qquad (3.2)$$

When the kernel B has a centre (e.g. B is a square or a disk), and this centre is located on the origin of E, then the erosion of A by B can be comprehended as the locus of points achieved by the centre of B when B moves inside A.

b) Dilation (See Figure 3.2c)

Dilation operator, the opposite of the erosion operator, of A by the kernel B is given by:

$$A \oplus B = \bigcup_{b\epsilon B} A_b = B \oplus A = \bigcup_{a\epsilon A} B_a \qquad (3.3)$$

If B has a centre on the origin, then the dilation operator of A by B can be comprehended as the locus of the points covered by B when the centre of B moves inside A.

c) Closing (See Figure 3.2d)

The closing of A by B starts with a dilation operator of A by B, followed by an erosion operator of the resulting structure by B:

$$A \bullet B = (A \oplus B) \ominus B \tag{3.4}$$

The closing operator is also the complement of the locus of translations of the symmetric of the kernel outside the image *A*. Therefore, the closing operator can also be derived from $A \bullet B = (A^C \circ B^C)^C$, where X^c denotes the complement of *X* relative to *E*.

d) Opening (See Figure 3.2e)

The opening of *A* by *B* is acquired from the erosion operator of *A* by *B*, followed by dilation operator of the resulting image by *B*, therefore the mathematical equation is represented as follows:

$$A \circ B = (A \ominus B) \oplus B \tag{3.5}$$

The opening operator is also defined by

$$A \circ B = \bigcup_{B_x \epsilon A} B_x \tag{3.6}$$

which means that it is the locus of translations of the kernel *B* inside the image *A*.

Binary image morphology (shown in Figure 3.2): (a) original image; (b) erosion; (c) dilation; (d) closing; (e) opening. The kernel for all examples is a 7 ×7 square. Due to the different sequence of basic morphological operations, the void in the lower part of the character '*j*' remains clear after opening but is filled with dark pixels by closing.

3.1.3 Image Filters

Image filtering allows one to emphasise certain features or remove adverse effects on images [60]. A few types of image filtering are described here; all using a 2D filter.

Average and Median Filters

Both the Average Filter (AF) and the Median Filter (MF) can be employed in eliminating noise

from an image. An AF is a filter of linear class that can smooth an image. The basic concept behind the filter is that for any element of the image, an average of the current pixel and its neighbourhood is computed. The MF does something similar, but, instead of computing the average, it takes the median.

| (a) Original image | (b) Original image with added salt and pepper noise |
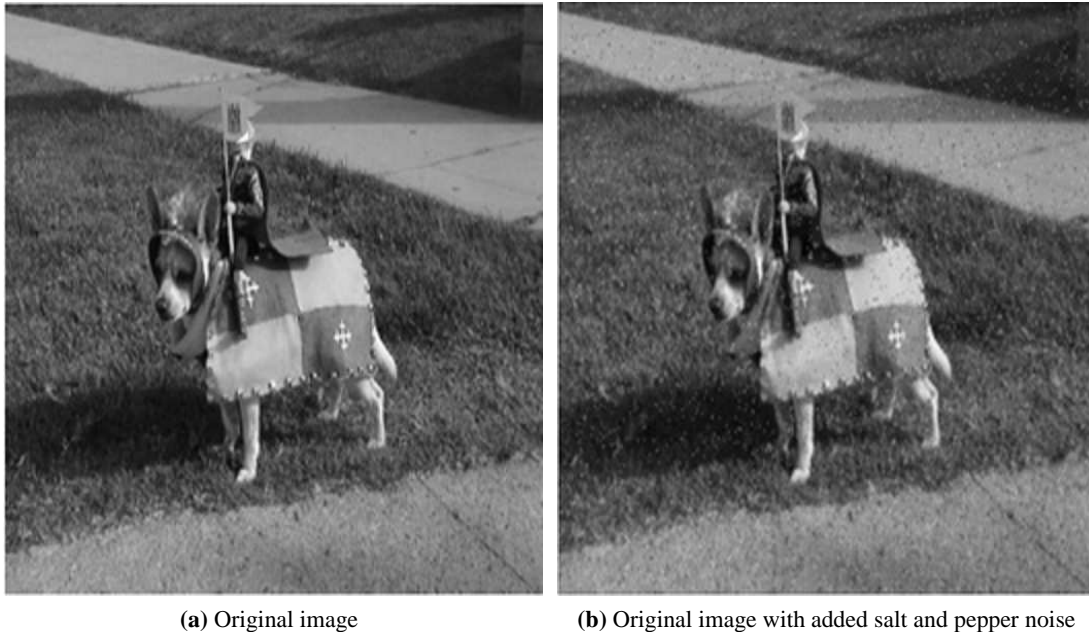
Figure 3.3: Samples for image filtering.

The median is acquired by sequencing all the values from low to high, and then selecting the value in the centre. If there are two values in the centre, the average of these two is calculated. In order to demonstrate the difference between these two filters, salt and pepper noise, a random white and black pixels noise, was added to an original image (shown as in Figure 3.3). A MF gives a better result as salt and pepper noise is completely eliminated (shown as in Figure 3.4). With an average filter, the colour values of all noisy pixels are taken into consideration in the mean calculation. In contrast, when taking the median, you only select the colour value of one or two pixels which have the least random fluctuations; however, similar to the AF, the median filter might blur the object boundary.

Linear filter with convolution

The image filter with convolution is another commonly-used filter. The convolution is a neighbourhood operation in which each output pixel is the weighted sum of neighbouring input pixels. The convolution kernel here is the matrix of weights. To compute the output pixels, the
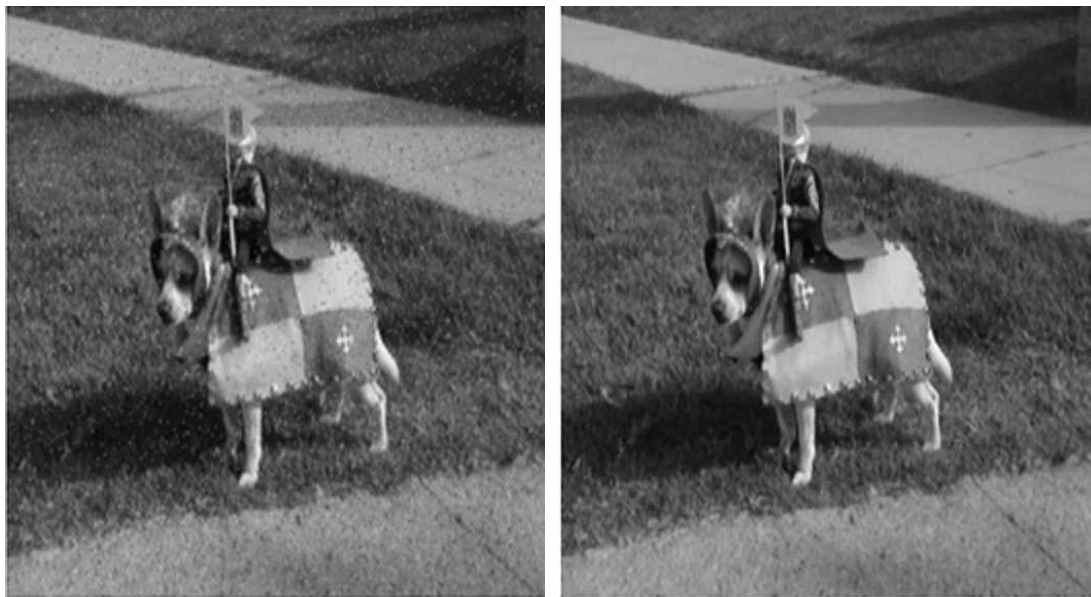
(a) The image after average filtering   (b) The salt and pepper noise has been removed after performing median filtering.

Figure 3.4: Results both for average filtering and median filtering.

convolution kernel is first rotated 180 about its centre element, then each weight in the rotated convolution kernel is multiplied with the pixel of the image and the products are summed together, as we scan the rotated convolution kernel over the entire image. An example application of a convolution filter to blur the image is shown in Figure 3.5.

3.1.4   Colour Space and Colour Transform

The basic colour channel used in medical image processing is R-G-B 3D colour space (Red, Green and Blue Channel). It is composed of primary colours - Red, Green, and Blue which are illustrated as x-, y- and z- axes of the space respectively (see Figure 3.6). All the colours in this space are found as points on or inside the colour cube, which are yielded by combining a different proportion of Red, Green and Blue. RGB colour space has two main drawbacks although it is a simple way to produce colour.

First, human eyes are psychologically more sensitive to one primary colour than another and therefore the representation of RGB space is not consistent with human perception. Second, any changes in an individual channel will result in the modification both in intensity of the channel and in the resultant colour.

(a) Original image   **(b)** The image after processing convolution filtering. The convolution filter blurs and smooths the image.

Figure 3.5: *Samples for convolution filtering.*

For the aforementioned reasons, many other colour spaces have been developed, (e.g. YIQ, CIELAB, CMY, CMYK and HSV), to suit specific applications. Among these, HSV and CIELAB space are the two most common used colour spaces in the thesis, alongside RGB.

The HSV (Hue, Saturation and Value) colour space consists of three elements:

Hue is a colour type that describes a pure colour (e.g. pure yellow, orange, or red), ranging from 0 to 360 degrees on a hue circle (also known as the colour wheel). Saturation, also called purity, varies from 0 up to 1 (or 0 to 100%) to which the lower value means more "grayness" presented. Value, also called Brightness, ranges from 0 up to 1 (or 0 to 100%), which is a nonlinear transformation of RGB colour space.

The utilisation of hue and saturation channels makes the representation of HSV space more closely associated with the way humans perceive colour relationships.

Figure 3.7 shows HSV space as a single cone. A 3D conical formation of the colour wheel represents the hue space. Three primary colours split the wheel equally, with Red at 0 degree,
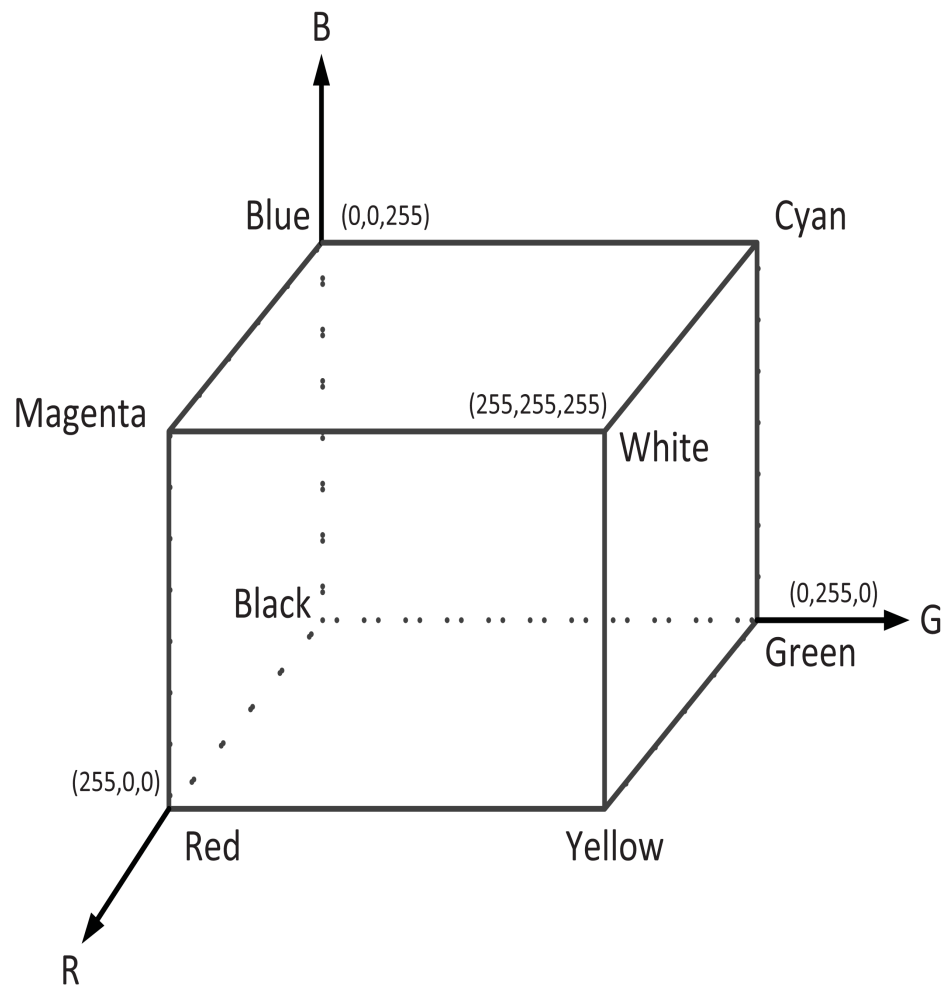
Figure 3.6: *RGB colour space cube.*

Green at 120 degree, Blue at 240 degree and so on. In addition, the saturation and the value are depicted by the distance from the centre of a round cross-section of the cone and the distance from the pointed end of the cone, respectively.
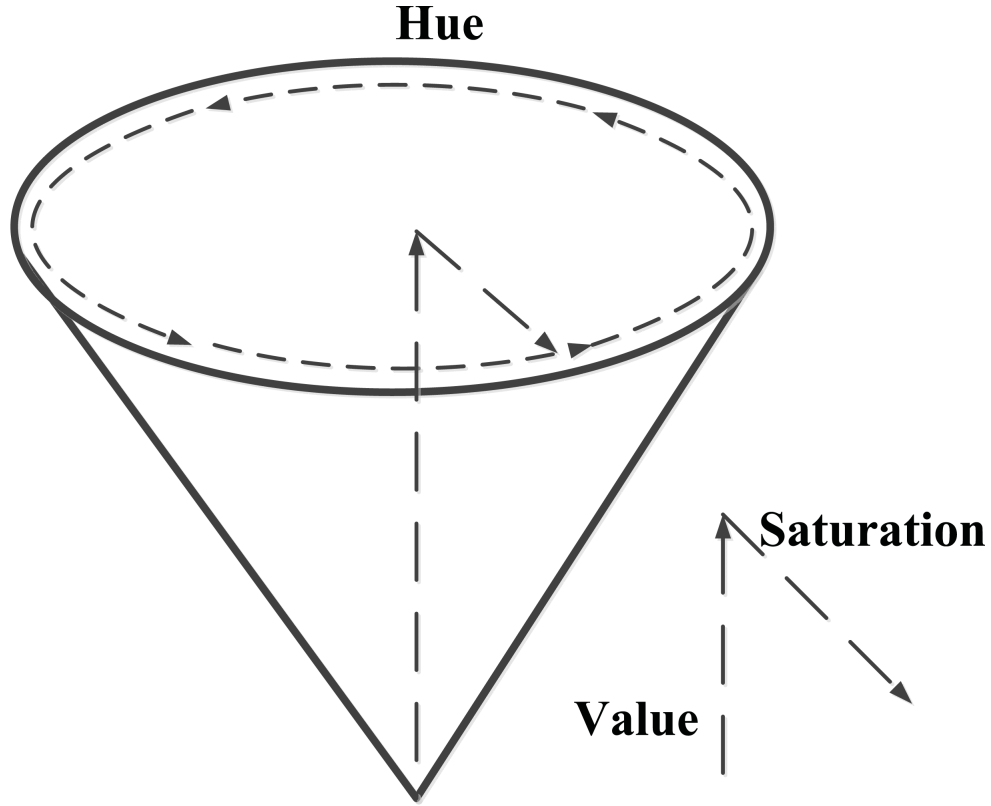
Figure 3.7: *HSV colour space cone.*

The conversion between RGB and HSV spaces is not straightforward but is well documented in [61]. Here the equations for conversion are given.

Assume r, g, b ∈ [0,1] be the coordinates of the red, green, and blue, respectively, of the primary RGB colour space. To find the angle of hue $h \in [0, 360]$ for HSV space, calculate:

$$h = \begin{cases} 0, if \max = \min \\ (60° \times \dfrac{g - b}{\max(r, g, b) - \min(r, g, b)} + 0°) \mod 360°, if \max = r \\ 60° \times \dfrac{b - r}{\max(r, g, b) - \min(r, g, b)} + 120°, if \max = g \\ 60° \times \dfrac{r - g}{\max(r, g, b) - \min(r, g, b)} + 240°, if \max = b \end{cases} \tag{3.7}$$

For *s* and *v* of HSV colour space are given as follows:

$$s = \begin{cases} 0, if \max = 0 \\ \dfrac{\max(r,g,b) - \min(r,g,b)}{\max(r,g,b)} = 1 - \dfrac{\min(r,g,b)}{\max(r,g,b)}, otherwise \end{cases} \qquad (3.8)$$

$$v = \max(r,g,b) \qquad (3.9)$$

for grays, as $\min = \max h = 0$ is used even if the hue has no geometric meaning there.

CIE L*a*b* is another most extensively used colour space. In this colour space, L* represents luminance, while a* and b* represent colour components, according to nonlinearly compressed CIE 1931 XYZ colour space coordinates. The RGB values must first be transformed to a specific colour space(e.g. sRGB) and then be converted to CIE L*a*b* because these two colour models are device dependent. The conversion between RGB and CIE L*a*b* colour spaces is well documented in [61, 62]. Here the equations for conversion from CIE 1931 XYZ colour space to L*a*b* space are given.

$$L^* = 116 \times [f(\frac{Y}{Y_n})] - 16 \qquad (3.10)$$

$$a^* = 500 \times [f(\frac{X}{X_n}) - f(\frac{Y}{Y_n})] \qquad (3.11)$$

$$b^* = 200 \times [f(\frac{Y}{Y_n}) - f(\frac{Z}{Z_n})] \qquad (3.12)$$

$$\begin{cases} f(\dfrac{Y}{Y_n}) = (\dfrac{Y}{Y_n})^{1/3}, for(\dfrac{Y}{Y_n}) > 0.008856 \\ f(\dfrac{Y}{Y_n}) = 7.787 \times (\dfrac{Y}{Y_n}) + \dfrac{16}{116}, for(\dfrac{Y}{Y_n}) \leq 0.008856 \end{cases} \qquad (3.13)$$

where X_n, Y_n and Z_n denote the tristimulus values of the reference white respectively. Details about the CIE L*a*b* space can be easily found in many image processing or colour related books (e.g. [62]).

3.2 Image Enhancement: Contrast enhancement and Histogram Modification

Due to the digital nature of a fundus camera or retinal camera, the output is in a digital format; in fact, they are raster images or bitmaps. In a fundus image, the intensity depends on the physical properties of the tissue. The intensities are usually described by eight bits per pixel, which allows the use of 256 gray scales. There are various different sources of interference in the production of images (e.g. the performance of the fundus camera). Moreover, some fundus cameras can not produce images without noise. The biggest problem is usually noise, which can be reduced by exploiting image enhancement approaches. These approaches could also be employed if the quality of an image is poor in its contrast. The most common used image enhancement approaches are stated in the following sub sections.

3.2.1 Contrast enhancement

A nonlinear and reduced image amplitude range probably results in poor contrast which is one of the most common imperfections of digital images. By rescaling the amplitude of individual pixels, the contrast of an image can usually be improved. The transfer function of the most continuous amplitude images can be realised by photographic techniques, but to implement an arbitrary transfer function accurately is very difficult. It is a trivial task to implement the transfer function for quantised amplitude images [2]. In terms of the implementation of the operator of the transfer function, the effects of amplitude quantisation have to be taken into consideration. It is usually able to reduce the gray scale contouring effect by achieving a linear placement of output levels if the output image is quantised to more levels than the input image [2].

Amplitude Scaling
The raw image probably takes up a range different from that of its raster image after digitalisation. Its numerical range probably covers pixels with negative values and can not be mapped straightforwardly into an intensity range [2].

Three different methods, which scale an output image back into the domain of values dominated by the raw image, are demonstrated in Figure 3.8.

For visualising an image with negatively valued pixels, the first technique of absolute amplitude value scaling, shown in Figure 3.8a, is used to exploit the transformation of absolute
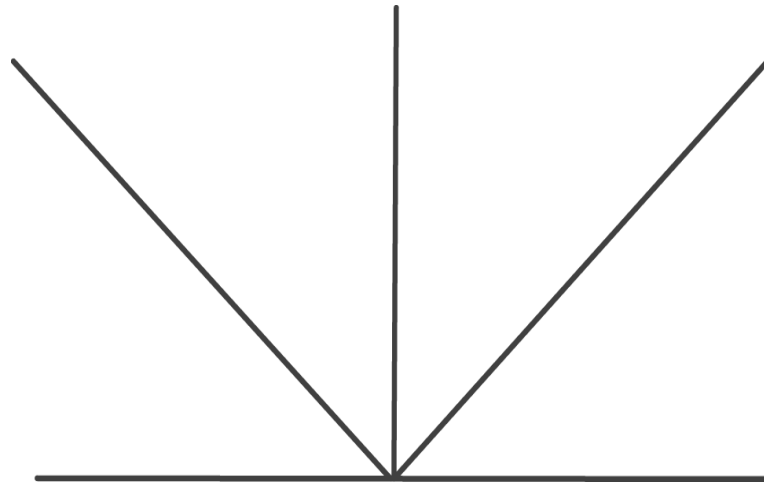
(a) Absolute value scaling. The amplitude value of the pixel overshoots +1.0 by a small amount, it wraps around by the same amount to -1.0.

OUTPUT

OUTPUT
RANGE

INPUT

INPUT RANGE
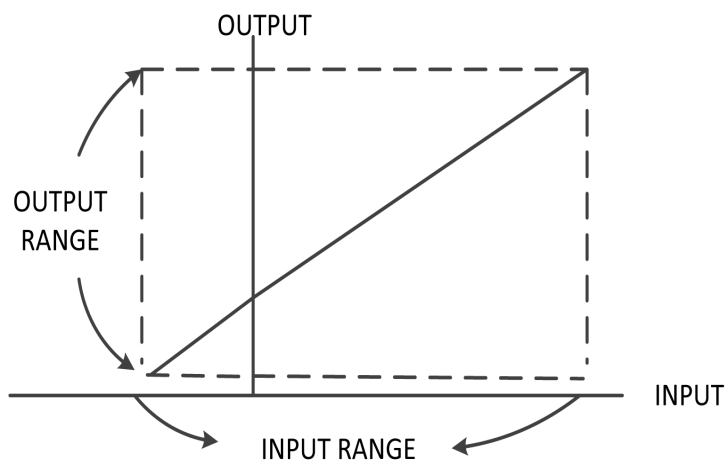
(b) Linear image scaling. The amplitude values of the processed image is linearly mapped over its entire range.

OUTPUT

OUTPUT
RANGE

S   M   T   INPUT

INPUT RANGE
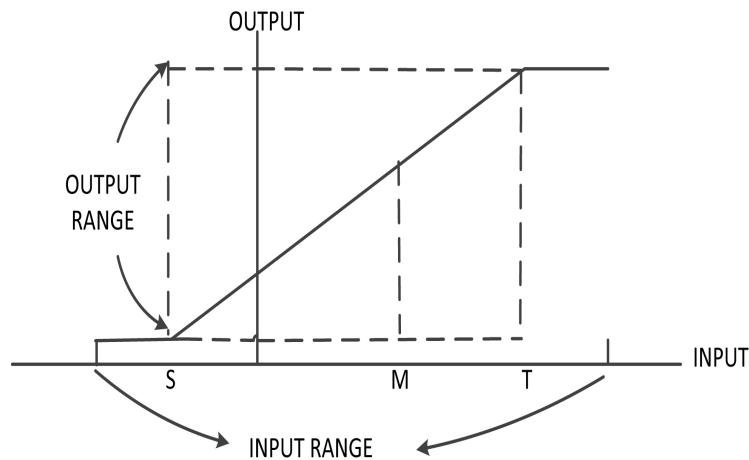
(c) Linear image scaling with trimming. The extreme amplitude values of the processed image are trimmed to maximum and minimum limits.

***Figure 3.8:** Three common image scaling methods [2].*

value [2].To represent amplitude by utilising the two's complement numbering convention is an essential transformation for system. In this kind of system, if the amplitude of the pixel exceeds +1.0 by a small amount, it wraps around by the same amount to -1.0 (here +1.0 and -1.0 both represent maximum of luminance white) [2]. Likewise, if the amplitude of the pixel undershoots stay almost black.

The processed image is linearly mapped over its whole range by the linear image scaling technique (See Figure 3.8b). The same mapping for the linear image scaling with trimming technique (See Figure 3.8c), but the extreme amplitude values (*S* and *T*) of the processed image are trimmed to minimum and maximum limits.

The last technique is particularly useful for images in which a small number of pixels exceed the limits. A certain proportion of the amplitude values on the end of the amplitude scale usually can be trimmed by contrast enhancement techniques [2]. For example, Figure 3.8c is a typical contrast modification operation applied to bio-medical image enhancement applications. A window-level transformation is shown in the Figure 3.8c. The width of the linear slope, *T-S*, is the value of this window. The level of the window is situated at the midpoint *M* of the slope line [2].

3.2.2 Histogram Modification

Images may have foregrounds and backgrounds that are both dark or both bright. In such images, segmentation tasks are not easy accomplished. Such types of images can be enhanced by the histogram equalisation technique, which is a means of contrast adjustment using the image's histogram. This method rescales the original image, and therefore the histogram of the enhanced image, to a certain desired form. For example, it can increase the global contrast of many images, particularly when the usable data of the image has close contrast values. The intensities can be better distributed on the histogram by this adjustment (e.g. local areas of lower contrast gain a higher contrast). In the literature, enhanced images have been produced by a histogram equalisation procedure for which the enhanced image's histogram must be uniform [63–65] and an adaptive histogram equalisation process has been used to improve the results [66, 67] have described improved results by using an adaptive histogram equalisation process. An example of histogram equalisation for a fundus image is given in Figure 3.9. The original fundus image in RGB space, in gray level and its histogram are shown in Figure 3.9a, Figure 3.9b and Figure 3.9c, respectively. In the histogram equalised result of Figure 3.9d, optic

nerve features from the fundus image, not seen in the original (See Figure 3.9b), are distinctly visible. In addition, the enhanced image's histogram (See Figure 3.9e) appears peaked, and many gray level output values are occupied. Obviously, histogram equalisation often performs better on images with detail concealed in dark regions. However, it usually degrades good quality originals [2].

Adaptive Histogram Equalisation

The mapping function of histogram equalisation is changed dependent on the histogram of the whole image. By employing histogram modification to every pixel according to the pixels' histogram within a moving window vicinity, histogram equalisation can be made spatially adaptive. The technique, which has to generate a histogram, compute the mapping function, and map the function at each individual pixel, is computationally intensive. An adaptive histogram equalisation technique has been proposed [68] in which a rectangular grid of points produces the histogram and interpolating mappings of the four neighbouring rectangular grid points yields the mappings for an individual pixel.

Figure 3.10 demonstrates the interpolative adaptive histogram equalisation enhancement array geometry. An individual grid point in a window about the grid point yields a histogram. In addition, the dimensions of the window can be larger or smaller than the grid spacing.

Assume H_{00}, H_{01}, H_{10}, H_{11} represent the mappings of the histogram equalisation produced at four nearest grid points. The pixel S(i, k) is determined by a bilinear interpolation of the mappings of the four neighbouring grid points defined by

$$H = a[bH_{00} + (1 - b)H_{10}] + (1 - a)[bH_{01} + (1 - b)H_{11}] \qquad (3.14)$$

where

$$\left\{ \begin{array}{l} a = \dfrac{k - k_0}{k_1 - k_0} \\ b = \dfrac{i - i_0}{i_1 - i_0} \end{array} \right\} \qquad (3.15)$$
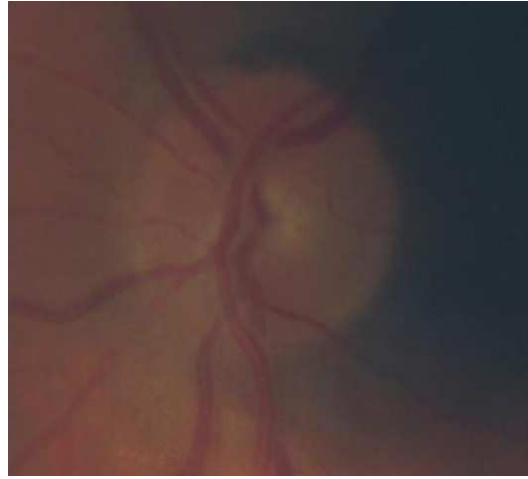
(a) Original fundus in RGB space.
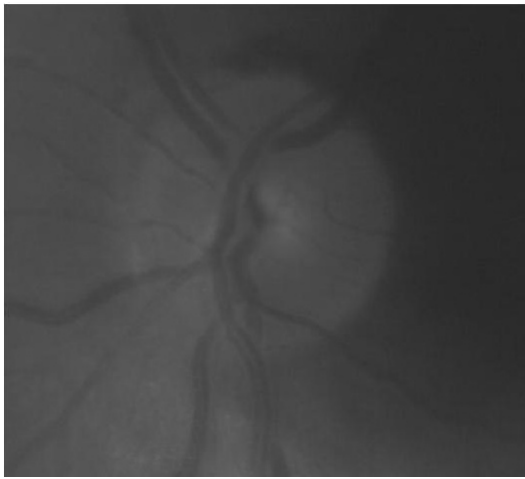
(b) Original fundus in grayscale.
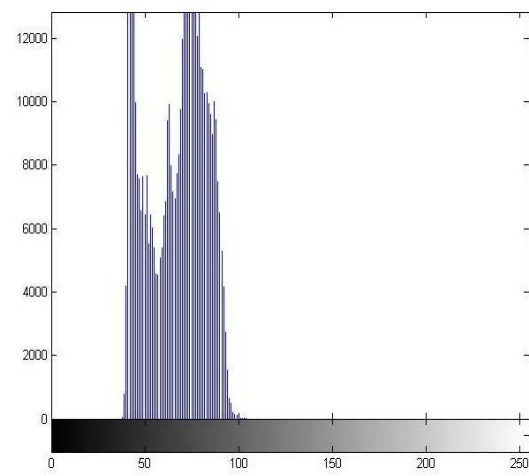
(c) Original grayscale image Histogram.
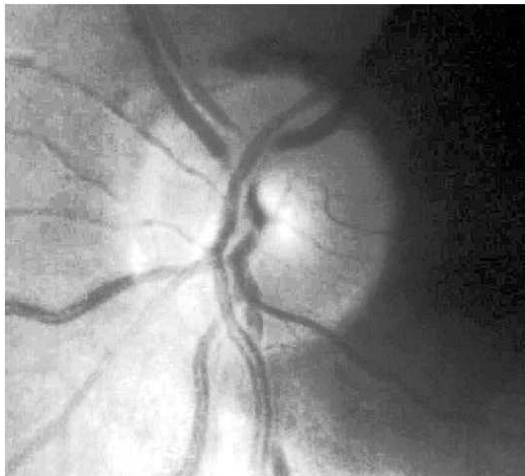
(d) Grayscale fundus image enhanced by non-adaptive histogram equalisation.
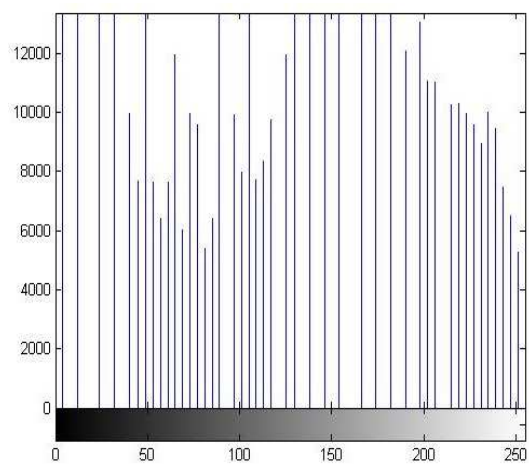
(e) Enhanced grayscale fundus image Histogram.

Figure 3.9: *Histogram equalisation.*
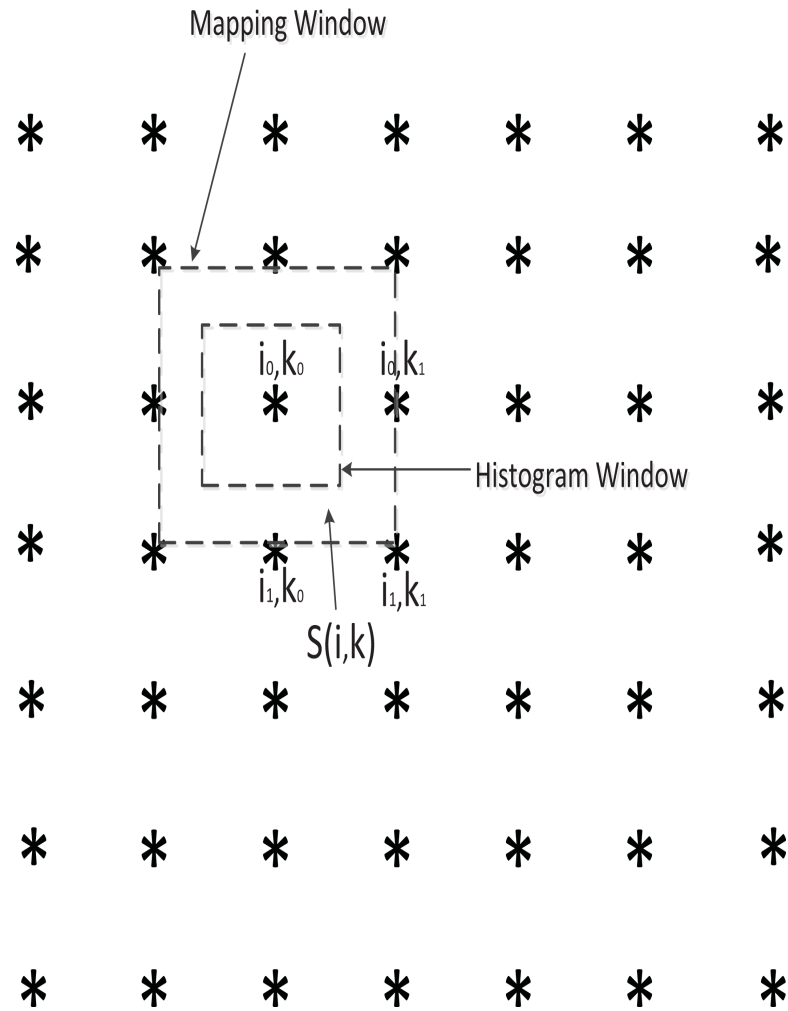
Figure 3.10: *Interpolative adaptive histogram equalisation enhancement array geometry [2].*

The special cases of equation(3.14), pixels in the margin region of the grid points, is tackled.

In practice, it is more efficient for parallel processes to exploit the histogram produced by histogram window and to employ the consequent mapping function in every pixel in the mapping window of the Figure 3.10. The procedure is then repeatly executed at every grid point. Bilinear interpolation is used to integrate the four modified pixels of histogram acquired from the four overlap mappings at each individual pixel coordinate (i, k). Figure 3.11 illustrates a comparison between adaptive and non-adaptive histogram equalisation of a gray-level fundus image.

3.3 Edge Detection: First-Order Derivative Edge Detection and Second-Order Derivative Edge Detection

The object edge is marked by its angle of slope, height and its slope midpoint's horizontal coordinate. When the height of the edge is much higher than a specific value, an edge occurs. An edge detector ideally yields an edge mark localised to a single pixel situated at the slope centre. In the continuous-domain, lines and edges in a 2D image assume that the discontinuity of the amplitude stays constant in a tiny vicinity which is normal to the line profile or edge. The transition model of a single pixel has a mid-value transition pixel interpolated between the low-value of the background and the high value of the line plateau. Two main types of differential edge detection are briefly introduced in this section [2]: 1st- order and 2nd-order derivatives. For the former type, certain forms of spatial 1st-order differentiation are computed, and the consequent edge gradient is compared to a specified threshold value. If the gradient value exceeds the given threshold, an edge is determined to exist. For the latter type, if the greatest spatial change occurs in the polarity of the 2nd derivative, an edge is determined to exist.

3.3.1 First-Order Derivative Edge Detection

In the continuous domain, an edge segment *S(x,y)* can be captured by producing the continuous 1D gradient *G(x,y)* along a line perpendicular to the slope of an edge, which is at an angle with regard to the horizontal axis. An edge is regarded to exist if the gradient is adequately large. The gradient along the line perpendicular to the slope of the edge can be calculated as follows [2]:
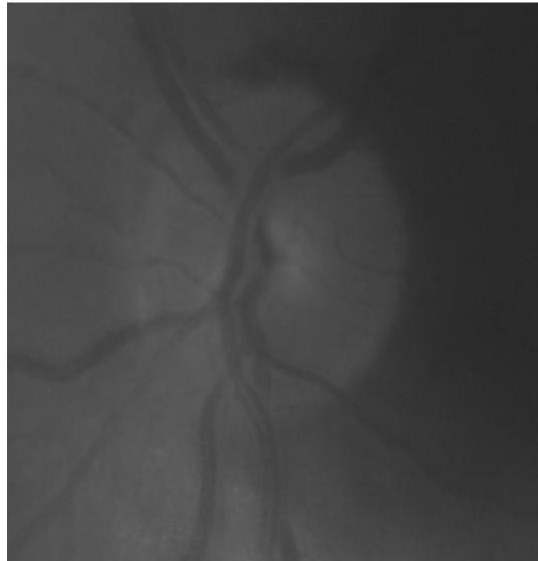
(a) Original
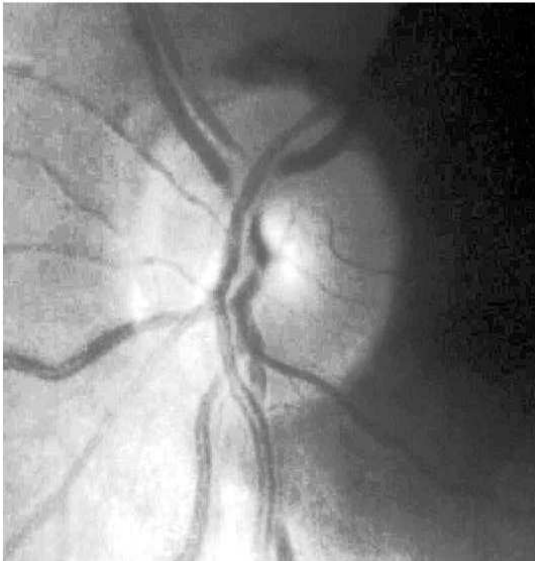
(b) Non-adaptive histogram equalisation
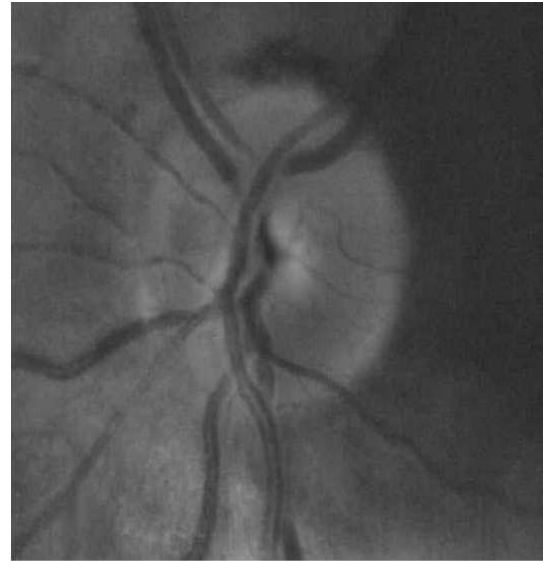
(c) Adaptive histogram equalisation. Provides better Optic Nerve features compared with Non-adaptive histogram equalisation method.

Figure 3.11: *Non-adaptive and adaptive histogram equalisation.*

$$G(x, y) = \frac{\partial S(x, y)}{\partial y} \cos \theta + \frac{\partial S(x, y)}{\partial x} \sin \theta \qquad (3.16)$$

In the discrete domain, an edge gradient $G(x,y)$ is generated by a column gradient $G_C(j, k)$ and a row gradient $G_R(j, k)$ in the discrete domain (shown in Figure 3.12). The amplitude of spatial gradient is defined as

$$G(j, k) = [[G_C(j, k)]^2 + [G_R(j, k)]^2]^{1/2} \qquad (3.17)$$

The amplitude of gradient can be estimated by Equation (3.18) for computational efficiency.

$$G(j, k) = \mid G_C(j, k) \mid + \mid G_R(j, k) \mid \qquad (3.18)$$
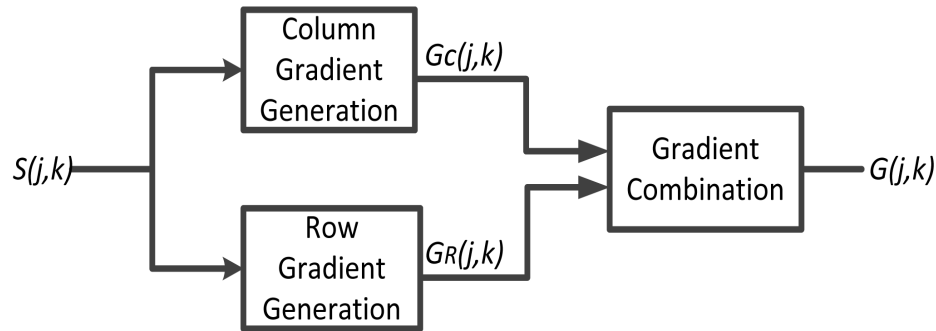
***Figure 3.12:** Orthogonal gradient generation [2].*

Equation (3.19) describes the orientation of the spatial gradient with respect to the horizontal axis.

$$\theta(j, k) = \arctan(\frac{G_C(j, k)}{G_R(j, k)}) \qquad (3.19)$$

The following issue for orthogonal gradient generation in discrete domain is to select a good discrete estimation to the continuous differentials of equation (3.16). In this subsection, the column and row gradients for all aforementioned edge detectors contain a linear combination of pixels within a tiny vicinity. The column and row gradients can therefore be calculated by

the convolution operation:

$$\begin{cases} G_C(j,k) = S(j,k) \oplus H_C(j,k) \\ G_R(j,k) = S(j,k) \oplus H_R(j,k) \end{cases} \tag{3.20}$$

where $H_C(j,k)$ and $H_R(j,k)$ are a 3x3 impulse response arrays, respectively. Some examples are shown in Figure 3.13 [2].

Two common operators, **Prewitt** and **Sobel**, are here briefly illustrated in Figure 3.13.

The **Prewitt** is technically a discrete differentiation edge operator, calculating an estimation of the gradient of the image intensity [2]. It offers the rate of change in the direction of the largest possible rising from light to dark. The result of this discrete differentiation edge operator is either the norm of the gradient vector or the corresponding vector point in an input grayscale image. It therefore demonstrates how smooth or abrupt the image edges are and how an edge is likely to be oriented. The result of the **Prewitt** operator is a zero vector when applying it to a point which is at a small region of constant intensity.

Overall, in terms of computations, the **Prewitt** operator is comparatively inexpensive because it is mathematically according to convolving the image with a separable and integer valued filter in both the vertical and horizontal direction. In addition, it is relatively crude to estimate the gradient, emphasizing regions of high spatial frequency variations that correspond to the edge.

The **Prewitt** operator can be illustrated by the numbering convention of the pixels of Figure 3.14. Its operator edge gradient is defined by equation (3.17) with equation (3.21 and 3.22) [2].

$$G_C(j,k) = \frac{1}{K+2}[(P_0 + KP_1 + P_2) - (P_6 + KP_5 + P_4)] \tag{3.21}$$

$$G_R(j,k) = \frac{1}{K+2}[(P_2 + KP_3 + P_4) - (P_0 + KP_7 + P_6)] \tag{3.22}$$

where K = 1. The unit-gain negative and positive weighted averages about a separated edge position are offered by normalising the column and row gradients in these formule. Each individual pixel contributes to the gradient equally by introducing the **Sobel** edge operator. The

Operator	Column gradient	Row gradient
Prewitt	$\dfrac{1}{3}\begin{bmatrix} -1\,-1\,-1 \\ 0\ \ 0\ \ 0 \\ 1\ \ 1\ \ 1 \end{bmatrix}$	$\dfrac{1}{3}\begin{bmatrix} 1\ \ 0\,-1 \\ 1\ \ 0\,-1 \\ 1\ \ 0\,-1 \end{bmatrix}$
Sobel	$\dfrac{1}{4}\begin{bmatrix} -1\,-2\,-1 \\ 0\ \ 0\ \ 0 \\ 1\ \ 2\ \ 1 \end{bmatrix}$	$\dfrac{1}{4}\begin{bmatrix} 1\ \ 0\,-1 \\ 2\ \ 0\,-2 \\ 1\ \ 0\,-1 \end{bmatrix}$
Seperated Pixel difference	$\begin{bmatrix} 0\,-1\ 0 \\ 0\ \ 0\ \ 0 \\ 0\ \ 1\ \ 0 \end{bmatrix}$	$\begin{bmatrix} 0\ \ 0\ \ 0 \\ 1\ \ 0\,-1 \\ 0\ \ 0\ \ 0 \end{bmatrix}$
Pixel difference	$\begin{bmatrix} 0\,-1\ 0 \\ 0\ \ 1\ \ 0 \\ 0\ \ 0\ \ 0 \end{bmatrix}$	$\begin{bmatrix} 0\ \ 0\ \ 0 \\ 0\ \ 1\,-1 \\ 0\ \ 0\ \ 0 \end{bmatrix}$
Roberts	$\begin{bmatrix} -1\ 0\ 0 \\ 0\ \ 1\ \ 0 \\ 0\ \ 0\ \ 0 \end{bmatrix}$	$\begin{bmatrix} 0\ \ 0\,-1 \\ 0\ \ 1\ \ 0 \\ 0\ \ 0\ \ 0 \end{bmatrix}$

Figure 3.13: *Some examples of impulse response arrays for 3 x 3 orthogonal differential gradient edge operators [2].*

P$_0$	P$_1$	P$_2$
P$_7$	s(j,k)	P$_3$
P$_6$	P$_5$	P$_4$

Figure 3.14: *Pixel numbering convention for 3×3 pixel edge gradient operator [2].*

Sobel edge operator is implemented with K $= 2$, which differs from the **Prewitt** edge operator in doubling the values of the east, west, south and north pixels [2]. Figure 3.15 gives some examples of the Prewitt and Sobel of the the 2D fundus image.

3.3.2 Second-Order Derivative Edge Detection

The 2nd-order derivative edge detection applies a certain form of spatial 2nd-order differentiation to significant edges. If a dramatic change in the intensity gradient takes place in the 2nd derivative, an edge is captured. Two kinds of 2nd-order derivative approaches are taken into consideration: directed 2nd derivative and Laplacian operator [2].

Laplacian

In the continuous domain, the Laplacian function *L(x,y)* of an image *F(x,y)* can be defined as:

$$L(x, y) = - \bigtriangledown^2 F(x, y) \tag{3.23}$$

here

$$\bigtriangledown^2 f = \frac{\partial^2 f}{\partial x^2} + \frac{\partial^2 f}{\partial y^2} \tag{3.24}$$

If *F(x,y)* is changing linearly or is constant in amplitude, the Laplacian *L(x,y)* is zero. In addition, if the rate of change of *F(x,y)* is greater than linear, *L(x,y)* shows a sign change at the point of inflection of *F(x,y)*.
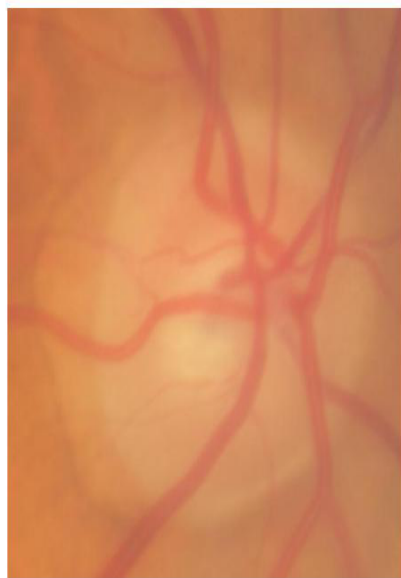
(a) Original 2D fundus image in RGB space
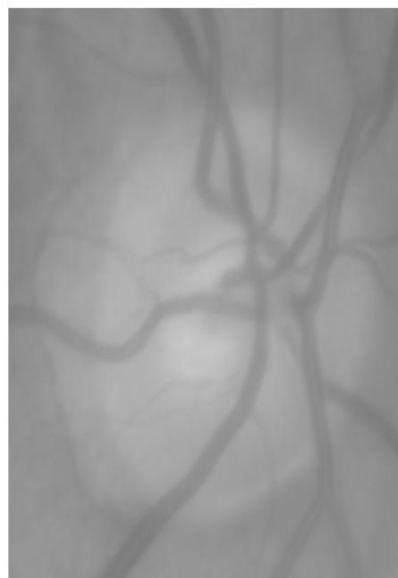
(b) The grayscale of original 2D fundus image
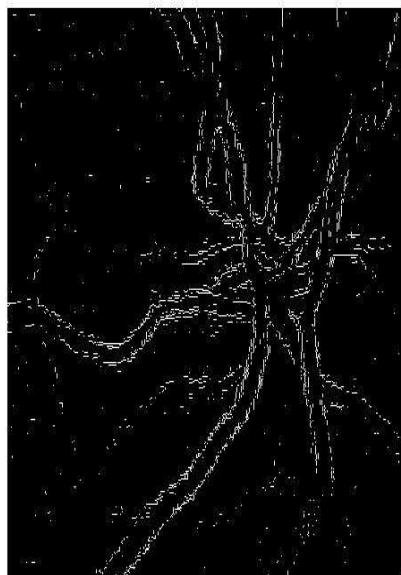
(c) Prewitt
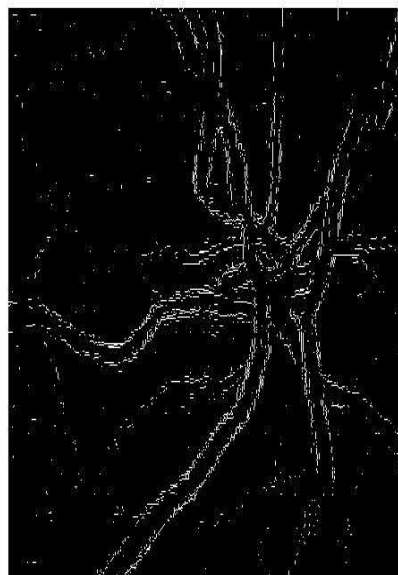
(d) Sobel

Figure 3.15: *Prewitt and Sobel gradients of the 2D fundus image.*

A zero crossing in *L(x,y)* implies the occurrence of an edge. The negative sign in the definition of equation (3.23) means that for the edge with an amplitude increasing from bottom to top or left to right in an image, the zero crossing of *L(x,y)* has a positive slope [2].

Laplacian zero-crossing Detection

The Laplacian zero crossings do not lie at pixel sample points in the discrete domain. As a matter of fact, it is unlikely for real images subject to fluctuations of luminance including zero-valued Laplacian response pixels and ramp edges of varying slope.

In discrete domain images, a simple method for Laplacian zero-crossing detection is to produce the minimum of all negative-value responses and the maximum of all positive Laplacian responses in a 3×3 window, respectively. An edge is determined present if the magnitude of the difference between the minima and the maxima is bigger than a threshold.

3.4 Chapter Summary

In the first part of this chapter, the basic theory of image pre-processing techniques was briefly introduced. The definition of digital image, the working principles of binary morphological operations (including erosion, dilation, opening, closing) and image filters (e.g. average filter, median filter and linear filter with convolution kernel) and the conversion between RGB space and HSV space or Lab colour space were explained. Two common image enhancement techniques, contrast enhancement and histogram modification, were described followed by an introduction to edge detection techniques. In this part, first-order (e.g. Prewitt and Sobel operators) and second-order derivative detection were described in detail. Overall, binary morphological operations, image filters and image enhancement techniques are most widely applied to the digital images in order to reduce the noise. The representation of HSV and Lab space is more consistent with human perception compared with that of RGB space. Edge detection is a primary tool in image processing in image processing, particularly in the area of feature extraction, which aims at detecting points in a digital image at which the intensity of an image changes sharply.

Chapter 4
Review of Major Image Segmentation Techniques

In this chapter, three different types of image segmentation techniques: thresholding techniques, region growing techniques and active contour (snakes), are introduced. The main focus is on providing the necessary background of image segmentation techniques that are relevant to this work.

4.1 Introduction

Many investigations into segmenting objects in an image automatically have been conducted for decades. Existing techniques for image segmentation theoretically can be categorised as three main types: feature space-based approaches, image domain-based approaches and physics-based approaches [69–71]. For the first approach, clustering techniques are frequently employed in the data distribution to classify image data into different groups. For the second approach [71–74], neighbouring pixels with small colour or intensity variations are integrated together based on the discontinuity of local information or the similarity of adjacent pixels. For the last approach, the mathematical models are fundamentally the same as the prior two types of approaches, while the last approach is utilised to specify the reflection features of coloured matter [69, 71]. In terms of implementation, the existing segmentation techniques, in practice, can be roughly classified as the following approaches:

a) Boundary-based techniques [70, 71, 75–77]: These techniques generally extract contours of the targeted region, namely edges. However, further processing is necessary because there are major limitations, over-/under- segmentation, to these methods.

b) Histogram-based techniques [70, 71, 78, 79]: These methods usually apply to gray-level images, normally with a 1D histogram. Regrettably, the techniques do not work effectively in

colour images, because it is a challenging problem to choose an appropriate global threshold in 3D space as the colour images are normally illustrated by 3D histogram.

c) Region-based techniques [70, 71, 80–83]: Merge-and-split and region growing are two common approaches of these techniques which group pixels with similar features according to the predefined criteria. However, these are two main shortcomings which limit the performance of segmentation. First, they both highly rely on manually adjusted thresholds. Second, for the latter approach, it also relies on setting initial seeds properly.

d) Hybrid-based techniques [70, 71, 84–90]: These techniques improve the performance of segmentation by combining the edge and region information. However, it is a non-trivial task to properly integrate these two features.

e) Graph-based techniques [70, 71, 91, 92]: These techniques traditionally utilise graphs in which the nodes denote the pixels and arcs connect the adjacent pixels. By minimising the weight that divides a graph into sub-graphs, the segmentation is implemented. It in general has a problem of high computational complexity.

Using mean shift algorithms to estimate the feature space was introduced for image segmentation [93]. Analysing the feature space is done by investigating the centres of the high density regions. According to the mean shift algorithm, it is an easy non-parametric procedure for computing density gradients to represent the important features of the image. This approach can achieve under-or over-segmentation by setting different parameters. However, undesired results occur frequently and this method is very complex. A non-parametric clustering algorithm maps an image from its primordial feature space (e.g. texture, intensity and colour) to the space of non-parametric density [94]. Connectivity and Isolation are then used for the sake of determining how to integrate regions. The segmentation performance is good according to their results. However, this method is computationally expensive. The JSEG method is proposed for colour image segmentation [95]. Figure 4.1 shows a flow chart of JSEG method. It consists of two stages: colour quantisation and spatial segmentation. In the first phase, colours in the image are categorised into several representative classifications. A class-map of the image is then produced by replacing the image pixel values with their corresponding colour class labels. In the second phase, spatial segmentation is achieved by yielding a *J*-image, region growing

Colour Image

Colour quantisation

Class-map

Spatial segmentation

J-image generated

Region growing

Regions United
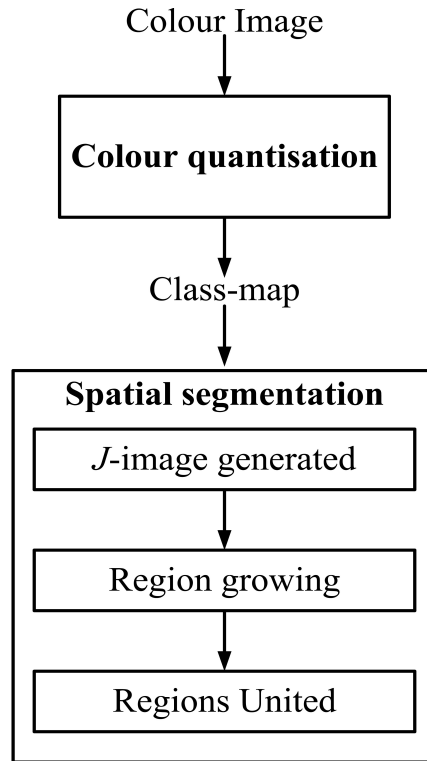
Figure 4.1: *A flow chart of JSEG method.*

and uniting regions. The *J*-image is generated by applying the segmentation criteria to local windows in the class-map. The initial regions/clusters are then acquired by using region growing approach and is followed by an agglomerative approach, a hierarchic procedure, to unite the initial regions/clusters step by step. According to the report, their proposed method also gets good results on segmentation. But, it is also computationally expensive compared to the "nonparametric clustering."

Many researchers analyse different properties of images by using complicated formulas for the sake of improving the segmentation results. This makes them more difficult to implement and sacrifices the operation time. The time-consumption therefore would be a bottleneck to those complicated algorithms, which limits the applications of those algorithms. Some inherent problems exist because the segmentation is not well defined. We briefly summarise as follows.

a) The segmentation results will be changed dramatically by different settings, so that many manually adjusted thresholds or parameters have to be carefully predetermined.
b) It is difficult to choose a representative feature for the evaluation of image similarity because a general similarity suitable for all types of images does not exist.

c) An exact number of sub-regions in the image is difficult to decide by giving proper criteria for unsupervised segmentation.

In next following sections, we will introduce three common image processing techniques: Region growing techniques (Region-based techniques), thresholding techniques and active contour techniques.

4.2 Thresholding Techniques

Many images can be depicted as comprising regions of interest (ROI) of moderately unvaried intensity value against a background of different intensity value. Typewritten text, aeroplanes on runways and microscope biomedical samples are three classical examples. When segmenting the targeted region from its background, luminance is a significant feature that can be used for these kind of images. If a ROI is black against a white background, or vice versa, giving a threshold (the mean of the minimum and maximum gray values in the local window) to extract the targeted region from the background is a simple work. Practical difficulties take place, however, as the processed image encounters noise and as both the targeted region and background region assume a wide range of gray scales. The background region is probably non-uniform which is another general problem. Thresholding techniques are briefly introduced in this subsection.

Let *A* represents a given input image, as a binary image *B*, where the b_n pixel gray-levels in *B* are restricted to 0,1. Assume a_n is the gray level of the *nth* pixel in *A*, then the corresponding value in *B* is:

$$b_n = \left\{ \begin{array}{lll} 1, & if & a_n \geq t_n \\ 0, & otherwise \end{array} \right\} \tag{4.1}$$

where t_n is the threshold value for the *nth* pixel. The thresholds $t_n, n \in 1, 2, ..., M$, may all be equal to a global threshold t_G or they may vary locally (e.g. from pixel to pixel). Here, we only use information contained in the current input image to calculate t_m and t_G.

The pixels in the image are therefore split into two groups: high intensity or high luminance pixels whose gray-levels are greater than, or equal to, a threshold *t* and low intensity or low

luminance pixels whose gray-levels are less than t. The existing thresholding techniques, in practice, could be roughly classified into the following five approaches [96] described in Table 4.1.

Five existing thresholding techniques	Descriptions
a) Object Attribute-based techniques	The methods use a measure of similarity between the binarised images and gray-level images.
b) Histogram-based techniques	Both shape and features of the image histogram are analysed by the techniques.
c) Cluster-based techniques	The pixel gray-levels are clustered into two groups, background and foreground pixels, by these methods.
d) Spatial-based techniques	The higher-order probability distribution is utilised in these methods to model the correlation between pixels.
e) Entropy-based techniques	An optimal threshold is found by using the entropy of the histogram or cross-entropy between the thresholded image and input image.

Table 4.1: *A summary of existing thresholding techniques*

4.3 Region Growing Technique

The primary concept of region growing approach is that it merges adjacent pixels of similar amplitude together to produce a detected area. However, for obtaining acceptable results, some complex constraints have to be imposed on the growth pattern results. A region-growing approach with a combination of uncomplicated growth rules has been proposed [97, 98]. Figure 4.2 shows two neighbouring regions, R_a and R_b, with different perimeters P_a and P_b, respectively, which will be considered for grouping together. Likewise, assume J represents the length of the joint border and assume B denotes the length of that part of J for which the value of the difference of amplitude D across the border is smaller than a setting parameter ε_1 [2]. The process of this technique is: Pairs of quantised pixels of the same amplitude are first merged together in *atomic regions* if they are non-orthogonal neighbouring pixels in the image. Weak boundaries between atomic boundaries are then dissolved by two heuristic rules. A processed region then probably includes preceding integrated sub-regions of diverse amplitude values. The regions R_a and R_b are then integrated according to following a condition
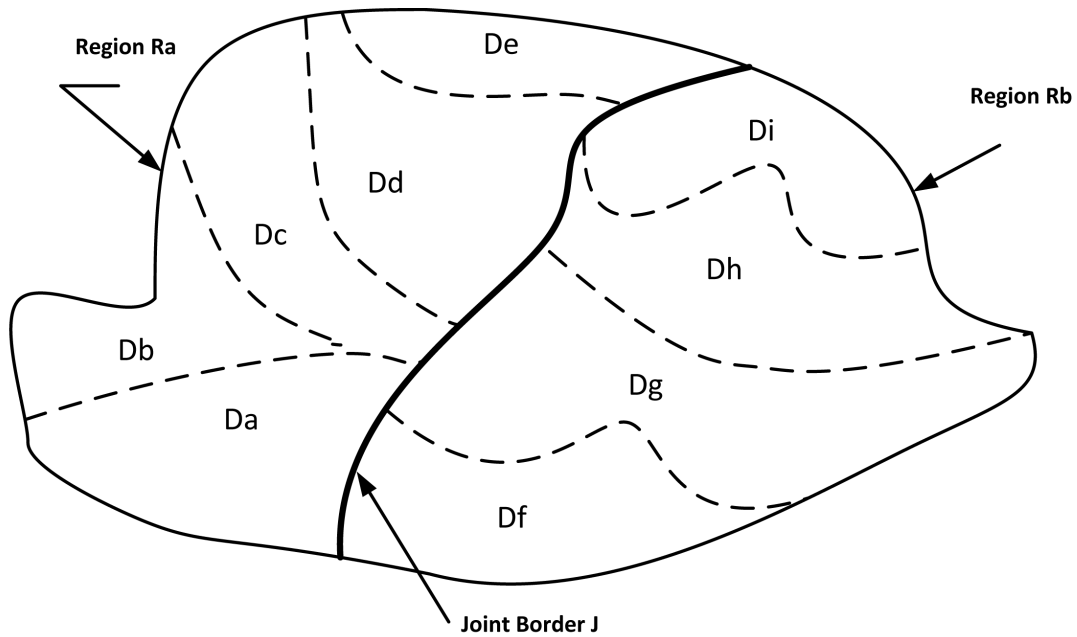
Figure 4.2: *A geometry for region growing [2].*

$$\frac{B}{MIN(P_a, P_b)} > \varepsilon_2 \qquad (4.2)$$

where a constant, ε_2, is usually given as $\varepsilon_2 = \frac{1}{2}$. The setting allows several tiny sub-regions to be merged into bigger sub-regions, which only absorbs the regions with strong joint borders by using equation (4.2). Another criterion is used to the result of equation (4.2) for the sake of merging the regions with weak joint boundaries. The neighbouring regions with weak common boundaries are then integrated if

$$\frac{B}{J} > \varepsilon_3 \qquad (4.3)$$

where a constant, ε_3, is typically set at $\varepsilon_3 = \frac{3}{4}$. The region growing method proposed by Brice and Fenema [97] gives reasonable results on segmentation of few objects with simple scenes and little texture, but the method does not perform well on more complicated scenes [2].

Seeded region growing technique [99] involves the selection of initial seed points, which are not limited to pixel-based but also permits pure and simple region-based selection. This method of image segmentation inspects adjacent pixels of "seed points" and then decides whether the neighbouring pixels should be merged to the region, beginning with the points of lowest prior-

ity. The process is iterated on using an approach similar to those used in generic data clustering algorithms. The seeded region growing algorithm is described briefly.

Primary concept of seeded region growing

The foremost phase in seeded region growing technique is to determine initial seed points. The selection criteria are defined by attributes of the target regions in the image such as the brightest pixel or pixels in a certain range of gray levels. The process starts with these initial seeds' position then adds adjacent points as new seeds, beginning with the points of lowest priority of region membership criterion. The priority is defined by a distance function; it could be, for instance, variance, colour, gray level texture, motion, geometric properties and pixel average intensity. The distance of each pixel to a contiguous region is defined by:

$$R(x, \delta_i) = [I(x) - mean_j \in \delta_i(I(j))] \tag{4.4}$$

here *I(x)* denotes the gray image value of the point $x \in \delta$ and δ_i is the region labelled *i*.

All the information embedded within the image should be exploited to achieve the optimal result. For instance, one could study the histogram of the image and hence might identify a suitable threshold value of intensity. This threshold value could be then used to restrain the inclusion of undesired pixels into the region of membership. The pros and cons of seeded region growing are summarised in Table 4.2.

Pros	Cons
• Simple approach and easy to implement	• Time consuming
• Multiple criteria are allowed	• Probably not able to discriminate
• Correctly discriminates the regions that have	shadings in the image
similar features	• Variation of intensity may cause
• Performs well in certain types of noise	over-sized segmentation
• Produces good segmentation results when edges	
on original images are visibly clear	

Table 4.2: *The pros and cons of seeded region growing method*

Essential issues about seeded region growing:

There are two main concepts about seeded region growing:

a) Selecting the correct initial seed points is extremely important; however the selection is bound to vary from person to person or be diverse for different applications.

b) The more information (e.g. average intensity or variance of gray level image, colour and texture) about the image there is, the better the results that can be achieved.

4.4 Active Contour Models(Snakes) for Contour Detection

4.4.1 Overview of Active Contour Models

Explicit or implicit object features should be detected and computed at every possible image position for detecting objects. Up to now, diverse object features have been investigated (e.g., intensity, texture, shape, colour and motion). Shape plays a key role both in 2D space object contour pattern recognition and 3D object surface recognition. For example, contour information of the human body and organs is an essential measurement for biometrics, medical diagnosis and clinical analysis. For example, the ventricle of a beating heart is tracked for cardiac action analysis. Naturally, colour and size cooperating with shape could offer a powerful realisation for object search. Based on this concept, the 2D shape (e.g. object contour) was selected as the main feature used in the object segmentation algorithms using this work. When using the object feature of shape, a primary trend to tackle the computational problems is the model-based vision. To formulate visual models that unite the representation of shape by combining physics and geometry, a family of deformable models was proposed in the 1980s. The deformable models that depict object shapes (namely active shape models) include diverse forms (e.g., deformable contours, deformable surfaces and deformable templates). They are a free-form geometry that has the dynamics of elastic contours, surfaces and templates. In this section, we focus on deformable contours that are known as active contours (snakes) restricted to the plane. Snakes are now extensively applied in various computer vision and image processing applications comprising segmentation, edge detection, motion tracking and shape modelling.

The snake for the estimation of object contour was first introduced by Kass *et al*. [100]. An energy minimising function, a weighted combination of external and internal energy, are used to a deformable contour in order to estimate the real object border. Each individual contour point of the snake seeks its new position iteratively to move towards targeted region boundaries via the energy function minimisation. The external energy governs the attraction force (e.g. image

gradients that govern the contour deformation), while the internal energy directs the intrinsic continuity force of the contour itself. As a snake evolves by minimising energy, often the terms such as "wriggle" and "slither" are used to describe the process. The model proposed in [100] executes a global investigation to optimise the energy function. In addition, the snake is an "active" model and is most ideally initialised near the object boundary.

A lot of greedy strategies have been proposed to decrease snakes' computational complexity [101–103]. These greedy approaches seek local 4- or 8- neighbours, instead of seeking the optimisation of the global information, to accelerate the convergence of the snakes. Moreover, a gradient vector flow (GVF) field is proposed to be the term of the external force in the snake model, widely known as GVF snake, it is relatively robust for object contour detection [104].

4.4.2   Original snake models

The original snake model [100] in the image is thus defined by a set of n points

$$V_j = (x_j, y_j) \tag{4.5}$$

where j=0,1,2,....,(n-1). Its energy-minimising function in general is defined as

$$E_{snake} = \int_0^1 E_{snake}(v(s))ds = \int_0^1 E_{internal}(v(s)) + E_{external}(v(s))ds \tag{4.6}$$

here $v(s)$ represents the snake deformable contour and arc length denotes $s \in [0.0, 1.0]$. In addition, $E_{internal}$ and $E_{external}$ denotes the internal energy of the snake because of the curvature and external energy deforming on the snake, respectively.

(a) An internal energy term ($E_{internal}$)

$$E_{internal} = E_{cont} + E_{curv} = \frac{1}{2}(\alpha(s) \mid v_s(s) \mid^2 + \beta(s) \mid v_{ss}(s) \mid^2) \tag{4.7}$$

where E_{cont} is the energy of the snake contour and E_{curv} denotes the energy of the snake curvature. In addition, $\alpha(s)$ and $\beta(s)$ are two weighting parameters. The 1st-order derivatives $v_s(s)$ and 2nd-order derivatives $v_{ss}(s)$ of $v(s)$ denote the continuity and stretch contour forces,

(a) The sketch map of the motion of segmenting anchor by snakes

(b) The lips segmentation by the snake
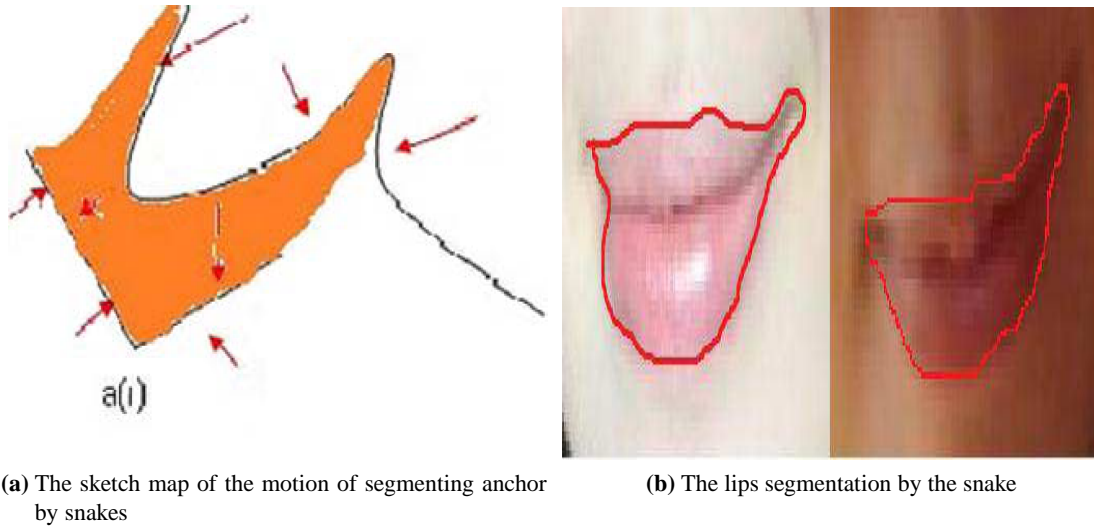
Figure 4.3: Samples of the original snake segmentation.

respectively. They make the snake deform like a membrane and like a thin plate, respectively. The bigger the value of $\alpha(s)$, the more sensitive the energy function is to the amount of stretch. Likewise, a bigger value of $\beta(s)$ will raise the internal energy of the snake as it evolves more rapidly into curvature, whereas small values of $\beta(s)$ will make the energy function less responsive in forming a curvature in the snake. The combination of smaller $\alpha(s)$ and $\beta(s)$ allows a more detailed modelling of the snake shape, at the cost of a longer computation time.

(b) An external edge based energy term ($E_{external}$)

$$E_{external} = E_{image} + E_{con} = W_{line}E_{line} + W_{edge}E_{edge} + W_{term}E_{term} \qquad (4.8)$$

where E_{image} denotes the image acting on snakes and E_{con} serves as an external constraint force introduced by programmer. In addition, E_{line}, E_{edge} and E_{term} represent line functional, edge functional and terminations, respectively. By adjusting the weights, W_{line}, W_{edge} and W_{term} to suitable values, the main features in the image may be extracted.

Two samples of the original snake segmentation are given in Figure 4.3. Figure 4.3a depicts an example application segmenting an orange colour anchor. The red arrows represent the attractive forces towards anchor points, *a(i)*, as well as the repulsive forces. Figure 4.3b shows another example where the snake is employed to track a person's lip.

Alternatively, $E_{external}$ could be defined as negative magnitudes of image gradient:

$$E_{external} = - \mid \nabla(G_\sigma * I(x, y)) \mid^2 \tag{4.9}$$

here $I(x, y)$ denotes the processed image, ∇ represents the gradient operator, and G_σ denotes the Gaussian filter with standard deviation σ. From the calculus of variations, the minimisation of the function of the snake E_{snake} can be obtained by solving the following equations:

$$\alpha v_{ss} - \beta v_{ssss} - \nabla E_{external} = 0 \tag{4.10}$$

where v_{ssss} is the 4th derivatives of $v(s)$. $v(s)$ can be regarded as a function of time t and an iterative optimisation procedure can be employed in order to solve equation (4.10). An initial estimate of the solution can be obtained as follows [100, 104],

$$v_t(s, t) - \alpha v_{ss}(s, t) - \beta v_{sss}(s, t) - \nabla E_{external} = 0 \tag{4.11}$$

here $v_t(s, t)$ denotes the 1st partial derivative of $v(s, t)$ in regard to t. The original snake model combines external and internal energy together, by which a snake is deformed towards targeted region contours.

On one hand, a smaller external energy is resulting from the object contours that usually have bigger gradient magnitudes. Therefore, the minimised external energy modifies the contour according to the status of the image gradient where it is processed. On the other hand, the minimised internal energy retains compactness and smoothness of the shape of the contour, but it probably degenerates to a single point in the difficult case. In conclusion, the deformation of the snake is governed by two different forces, the external and internal energy items, and the equation (4.6) demonstrates a compromise between the external and internal energy by the weighting parameters $\beta(s)$ and $\alpha(s)$. Regrettably, for original snake models, the external force is limited to regions adjacent to the object contours. The snakes perform badly and are most likely fail to estimate them as the contours of the snake are initialised far from object contours. The snakes implemented by original image gradient fields also failed in converging to the concave parts of the targeted boundary for the same reason. It is therefore widely known that the snake models are a good approach to estimate object borders based on edge-based

segmentation techniques by giving an accurate initial mask of the contour. In addition to this, global energy minimisation takes a quite high computational cost. Aforementioned problems are three main drawbacks of the original snake segmentation.

4.4.3 Greedy snake models

The greedy snake models [101–103, 105] adopt a local seeking scheme instead of global optimisation during the energy-minimising process. Each individual snake point i moves toward its next location within m-neighbours (normally, 4- or 8-neighbors) with lowest Energy Function energy by comparing the snake energy $E^i_{snake,j}$:

$$E^i_{snake,j} = \alpha(i)E^i_{curv,j} + \beta(i)E^i_{cont,j} + \gamma(i)E^i_{image,j} \tag{4.12}$$

here $j = 1, 2, ..., m$ denotes the index of a neighbourhood. In addition, $\alpha(i)$, $\beta(i)$, and $\gamma(i)$ are position dependent weighting parameters. Moreover, $E^i_{curv,j}$ and $E^i_{cont,j}$ represent the curvature (stretch) and continuity forces in the internal energy respectively, $E^i_{image,j}$ here is the external energy. The curvature energy term E_{curv} and the continuity energy term E_{cont} are defined as:

$$E_{curv} = \mid v_{i-1} - 2v_i + v_{i+1} \mid^2 \tag{4.13}$$

$$E_{cont} = \mid v_i - v_{i-1} \mid^2 \tag{4.14}$$

where v_i denotes coordinates of the i-th snake point. The external energy term E_{image} normally corresponds to the gradient of an image, as given in equation (4.9). The greedy snake algorithm is to seek a point where $E_{snake,j}$ is minimal among m-neighbours. It iterates until a "termination condition" is met. This can be defined by a max number of iterations or the stability of the position of the points. The computational cost is therefore limited; however, the greedy snake contours become very sensitive to the Gaussian and Salt and Pepper noise.

4.4.4   Gradient Vector Flow (GVF) Snake

The active contour model based on the GVF field was proposed by Xu and Prince [104] to have less sensitivity to initial contour conditions and to solve a related problem that snakes are unable to converge into concave shapes. The GVF field utilises a field of vectors, which is the replacement for the original external force of Kass' snake [100]. For any image pixel *(x, y)*, every vector $V(x, y) = (s(x, y), t(x, y))$ is computed by minimising the energy function:

$$\varepsilon = \iint \mu(s_x^2 + s_y^2 + t_x^2 + t_y^2) + |\nabla f|^2 |V - \nabla f|^2 \, dxdy \tag{4.15}$$

here μ is a regularisation parameter, ∇f denotes the gradient value of the edge map *f* derived from the input image *I(x, y)* and the subscripts denote partial derivatives in regard to the *x* and *y* axes. The ∇f (e.g. the gradients are propagated from targeted object contours to homogeneous areas) will be estimated by *V(x, y)* after the minimisation process. Although the presently processed pixel is far from them, every GVF vector points still towards targeted region contours [106]. For stronger resistance to local noise than the traditional image gradients, the external energy term equation (equation 4.9) is then replaced by the GVF field. The GVF snake therefore could estimate object borders even if some concave parts of targeted object borders exist or the initial mask of the contour is given far from them. The regularisation parameter μ should be restricted to 0~0.25 because the traditional GVF field reaches stable status only with the condition of Courant-Friedrichs-Lewy step-size [104]. In addition, this GVF snake model still needs human interaction (e.g. offering initial masks for snakes).

4.4.5   Active contours without edges (Chan-Vese)

Tony Chan and Luminita Vese (Chan-Vese) introduced a snake model to segment objects in an image by using a combination technique of level sets, curve evolution and Mumford-Shah functional for object estimation [107]. The C-V model can estimate the boundaries of objects with or without gradient, dissimilar to the original active contour model. Furthermore, their model uses a formulation of level set, permitting an initial mask to be set at anywhere in the image and the interior contours to be segmented automatically. (Figure 4.4).

Assume Ω be a bounded open subset of $\mathbf{R}^2$ and *C* be an evolving curve representing the border of the open subset ω of Ω, with $\partial\omega$. The direction N stands for propagating in normal direction.
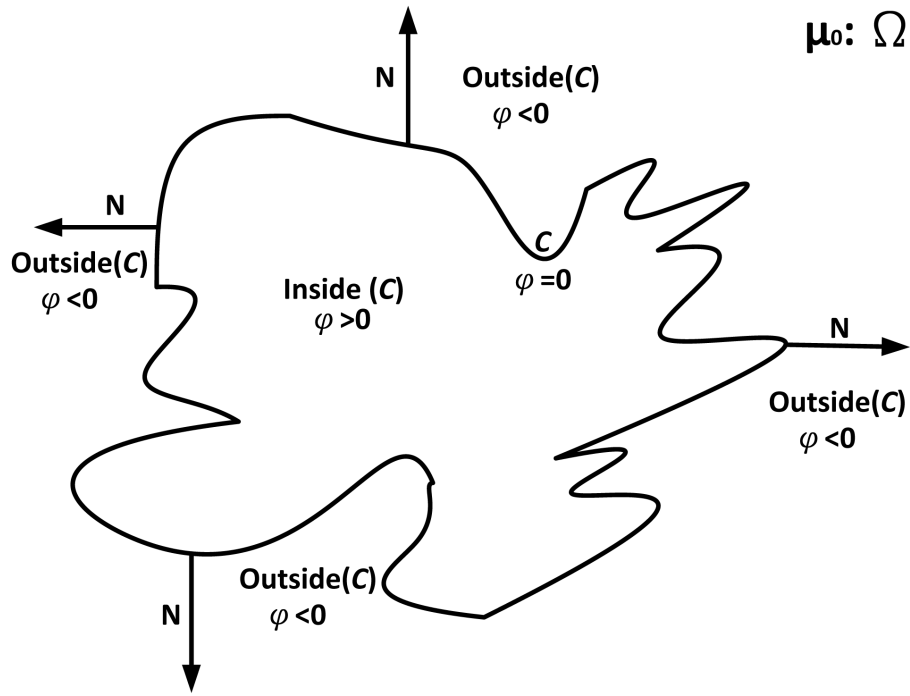
Figure 4.4: *Curve C=(x, y) : $\varphi(x,y)=0$ propagating in all normal directions till it reaches resting points ($\varphi=0$).*

In addition, let u_0: $\Omega \rightarrow \mathbf{R}$ be a given image which is composed of two regions with roughly piecewise-constant intensities. The curve C is defined implicitly by the zero level set of a Lipschitz function $\varphi:\Omega \rightarrow \mathbf{R}$, therefore:

$$\left\{ \begin{array}{c} C = \partial\omega = (x,y) \in \Omega : \varphi(x,y) = 0 \\ inside(C) = \omega = (x,y) \in \Omega : \varphi(x,y) > 0 \\ outside(C) = \dfrac{\Omega}{\omega} = (x,y) \in \Omega : \varphi(x,y) < 0 \end{array} \right\} \tag{4.16}$$

where *x* and *y* represent co-ordinates on a given image μ_0. Its energy function of the image μ_0 can be defined as:

$$F(c_1, c_2, C) = \mu \cdot L(C) + \nu \cdot a((C))$$
$$= \lambda_1 \int_{in(C)} \mid \mu_0(x,y) - c_1 \mid^2 \, dxdy + \lambda_2 \int_{out(C)} \mid \mu_0(x,y) - c_2 \mid^2 \, dxdy \tag{4.17}$$

where c_1 , c_2 are the constants, depending on C, $L(C)$ denotes the length of the curve C , and a represents the area of the inside region, respectively. Other parameters μ, v, λ_1, λ_2 are positive fixed constants. Between the two regions on the image μ_0, the boundary of the object could be detected by the zero-level curve where $\varphi(x, y)$=0.

4.4.6   Other snake models

In original snake model (see Section 4.4.2), minimisation of snake energy is achieved by utilising the calculus of variations. In [108] and [109], a dynamic programming snake model was proposed to tackle the variation problems in computer vision. The balloon model using a Galerkin solution of the finite-element method was proposed [110, 111] for snake energy minimisation. This model considers the contour as an inflated balloon and utilises an internal pressure force to permit the snake to deal with a problem of isolated energy valleys which arise from spurious edge points. The snake models which portray the deformation of contour explicitly as an energy minimising process are classified as energy-minimisation based snakes [100–105]. For more details of the behaviour of energy minimisation please refer to Section 4.4.2. A geometric snake model which depicts contours implicitly as level sets of 2D scalar functions was also proposed [112]. The geometric snakes, implemented by using the level set technique [113–116] and based on the curve evolution theory [117], are deformed via only geometric measures. In this model, a contour is evolved according to a speed function constrained by the inverse of gradient magnitude and governed by the level set curvature, leading into the evolution of snake contour. However, the geometric snake probably ran over the object boundaries and will not return back when the boundaries are broken or have low contrast.

4.4.7   Summary of snake models

As described in the preceding sections, snake models provide a quite useful technique to detect object boundaries. Two primary drawbacks of original snake models, for example, sensitivity to initial conditions and high computational complexity, are almost tackled by GVF and greedy snake models, respectively. However, the initialisation of the snakes, generally executed by human interaction, is not solved yet. The users have to manually offer a contour as the initial mask for snakes. It is not only a time-consuming but also a very tedious task. In addition, different initial snakes may produce different results, making them not reliable enough. As a result, automation of snake initialisation has recently become one of the critical issues in snake

processing. In energy-minimisation based snake models, a momentous task is to adjust the weighting parameters between the external and the internal energy items in order to compromise the behaviour of snake contours with different image contents.

These weighting parameters have to be adaptively adjusted, not only for varing image contents but also during snake iterations because the snake contours are faced with multifarious image data. The parameters setting of original snakes normally requires human experimentation and is invariable all over the whole image. It is crucial to offer space-varying parameters automatically. Hence, in this thesis, one of the primary goals is to provide fully automated snake-based schemes for object contour detection in the fundus image.

4.5 Chapter Summary

In this chapter, a thresholding technique was first introduced. Each pixel in an image is regarded as an "object" pixel if the intensity value of the pixel is higher than a certain threshold value and as a "background" pixel otherwise during the thresholding process. This kind of convention is widely known as a threshold technique. Existing thresholding approaches implemented by five different techniques (e.g. object attribute-based, histogram-based, cluster-based, spatial-based and entropy-based) were listed.

The concept of region growing was then described. Region growing could be regarded as a pixel-based segmentation approach because the selection procedure of initial seed points is involved. This image segmentation method determines whether the neighbouring pixels of initial "seed points" should be merged to the region iteratively. Finally, different types of active contour (snake), including traditional snake, greedy snake, GVF snake and Chan-Vese method, were discussed briefly. As stated in the aforementioned sections, snake models are a useful technique for image segmentation. However, precise initialisation, often set by human experimentation, is usually required for getting reasonable results in different applications. Based on the techniques introduced in this chapter, the necessary background of image processing techniques to this PhD work has been established.

Chapter 5

Optic Disc (OD) and Parapillary Atrophy (PPA) Analysis: Colour Morphology and Chan-Vese Snake

Three different methods to segment PPA and OD region are described in Chapter 5, Chapter 6 and Chapter 7, respectively.

The aim of this chapter is twofold: to implement an aforementioned technique (See Chapter 2) to the OD segmentation and provide a novel method to both segment OD and PPA. The novel technique exploits both red and blue channels of the colour fundus image to strengthen information extraction from features (OD and PPA) whilst keeping interference to a minimum. The PPA and OD region were segmented using the morphological operation and Chan-Vese (MOCV) model.

5.1   Previous work: The GVF Snake on the OD segmentation

By applying a snake to the OD region extraction and comparing the outcome against the ground-truth information labelled by an ophthalmologist, the efficiency of different boundary detection methods can be evaluated. A gradient vector flow (GVF) snake method was proposed [118], described in detail in Section 4.4.4, for segmenting the OD on nine retinal images followed by a minimisation of the effect on the value of the force or of the energy because of high gradient at vessel locations. The results indicate that a GVF-based snake can be used in association with a pre-processed 2D fundus image to extract an accurate boundary of the OD region. The colour images were converted from RGB space to YIQ basis prior to processing.

The pre-processing technique integrates a minima detection scheme and a morphological correction technique together, which yields an intact OD region. For the GVF snake, Mendels *et al.* [118] conducted initial studies of the range of initialisation conditions that offer convergence,

and found that reasonable results can be obtained from quite distant initial conditions (e.g., circles ranging from an estimate half to double the radius of the OD). Three ophthalmologists have reviewed the OD region extracted by Mendels *et al.*'s proposed technique, and consider it as a promising tool for clinical use.

5.2 Proposed Approach: Using Colour Morphology and Chan-Vese Snake on the OD segmentation

5.2.1 Method

The experimental protocol are described in detail in Figure 1.4, Chapter 1. In addition, the steps used in our proposed method, MOCV, are shown (See Figure 5.1)

The variation of the intensity between the brightest parts (e.g. the OD and PPA) and the retinal blood vessels is comparatively high. In particular, the blood vessels are generally at a lower intensity level in regard to the background (See Figure 5.2).

Pre-processing of the image is essential because snake methods only work well on an image with homogeneous regions enclosed by intense gradient information. Applying them directly to the fundus images is extremely difficult, as the area of the OD and PPA is always divided into several regions by the retinal blood vessels. Gray-level morphology operations has been used previously [28, 31, 33, 37, 40, 55] to eliminate the retinal blood vessels to produce a relatively homogeneous region before applying snake methods to the image. Similar morphological operations are equally applicable to the red and blue channels. These two channels were adopted specifically because the blood vessels were found least influential in the red channel and the region of OD-plus-PPA was found most well-defined and less influenced by blood vessels in the blue channel. Pre-processing techniques are therefore applied separately on the red and blue channels in order to segment the OD and the OD-plus-PPA respectively.

5.2.1.1 Average filtering

Average filtering operator was chosen here for two reasons: (a) it could eliminate random noise with less computational cost compared with median filter; and (b) with a large kernel, it could also act as a vessel removal function. On the red channel (Figure 5.3a), the size of the
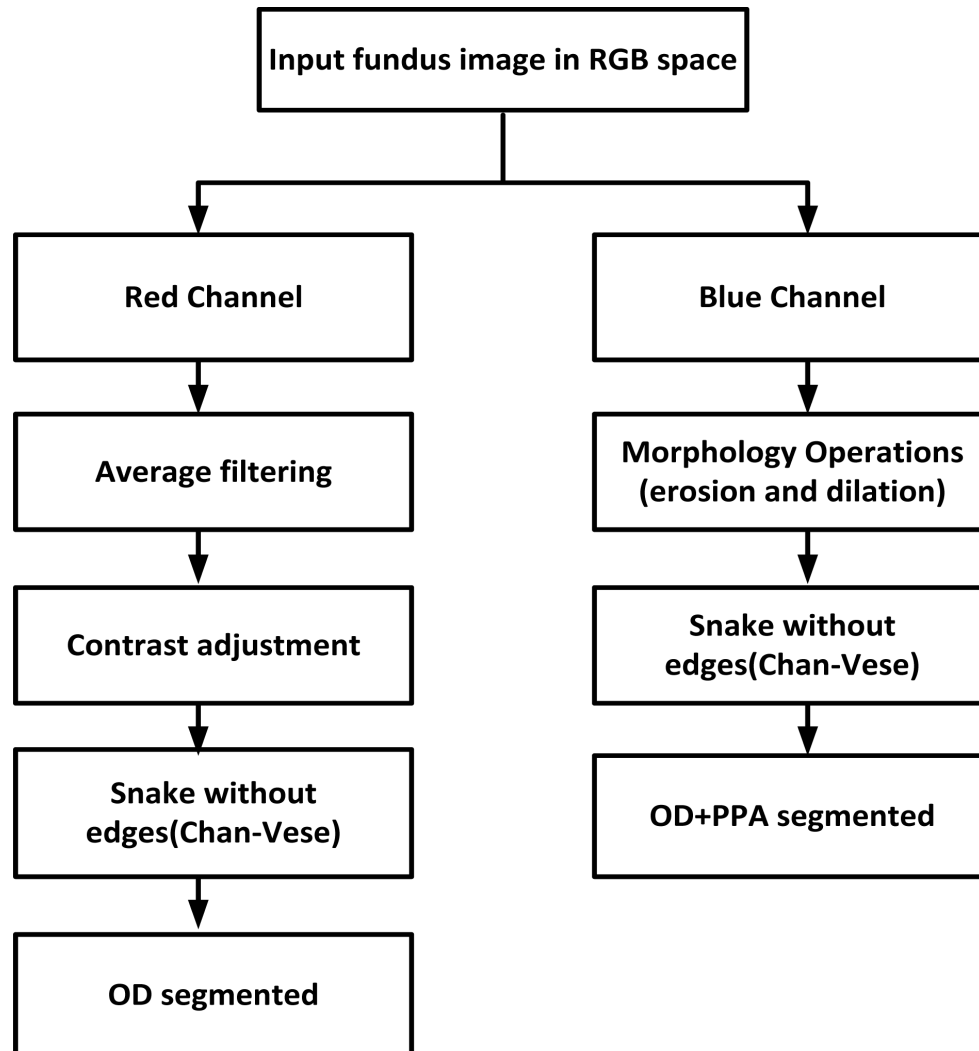
Figure 5.1: *Processing steps of proposed methodology.*
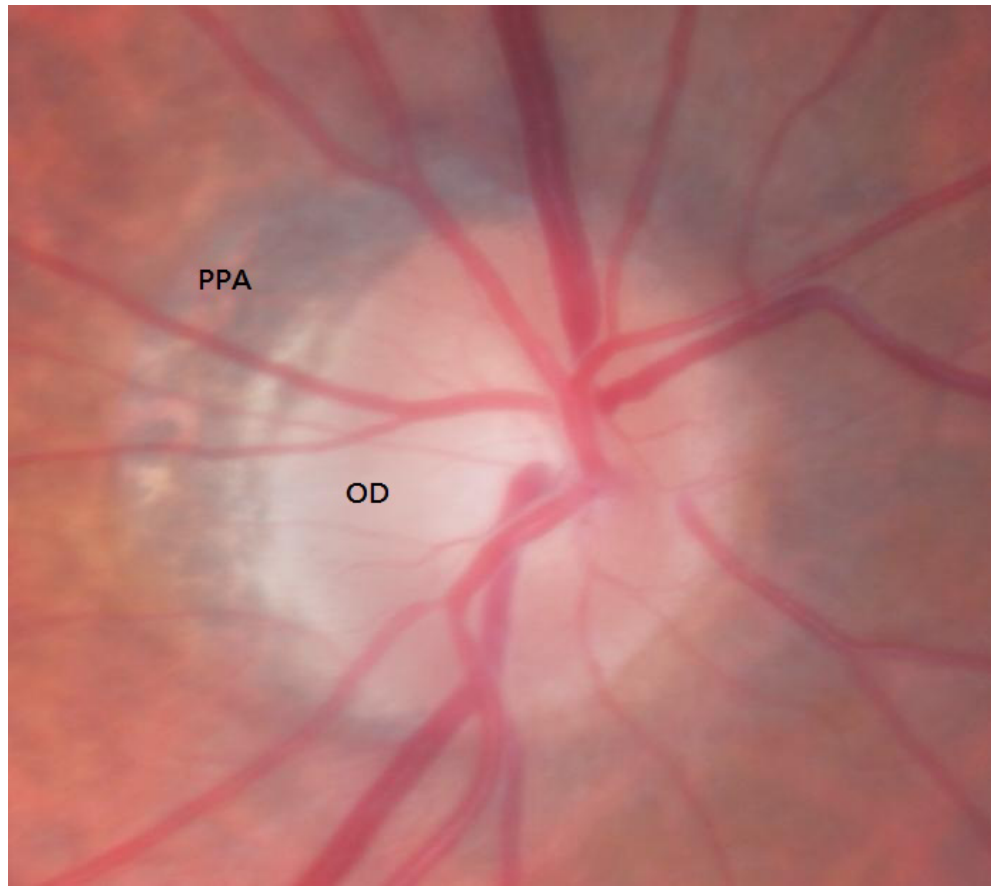
Figure 5.2: *Original fundus image with the OD plus PPA.*

averaging filter is defined as 14×14 pixels, including equal weights of value "1", because the retinal blood vessels are usually smaller than 12 pixels [55]. The retinal blood vessels with low intensity variation are removed by using this operation, whilst keeping the boundary of the OD comparatively unaltered. In addition, the average filter is implemented via the following equation [55]:

$$FI = \frac{1}{m \times n} \sum_{i=1}^{m \times n} R_i \tag{5.1}$$

here m=14 and n=14. The filtered image *FI* is shown in Figure 5.3b.

(a)   **(b)**   **(c)**
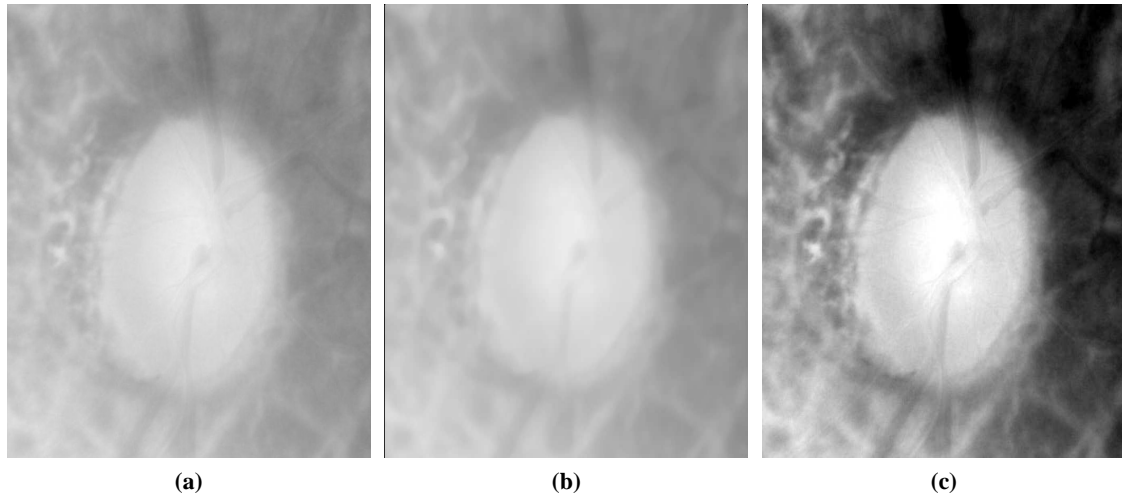
Figure 5.3: *Pre-processing on the Red Channel: (a) original fundus image (b) fundus image after average filtering the vessels have almost removed (c) fundus image after contrast adjustment.*

5.2.1.2   Contrast adjustment

It is more reliable to work on the red channel because there is a good contrast between the OD region and the background. To make the OD more distinguishable from the background, a typical contrast modification operation was applied to the images. The intensity values in grayscale image, Figure 5.3b, to new intensity values in the adjusted image, Figure 5.3c, such that 1% of data is saturated at low and high intensities of the grayscale image, Figure 5.3b. This increases the contrast of the adjusted image, Figure 5.3c.

5.2.1.3   Morphological operations

Standard morphological operations (erosion and dilation) were used to first remove the retinal blood vessels in the OD region and then to restore the boundaries back to their original positions. The original fundus image is shown in Figure 5.4a. A symmetrical circular shape structuring element of erosion or dilation operator with 14 pixels was set here. Intuitively, dilation operation expands the retinal blood vessels and erosion operation shrinks it. Therefore, the combination of erosion and dilation can alleviate the effects of blood vessels that have fewer than 14 pixels, as illustrated in Figure 5.4b.

(a)   **(b)**
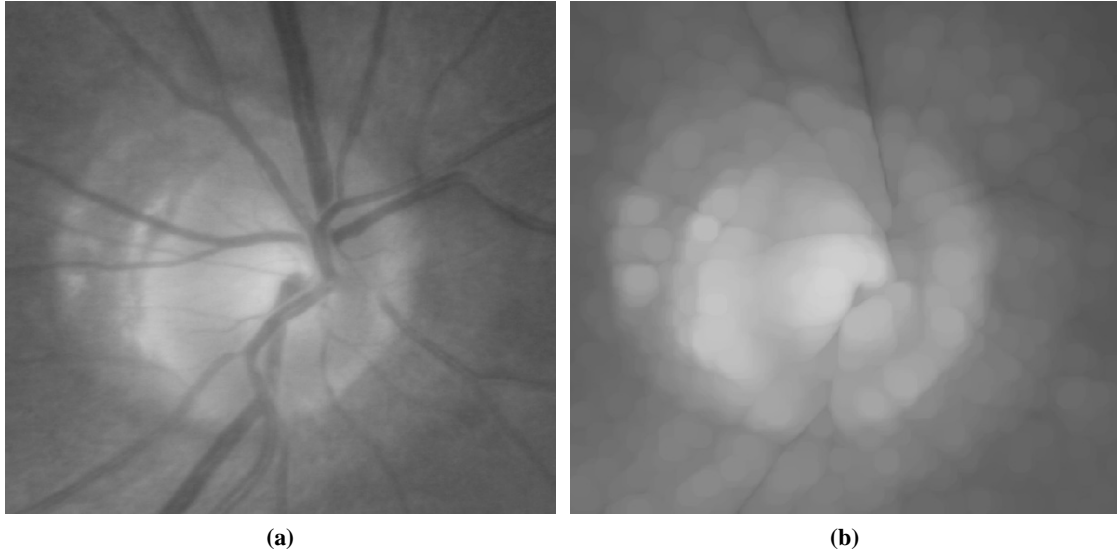
Figure 5.4: *Pre-processing on blue channel: (a) original fungus image, and (b) after operation most vessels have been removed.*

5.2.1.4   Chan-Vese Snake

Previously, although GVF snake has been applied to detect OD boundary, it performed poorly when the condition of PPA was present. Topological changes, corners and cusps due to the PPA complicated the task. The Chan-Vese [107] was thus adopted, described in detail in Section 4.4.5, to estimate objects whose contours are not necessarily defined by gradient. In addition, the energy function of the image μ_0 can be defined as:

$$
\begin{aligned}
F(c_1, c_2, C) &= \mu \cdot L(C) + \nu \cdot a((C)) \\
&= \lambda_1 \int_{in(C)} \mid \mu_0(x, y) - c_1 \mid^2 dxdy + \lambda_2 \int_{out(C)} \mid \mu_0(x, y) - c_2 \mid^2 dxdy
\end{aligned}
\tag{5.2}
$$

here *C* is any other changing curve, and c_1 , c_2 are the constants, depending on *C*, *L(C)* denotes length of the curve *C* , and *a* represents the area of the inside region, respectively. Let that the image μ_0 is formed by two regions of approximatively piecewise-constant intensities. Other parameters μ, v, λ_1, λ_2 are positive fixed constants. In our application, we experimentally set the step size of the energy function Equation (5.2) at 0.5 to ensure our snakes stopped at the desired boundary.

5.2.2 Experimental Results and Discussions

The colour fundus photograph images from a database of a well characterised cohort [22] was used for the experiments. In order to assess the performance of the proposed model for detecting the OD boundary, the results of the proposed approach were compared with the results obtained from the GVF snake method [55]. For the GVF snake method, Osareh *et al.* applied morphological operations on the images for pre-processing, and experimentally set the parameters of energy functions to balance the accuracy and the smoothness of the final contour. Fundus images were specifically classified into two categories, i.e. normal retinal images with the OD, and abnormal retinal images with the OD plus PPA.

The results are shown in Figure 5.5. The first column shows the results obtained from the normal retinal images. Results of abnormal retinal images (i.e. with PPA) are given in the second column. Viewing row by row, the first row (a & b) shows the original fundus images. The second row (c & d) presents the results of GVF snake method. The last row (e & f) presents the results based on the proposed MOCV model.

Compared to the GVF snake method, the MOCV has the following merits: (1) It is less susceptible to the interference effect of blood vessels (2) it makes no prior assumption about the shapes of the OD and PPA, (3) it provides a more accurate description of the boundaries.

The accuracy of the contour localisation against the manually marked ground-truth information drawn by an ophthalmologist for all variations of the OD and PPA morphology has been quantified and compared. An effective overlap measure (M) has been used here [55], described in detail in Section 2.3, of the match between estimated region and ground-truth as:

$$M = \frac{N(R \cap T)}{N(R \cup T)} \tag{5.3}$$

here *R* and *T* are equivalent to the ground estimate and the final iteration of snake-localised boundary respectively and *N(.)* denotes the number of pixels within the targeted regions.

In addition, the results of the randomly selected fundus images in 20 images are shown in Table
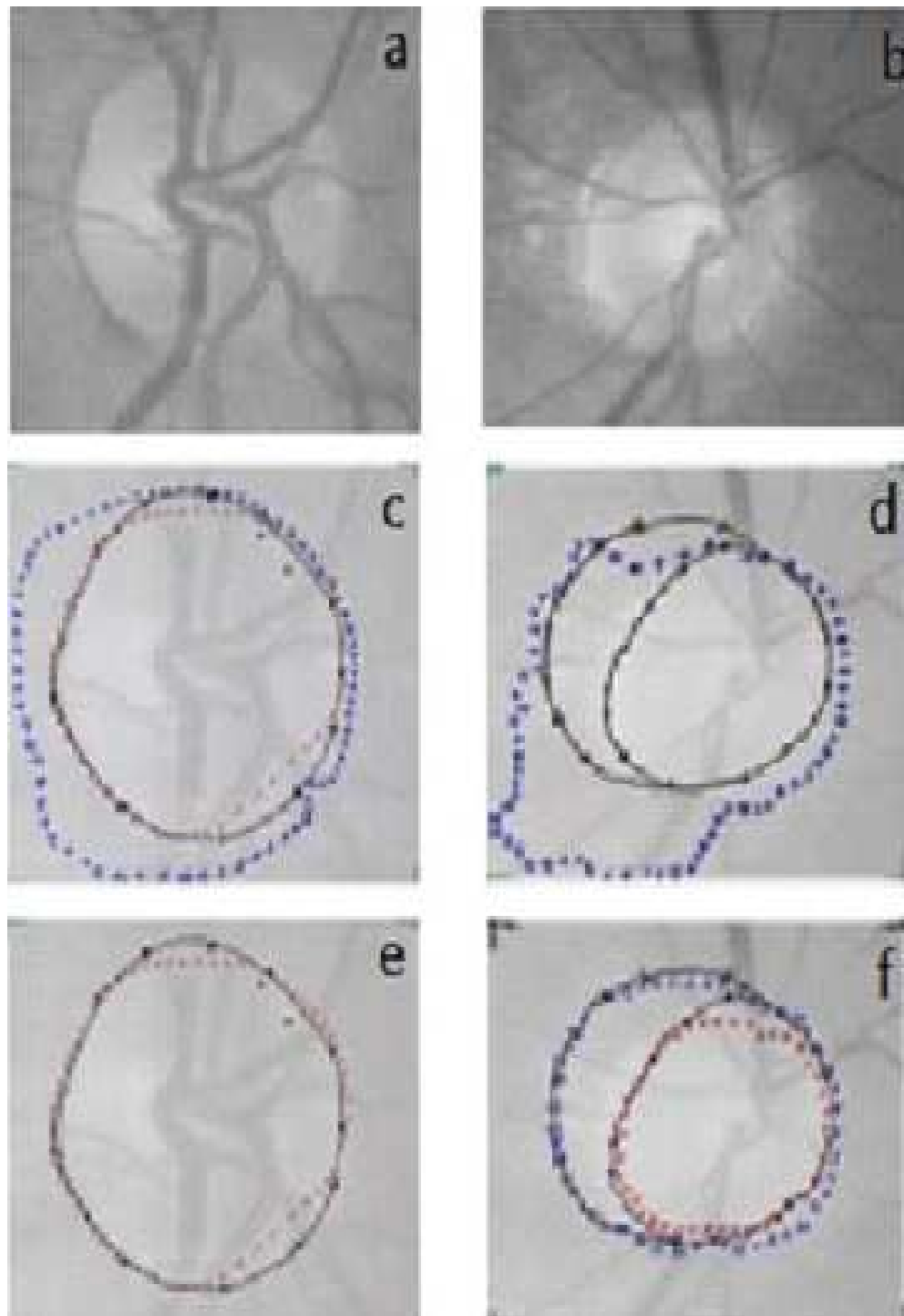
Figure 5.5: *First row (a), (b): Example images with a close view of OD with/without the conditions of PPA; Second row (c), (d): Results from GVF snake method; Last row (e), (f): Results from MOCV method.*

5.1. The results from the MOCV method were better (almost double in mean accuracy) than the ones from the GVF-snake method. The MOCV additionally provided a means to extract the PPA region.

Results	GVF-snake	MOCV
Mean accuracy (%)	44.62	86.65
Standard Deviation	9.85	8.97

Table 5.1: *The Statistical Results of OD Segmentation in 20 Images*

5.3   Chapter Summary

In this chapter, a novel approach, MOCV, has been described for segmenting the OD and PPA automatically in fundus images. The performance of the MOCV has been evaluated using a set of standard retinal fundal photograph images. Compared to the published works, experimental results showed that the MOCV performed better in detecting the OD and, for the first time, demonstrated successfully the detection of the boundary between the OD and PPA in a retinal image. The MOCV can estimate the OD contours of those bright objects with accurate contours with a mean accuracy level of 86.65% (S.D.=8.97). For early diagnosis of ophthalmological diseases, the model described in this chapter is potentially very promising in computer-aided screening system. Moreover, by providing a way to detect the region of PPA, a new dimension is added to the standard eye-diagnosis.

Chapter 6
Optic Disc (OD) and Parapillary Atrophy (PPA) Analysis: Multiple image processing techniques

In Chapter 5, an attempt to segment the Parapillary Atrophy (PPA) and Optic Disc (OD) using morphological operations and the Chan-Vese model was described. The MOCV method is promising in segmenting the OD region; however there is still room for an improvement. This chapter introduces another novel technique to define the size of the OD and PPA, which provides more accurate results.

The novel technique, named MULIPT, exploits both red and blue spaces of the colour fundus image to maximise information extraction from features (OD and PPA) whilst keeping interference (e.g. blood vessels and artifacts) to a minimum. The OD region was segmented using the Chan-Vese model with an elliptical shape constraint. This region was then removed from the image (OD-plus-PPA), which was cropped using a modified Chan-Vese method, yielding a first-order estimation of the PPA region. Its boundary was subsequently refined by using scanning filter, thresholding and multi-seeded region growing methods. Much of the work described and discussed in this chapter has been previously published in [119, 120].

6.1 Background Study: Chan-Vese Snake with elliptical constraint on the OD segmentation

Because the OD appears more or less an ellipse or a circle, Tang [121] proposed a modified C-V model which included an elliptic shape constraint imposed on zero-level set function in C-V model (Described in detail in Section 4.4.5). The new "fitting energy" function E is then:

$$inf\{E[c_1, c_2, \varphi|\mu_0]\} = \alpha \int_\Omega (\mu_0 - c_1)^2 H(\varphi) + (1 - \alpha) \int_\Omega (\mu_0 - c_2)^2 (1 - H(\varphi)) \quad (6.1)$$

Subject to

$$\varphi = 1 - [\frac{((x - x_0)\cos\theta + (y - y_0)\sin\theta)^2}{a^2} + \frac{(-(x - x_0)\sin\theta + (y - y_0)\cos\theta)^2}{b^2}]^{\frac{1}{2}} \quad (6.2)$$

where

Lipschitz function $\varphi : \Omega \to \Re$ of $\boldsymbol{R}^2$,

$\alpha > 0$ is a fixed parameter,

$H(\varphi)$ denotes the Heaviside function.

x_0, y_0, θ, major axis *(a)* and minor axis *(b)* denote the ellipse parameters at the parameters of the ellipse at φ=0.

In addition, the evolutions related to the Euler-Lagrange equations are:

$$\left\{ \begin{array}{l} \frac{da(t)}{dt} = -\int_\Omega [\alpha(\mu_0 - c_1)^2 - (1 - \alpha)(\mu_0 - c_2)^2]\delta(\varphi)A(\frac{1}{a^3})dxdy \\[2mm] \frac{db(t)}{dt} = -\int_\Omega [\alpha(\mu_0 - c_1)^2 - (1 - \alpha)(\mu_0 - c_2)^2]\delta(\varphi)B^2(\frac{1}{b^3})dxdy \\[2mm] \frac{dx_0(t)}{dt} = -\int_\Omega [\alpha(\mu_0 - c_1)^2 - (1 - \alpha)(\mu_0 - c_2)^2]\delta(\varphi)Ldxdy \\[2mm] \frac{dy_0(t)}{dt} = -\int_\Omega [\alpha(\mu_0 - c_1)^2 - (1 - \alpha)(\mu_0 - c_2)^2]\delta(\varphi)Mdxdy \\[2mm] \frac{d\theta_0(t)}{dt} = -\int_\Omega [\alpha(\mu_0 - c_1)^2 - (1 - \alpha)(\mu_0 - c_2)^2]\delta(\varphi)Ndxdy \end{array} \right\} \quad (6.3)$$

where, $\delta(\varphi)$ denotes the Dirac function and

$c_1 = (\int_\Omega \mu_0 H(\varphi)dxdy)/(\int_\Omega H(\varphi)dxdy)$

$c_2 = (\int_\Omega \mu_0 (1 - H(\varphi))dxdy)/(\int_\Omega (1 - H(\varphi))dxdy)$

$A = (x - x_0)\cos\theta + (y - y_0)\sin\theta$

$B = -(x - x_0)\sin\theta + (y - y_0)\cos\theta$

$L = A\cos\theta/a^2 - B\sin\theta/b^2$

$M = A\sin\theta/a^2 + B\cos\theta/b^2$

$N = AB[1/b^2 - 1/a^2]$

with a condition of

$$\varphi_0(x, y) = 1 - \frac{\sqrt{(x - x_c)^2 + (y - y_c)^2}}{R} \tag{6.4}$$

Also, the initial conditions of the equation (6.3) could be set as follows:

$$\left\{ \begin{array}{l} a(t) \mid_{t=0} = R, \\ b(t) \mid_{t=0} = R, \\ x_0(t) \mid_{t=0} = x_c, \\ y_0(t) \mid_{t=0} = y_c, \\ \theta(t) \mid_{t=0} = 0.0, \end{array} \right\} \tag{6.5}$$

here *R* is a positive constant. Therefore, the steady solution of equation (6.2 and 6.3) at time *T*:

$$1 = [\frac{((x - x_0(T)) \cos(\theta(T)) + (y - y_0(T)) \sin(\theta(T)))^2}{(a(T))^2}$$
$$+ \frac{(-(x - x_0(T)) \sin(\theta(T)) + (y - y_0(T)) \cos(\theta(T)))^2}{(b(T))^2}]^{\frac{1}{2}} \tag{6.6}$$

Tang *et al.*'s model was examined with the 50 trials, including 20 poor quality (low contrast) fundus images. The performance of their model in detecting the OD region and in computing its shape is robust to noise and the OD deformity. However, the model failed to estimate the OD shape as the OD feature acquired in red channel is insufficient.

6.2 Segmentation and Quantification Tool for the Size of OD and PPA region

6.2.1 Proposed Method

The experimental protocol are described in detail in Figure 1.4, Chapter 1. The original software code of implementation of Chan-Vese algorithm was downloaded from MATLAB CEN-TRE and the rest of scripts were written by Cheng-Kai Lu. The variation of the intensity between the bright objects (e.g. the PPA and the OD) and the retinal blood vessels of the fundus image was relatively high (see Figure 6.1a). Conversely, the blood vessels were in general at a lower intensity level with respect to the background.
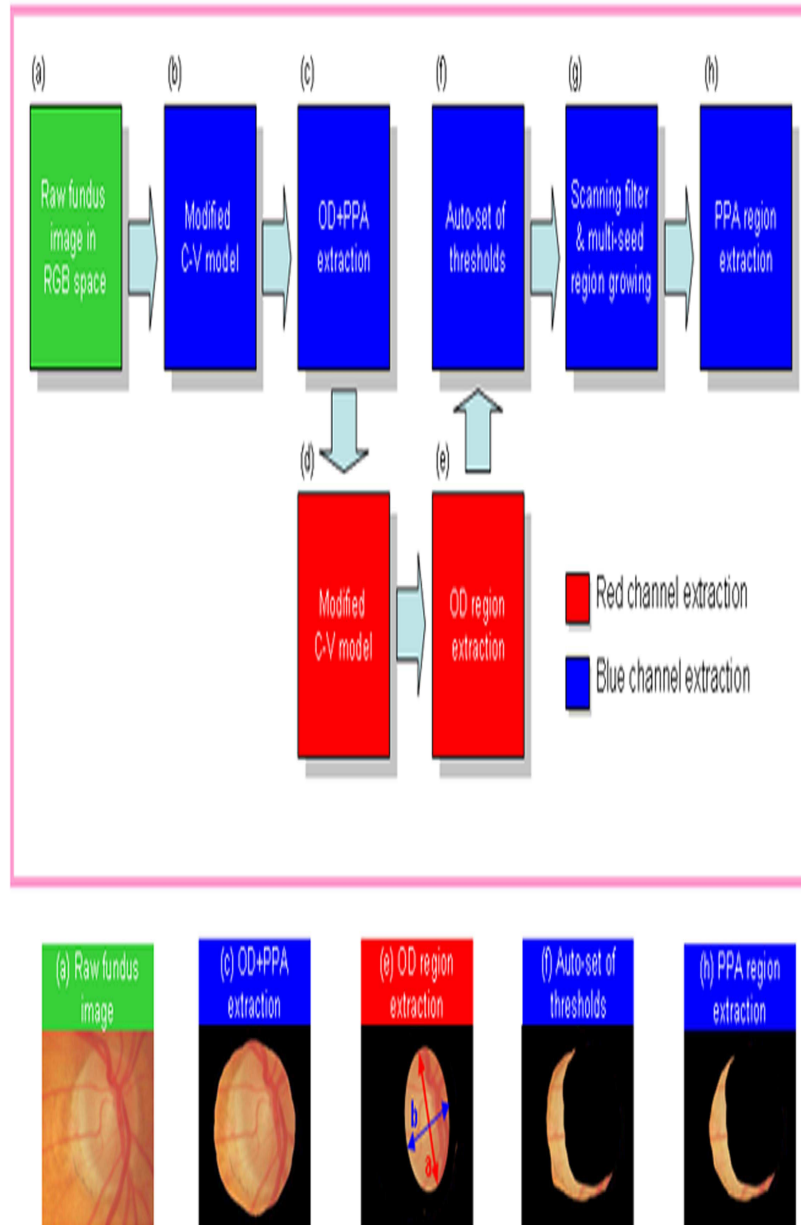
Figure 6.1: *Flow chart shows the extraction of the PPA and the OD regions.*

The proposed algorithm, MULIPT, combined a collection of image processing techniques (Figure 6.1).

1. Channel Selection:

The OD region could be reliably detected in the red channel as it appeared brighter than the rest of the fundus image while the blood vessels appeared least influential [37]. The region consisting of both the OD and the PPA (hereafter referred to as the region of OD-plus-PPA) was also well-defined in the blue channel. Therefore, fundus images were initially pre-processed in two channels (Red and Blue) of the RGB space to reduce the interference of blood vessels and to better distinguish the regions of OD and PPA.

2. OD-plus-PPA region segmentation:

The OD-plus-PPA was segmented by a modified C-V model in the blue channel (Figure 6.1b and c).

3. OD region segmentation:

A variant of the C-V model with a shape restraint was applied to segment the OD region in the red channel (Figure 6.1d and e). In this case, the restraint was based on an ellipse reflecting the actual shape of an OD. Here, the fixed parameter, α , of the C-V model is the experimentally set at 0.6.

4. PPA region segmentation:

The first order estimation of PPA region was produced by removing the OD region from the region of OD-plus-PPA. Moving back to the blue channel, the segmented image was then equally divided into four zones automatically. Based on the auto-set thresholds acquired from each zone, the image was then filtered to reduce the influence of crossing vessels and artefacts (Figure 6.1f). Finally, the PPA region was extracted by using a multi-seed region growing method [99] (Figure 6.1g).

A. OD-plus-PPA region and OD segmentation using modified C-V Model

As the OD region appears to be more or less an ellipse, Tang's model [121] which integrated the C-V model with an elliptical shape constraint was adopted. It was also used to segment the OD-plus-PPA region. However, the PPA region may sometimes appear in an irregular shape, so

the rules for the evolution of the C-V model had to be modified slightly. The set of starting C-V model points, also known as the initial mask, was arranged to be in an ellipse as per normal. However, the model was then allowed to deform freely as it edged closer to the boundary of the OD-plus-PPA in each subsequent iteration. This allowed the model to produce an enclosed but not necessarily elliptical shape, which was always bigger than the exact region of the OD-plus-PPA.

Next, Tang's C-V model was exploited to detect the OD region. In order to accurately segment the OD, two modifications to the model were introduced. Firstly, Tang's equation (6.3) was restored to its original form (of an ellipse):

$$\frac{da(t)}{dt} = -\int_{\Omega}[\alpha(\mu_0 - c_1)^2 - (1-\alpha)(\mu_0 - c_2)^2]\delta(\varphi)A^2(\frac{1}{a^3})dxdy \qquad (6.7)$$

Secondly, a new way to automatically detect the centre of OD for more accurate segmentation was introduced. The raw image was divided into four sub-regions. Then, the approach used in Tang's model to estimate the initial mask centre (x_0, y_0) was adopted. The initial function was chosen as equation (6.4)

In equation (6.4), *R* is the estimated radius of the OD and could be simply taken as:

$$R = min(min[x_0/2, (w - x_0)/2], min[y_0/2, (h - y_0)/2]) \qquad (6.8)$$

here *w* and *h* are the width and height of an image respectively.

Then, the algorithm automatically calculates the offset, f_x and f_y, of the initial mask centre (x_c, y_c), based on the histogram of intensity value of each of the four regions. The updated initial mask centre is thus:

$$(x'_0, y'_0) = (x_0 + f_x, y_0 + f_y) \qquad (6.9)$$

B. Auto-set of Thresholds and Scanning Filter

In order to eliminate the unwanted pixels in the over-sized OD-plus-PPA region, threshold values from the histogram of intensity values in the four sub-regions were acquired. In this

context, the threshold was set by the brightest 30% of all pixels in each region. This produced a better-defined OD-plus-PPA region. The OD region was then subtracted resulting in the first order estimation of the PPA region as illustrated in Figure 6.1f.

The PPA region is a non-homogeneous region divided into multiple sections by a few crossing blood vessels. We therefore proposed the use of a scanning [1x3] filter to create a path through the vessels for the following region growing model to reach different sections of the PPA.

C. Multi-Initial Seed Region Growing

The seeded region growing technique was first introduced by Adams and Bischof [99]. It starts with several initial seeds and then adds adjacent points as new seeds, beginning with the points of lowest priority. The priority is defined by a distance function. The distance of each pixel to a contiguous region [31] is defined by:

$$R(x, \delta_i) = [I(x) - mean_j \in \delta_i(I(j))] \qquad (6.10)$$

where *I(x)* is the gray image value of the point x(element) δ and δ_i the region labelled *i*. Setting both the right initial seed and distance function are some of the most important steps in PPA extraction.

The algorithm automatically placed one initial seed in each of the four sub-regions and experimentally set an optimal distance function at the value of 0.45 for each sub-region. Each seed was then allowed to grow until the regional threshold distance set by equation (6.10) has been met. Finally, the results at all four sub-regions were combined to produce an integrated PPA region. By combining the techniques listed above, our methodology permitted the full use of both global and local information for PPA and OD segmentation.

6.2.2   Experimental Results

For the experiments, colour retinal images drawn from the Lothian Birth Cohort (LBC), a 1936 study described in Section 1.4 were used. A total of 94 colour fundus images (including 18 poor quality images as determined by an independent and experienced human assessor) from 66 subjects were randomly selected. Without knowing the segmentation results from the proposed tool, the human assessor provided the ground estimate of the OD and the PPA region in

<p align="center">(a)   (b)</p>
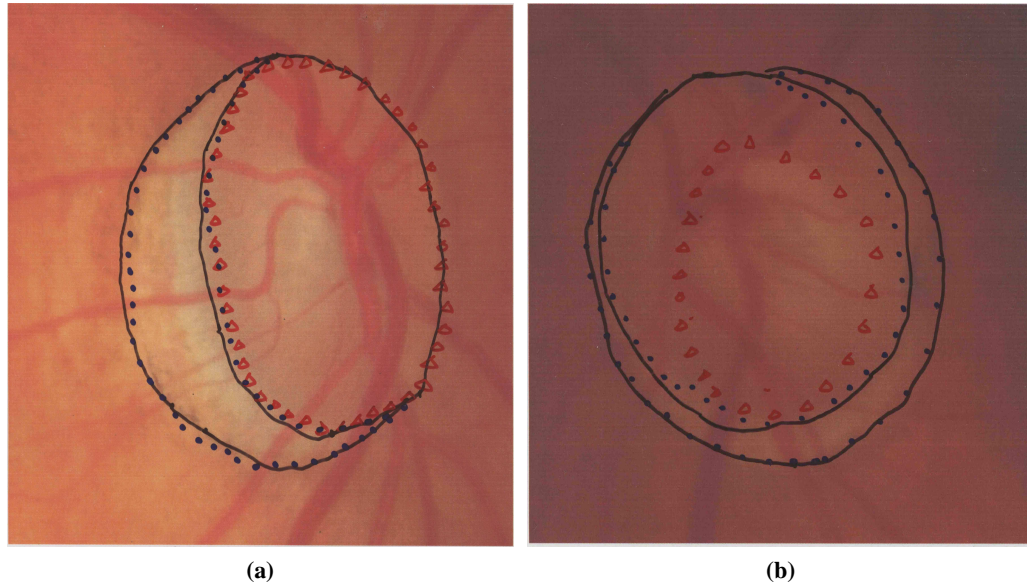
Figure 6.2: *Two segmentation results from the proposed algorithm. Shown are (a) good-quality and (b) poor-quality images.* Black solid line*: the ground estimate;* black dots *and the* red triangle:*the estimated PPA and OD regions, respectively.*

the images. Subsequently, the area enclosed by the ground estimate was counted pixel by pixel with a commercial software package Photoshop (Adobe Systems Inc., San Jose, CA, USA) to quantify the size of each region. This was repeated with the segmentation results from the tool.

Figure 6.2 and Figure 6.3 show two and six samples from the segmentation results of the MULIPT, respectively. In both Figure 6.2 and Figure 6.3, the first column depicts the results obtained from good quality images while the second column depicts the results from poor quality images. The ground estimate is drawn on the black solid line. The results of estimated PPA and OD region are enclosed by the spots and red markings, respectively.

Figure 6.4a shows the comparison of the OD area size (in arbitrary pixel units), based on the ground estimate, and the estimated OD area size, determined by the proposed tool in the 94 trials, with a line of best fit. Figure 6.4b shows a similar graph but for the PPA area size estimation.

The results suggest that the MULIPT was able to detect the general boundary of OD and PPA. However, it tended to terminate the snake evolution prematurely on all good quality images; hence the results appeared to under-estimate the actual size. This is less consistent in the case
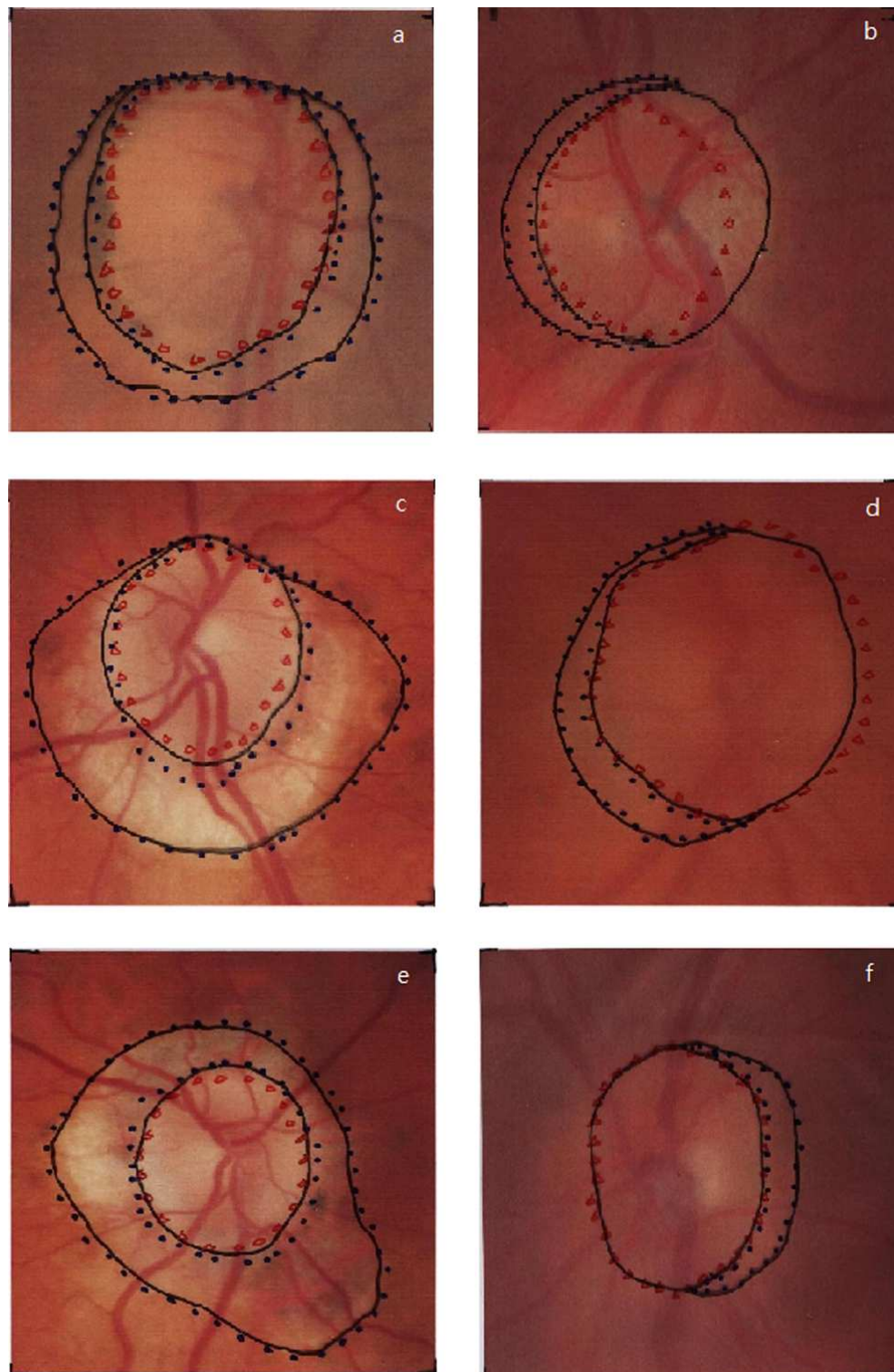
Figure 6.3: *Six segmentation results from the proposed algorithm. Shown are (a, c, e) good-quality and (b, d, f) poor-quality images.* Black solid line*: the ground estimate;* black dots *and the* red markings*: the estimated PPA and OD regions, respectively.*
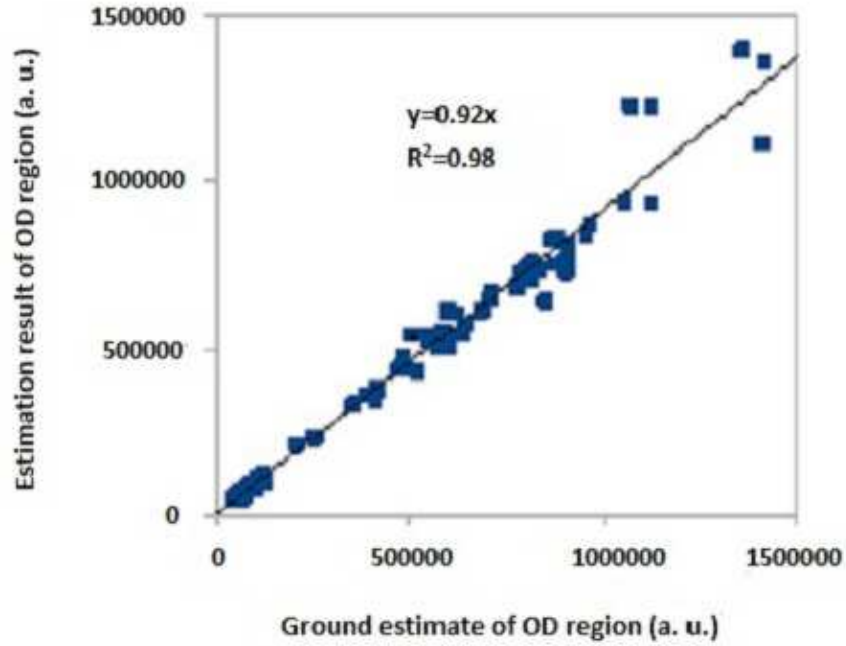
(a)
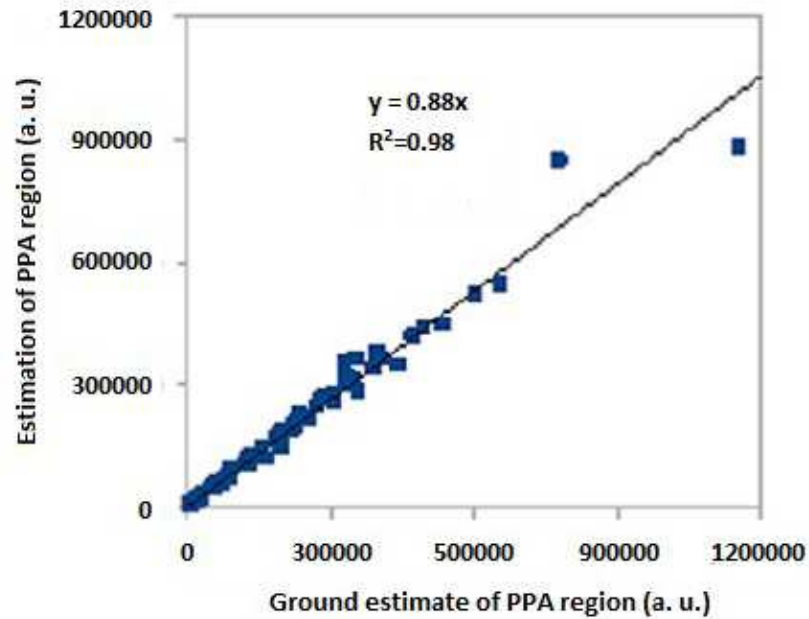
(b)

Figure 6.4: *The correlation between the ground estimate (x-axis) and the results obtained by the proposed MULIPT tool (y-axis) in quantifying the size of each region, in arbitrary pixel unit. (a), (b): direct estimation results of OD and PPA from the tool, respectively. The correlation coefficient is found to be 0.98 in both cases.*
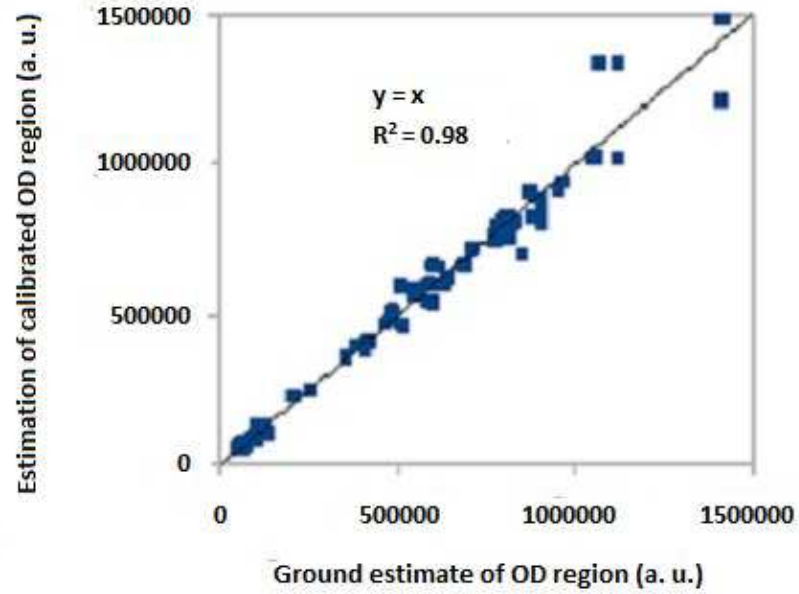
(a)
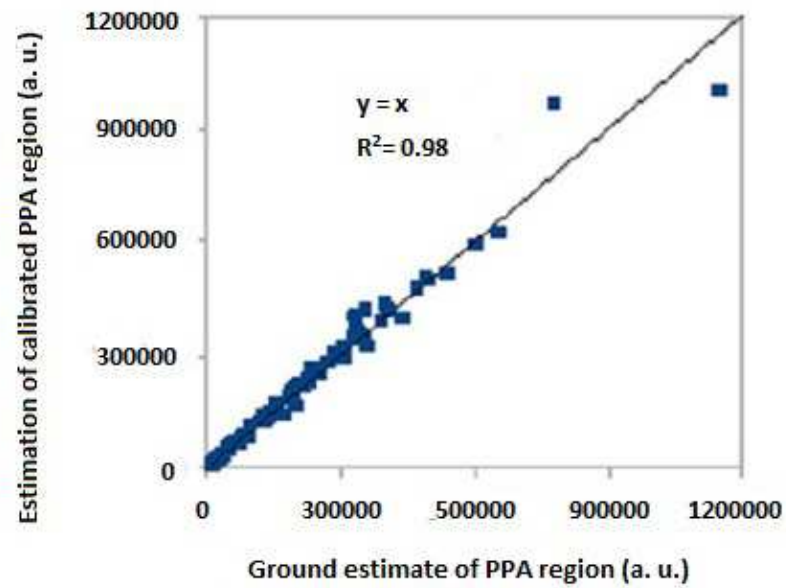
(b)

Figure 6.5: *The correlation between the ground estimate (x-axis) and the results obtained by the proposed MULIPT tool (y-axis) in quantifying the size of each region, in arbitrary pixel unit. (a),(b): estimation results of the OD and PPA region after calibration such that y=x. The correlation coefficient is found to be 0.98 in both cases.*

of poor quality images where the intensity variation/resolution in defining the boundary of OD is limited. Figure 6.3d shows a good example when the model missed the mark by pushing the boundary into the scleral rim. Overall, it appears that most of the estimation results in the 94-trials are under-estimated. This is confirmed by the gradients (both<1) of the best-fit lines in Figure 6.4a and Figure 6.4b. Therefore the estimation model was calibrated using these values as scaling factors. The final estimation results are plotted in Figure 6.5a and Figure 6.5b. As shown, a correlation coefficient of 0.98 (max=1) is achieved in the size estimation of both the OD and PPA region. This suggests that the estimation is not stochastic but fairly consistent with the ground estimate defined by an ophthalmologist (i.e. the best-fit line is defined by the equation y=x).

	Before Calibration		After Calibration	
Results	PPA	OD	PPA	OD
Mean accuracy (%)	88.2	90.0	93.8	94.0
Standard Deviation	5.85	6.20	5.26	5.88
Correlation coefficient, R^2	0.98	0.98	0.98	0.98

Table 6.1: *The Statistical Results of PPA and OD Segmentation in 94 Trials*

6.2.3 Validity of the Proposed Method

Three methods were used to validate the proposed MULIPT model. Firstly, the mean accuracy (*M.A.*) of the model was calculated, which is given by:

$$M.A. = [1 - \frac{\sum_{i=1}^{n}[\frac{S_a - S_e}{S_a}]}{n}] \times 100\% \tag{6.11}$$

where *Sa* represents the actual size (ground estimate) of PPA or OD, while *Se* represents the estimated size (by our model) of PPA or OD. The numerical value *n* is the total number of images analysed in the experiment. Prior to calibration, the estimation model achieved a mean accuracy level of 90.0% (S.D.=6.20) and 88.2% (S.D.=5.85), in defining the size of OD and PPA respectively. With the same set of colour fundus images, the estimation model after calibration achieved a mean accuracy level of 94.0% (S.D.=5.88) and 93.8% (S.D.=5.26).Table 6.1 summarises the segmentation results on 94 images.

Secondly, the sensitivity of the estimation model at different tolerance levels was calculated. In this context, tolerance level refers to the percentage of estimation error being acceptable. When the estimation result by this model falls within the range of tolerance, it was counted as one correct prediction, and vice versa. The sensitivity is defined as the percentage of correct predictions over the total number of images analysed in the experiment. Clinically, the acceptable tolerance level varies from application to application. For example, the OD appearance has a strong relationship with visual field deficits, the lower tolerance level is therefore probably essential for monitoring ocular diseases. On the other hand, the higher tolerance level is probably reliable enough for medics to oversee diabete. Therefore, two tolerance level, 10% and 15%, were presumably set in the validation. The model after calibration achieved a sensitivity of 75.5% (tolerance= 10%) and 90.4% (tolerance= 15%) in estimating the size of OD region. As expected, the sensitivity level is lower when the tolerance is smaller, and when the model is not calibrated (see Figure 6.6a). The scattering plots in Figure 6.6b show a similar trend. After calibration, the sensitivity of the model for the PPA region is 84.0% (tolerance= 10%) and 92.6% (tolerance= 15%) respectively.

Third and finally, the robustness of the calibration method was evaluated for the estimation model. 70 of the 94 images were randomly selected and a suitable scaling factor to calibrate the segmentation results was derived, according to the aforementioned methodology. Then the remaining 24 images were used to obtain the accuracy of the calibrated model. In this case (labelled as 'RA'), the mean accuracy is 94.0% (S.D.=5.77) and 94.3% (S.D.=4.53) in defining the size of OD and PPA respectively in the 24 test images. This experiment was repeated by (a) calibrating the proposed model with images that have the largest (70/94=74.5%) PPA and having remaining images from the dataset, i.e. those with the smallest (24/94=21.3%) PPA as test images, and (b) calibrating with the smallest (74.5%) PPA and testing with the largest (21.3%) PPA. The earlier (labelled as 'HI') achieved a mean accuracy of 92.7% (S.D.=7.53) and 92.8% (S.D.=4.93) for size estimation of the OD and PPA region, respectively.

On the other hand, the latter (labelled as 'LO') achieved a mean accuracy of 93.7% (S.D.=6.98) and 93.4% (S.D.=6.57) for the OD and PPA. Table 6.2 summarises the results, including the previous results from calibrating with all 94 images (labelled as 'AL'). As expected, the model performs the worst when it is calibrated with the largest PPA images and tested with the smallest PPA images. However, the mean accuracy of the proposed model is still greater than 92.7%.
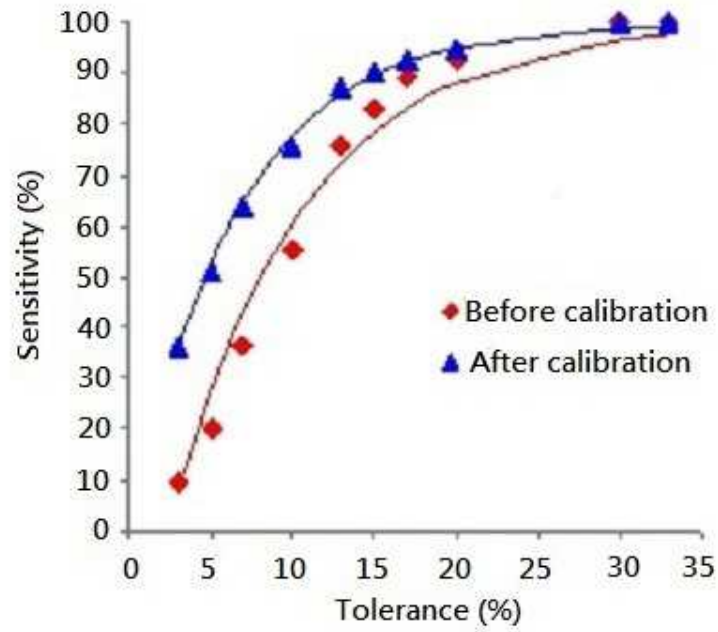
(a)
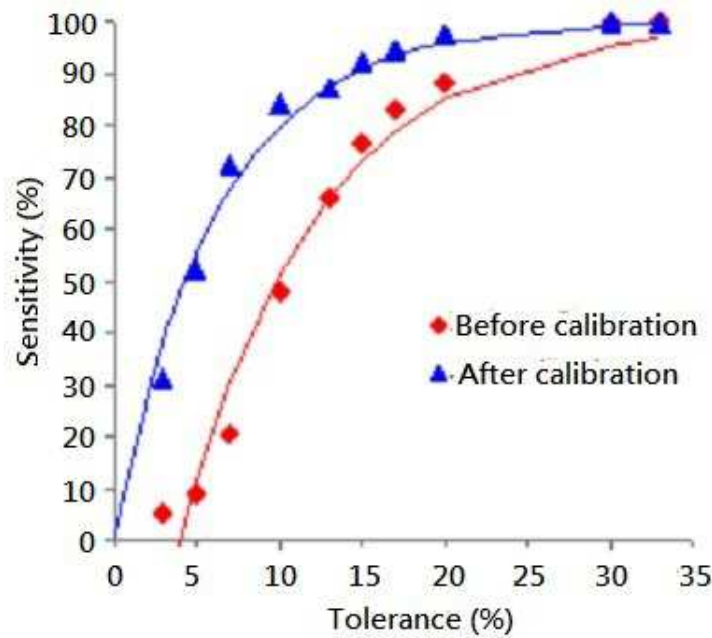
(b)

Figure 6.6: *The sensitivity of the proposed tool in defining the size of (a) the OD and (b) the PPA regions at different tolerance levels in the 94 trials. The slopes represent in best fit for the scatterplots.*

	OD				PPA			
	HI	RA	LO	AL	HI	RA	LO	AL
Scaling factor	0.92	0.91	0.90	0.92	0.88	0.87	0.89	0.88
Correlation coefficient, R^2	0.97	0.98	0.99	0.98	0.97	0.97	0.99	0.98
Mean accuracy (%)	92.7	94.0	93.7	94.0	92.8	94.3	93.4	93.8
Standard Deviation	7.53	5.77	6.98	5.88	4.93	4.53	6.57	5.26

Table 6.2: *The Statistical Results of PPA and OD Segmentation in Results in Different Combinations of Calibration and Test Images*

6.2.4 Discussions

Automated software has been developed to measure the size of the PPA and OD in a 2D fundus image. The experimental results with a very wide variety of fundus images showed that the proposed algorithm was not only robust for automatic PPA shape detection and area quantification, but it could also provide the transverse and conjugate diameter of the OD as well as PPA-to-OD ratio, which may be useful in early detection and grading of eye conditions such as glaucoma.

The automatic detection and the quantification of OD in fundus image are particularly important tasks in this retinal image analysis for two reasons: Firstly, the OD has similar attributes to the PPA, both in terms of contrast and brightness, making their boundary detection a difficult task. Secondly, the OD is often considered as a landmark which can be utilised for a coarse localisation of area of interest in retinal fundus images, reducing the search space during the pre-processing stage.

In this work, a dual-channel approach with a modified C-V model to segment the PPA and the OD individually was exploited. The seeded region growing proposed algorithm particularly aims to address the aforementioned challenges on how to maximise information extraction of features (OD/PPA) while keeping interference (blood vessels) to a minimum.

In the previous studies, investigators were required to manually measure the PPA region in either 2D images [10–16] or 3D images which were constructed by specially-written computer planimetry program [6]. Compared with the work that has been done by different groups, there are three main merits of the proposed MULIPT method: Firstly, the software tool could not only detect but also can quantify the size and transverse and conjugate diameter of OD region automatically, which is a technique not fully established by the other research groups. Secondly, the proposed software can automatically detect and quantify both the PPA region in

2D fundus images, which is a breakthrough in the field of computer-aided tool on retinal image applications. Based on the above two strong points, the ratio between the OD and PPA size could also be offered by the proposed tool. Such a tool could not only reduce the workload of the human assessor and therefore avoid problems resulting from fatigue, but also would be more cost-effective for population-based screening.

There remain some limitations within this MULIPT method: Firstly, the software occasionally stopped at undesired points upon encountering irregular dark pixels prior to the OD boundary. This results in underestimation of the actual size. Secondly, the proposed algorithm estimates the sizes of OD and PPA regions, providing a means to measure the extent of PPA. It will be ideal if the software could also define the absolute shapes allowing the patterns in PPA progression be studied in different eye conditions. One possible way to address the above limitations would be to take into consideration additional local information (e.g. texture) and exploit further the image fusion from multiple channels.

6.3   Chapter Summary

This chapter has demonstrated that PPA on a 2D retinal image can be quantified by means of computer-aided software. The proposed estimation model, MULIPT, after calibration achieved an accuracy of 94.0% (S.D.=5.88) and 93.8% (S.D.=5.26) in defining the size of OD and PPA respectively compared with the "gold standard" of an experienced human assessor. The model also showed high reliability in estimating the size, with correlation coefficient reaching 0.98 for both cases (OD and PPA). In terms of sensitivity, the model achieved 75.5% and 84.0% (tolerance, $\pm 10\%$) in size estimation of the OD and PPA region, and higher when the tolerance level was increased. The robustness of our calibration method was also investigated and it was found that our model consistently achieved a mean accuracy of more than 92.7%. Moreover, it could also provide ophthalmologists additional information, namely transverse and conjugate diameter of the OD as well as the ratio between the OD and PPA size, with potential application in eye screening programs. The methods developed so far are therefore promising as the basis for a fully-automated pre-screening technique that will prioritise images for subsequent expert human assessment.

Chapter 7
Optic Disc (OD) and Parapillary Atrophy (PPA) Analysis: Multiple image processing and Edge Detection Techniques

In Chapter 5 and Chapter 6, two different approaches were introduced to the segmentation of the Optic Disc (OD) and Parapillary Atrophy (PPA). In Chapter 6, the experimental trials were reasonable in defining the sizes of both the OD and PPA region, but did not perform well enough in terms of defining the actual shape of these two regions. Therefore, a novel imaging tool, Parapapillary atrophy AND Optic disc Regions Assessment (**PANDORA**), for assessment of both the OD and PPA is introduced in detail in this chapter. The tool is implemented by a combination of image processing techniques such as edge detection, ellipse fitting methods, modified Chan-Vese approach, thresholding, scanning filter and multi-seed region growing methods. In addition, clinical-knowledge has been utilised to develop this tool. The results show PANDORA can describe the actual shape of the regions and is more robust against difficult conditions.

7.1   Background Study: Direct Least Square Fitting algorithm

Ellipse fitting is traditionally categorised into two types of techniques: least squares fitting and clustering (such as Hough-based approaches [122, 123]). The former techniques focus on the parameters setting that minimise a certain distance measure between the ellipse and the spatial data points. Fitzgibbon *et al.* [124] proposed an efficient least squares approach for directly fitting ellipses to scattered data. A general conic fitting could be represented by an implicit 2nd-order polynomial:

$$F(a, x) = a \cdot x = ax^2 + bxy + cy^2 + dx + ey + f = 0 \qquad (7.1)$$

where a=[a b c d e f]^T and x=[x^2 xy y^2 x y 1]^T. *F(a; x_i)* denotes the algebraic distance of a point *(x,y)* to the conic *F(a; x)* =0. By minimising the sum of squared algebraic distances of the curve to the *N* data points x_i, the fitting of a general conic is probably to be achieved [125].

$$D_A(a) = \sum_{i=1}^{N} F(x_i)^2 \qquad (7.2)$$

It is widely known that to compel the conic's representation to be an ellipse the discriminant of the parameter vector *a* of equation (7.2), *b^2-4ac*, must be negative. However, this assumption does not guarantee to provide an optimal solution. Here, a, b and c are coefficients of equation (7.1). In the study, Fitzgibbon *et al.* tried to arbitrarily scale the parameters and eventually imposed the equality constraint 4ac - b^2 = 1, which minimised the sum of squared algebraic distances from all points to the ellipse. Their results describe the advantages of the ellipse-specificity in terms of occlusion and the sensitivity of the noise. The approach is easy to implement, extremely robust and efficient, and ellipse-specific therefore even when the algorithm encounters bad data it will always yield an ellipse. As a result, PANDORA has adopted this method to produce an estimate of the elliptical shape of OD region.

7.2 Segmentation and Quantification Tool for the OD and PPA region

7.2.1 Proposed Method

The imaging tool called PANDORA is implemented in MATLAB (Mathworks Inc., Natick, MA, USA). All fundus images were first cropped manually to the Region of Interest (ROI) and had a "ground truth" estimate of the OD and PPA regions defined by an ophthalmologist who had not seen the results from PANDORA. The experimental protocol are described in detail in Figure 1.4, Chapter 1. 7.1 illustrates the flow chart of the PANDORA algorithm, which can be divided into three phases:

Phase 1: OD segmentation
This module uses an ellipse fitting technique on a (Sobel) edge map in the red channel to outline the OD boundary.
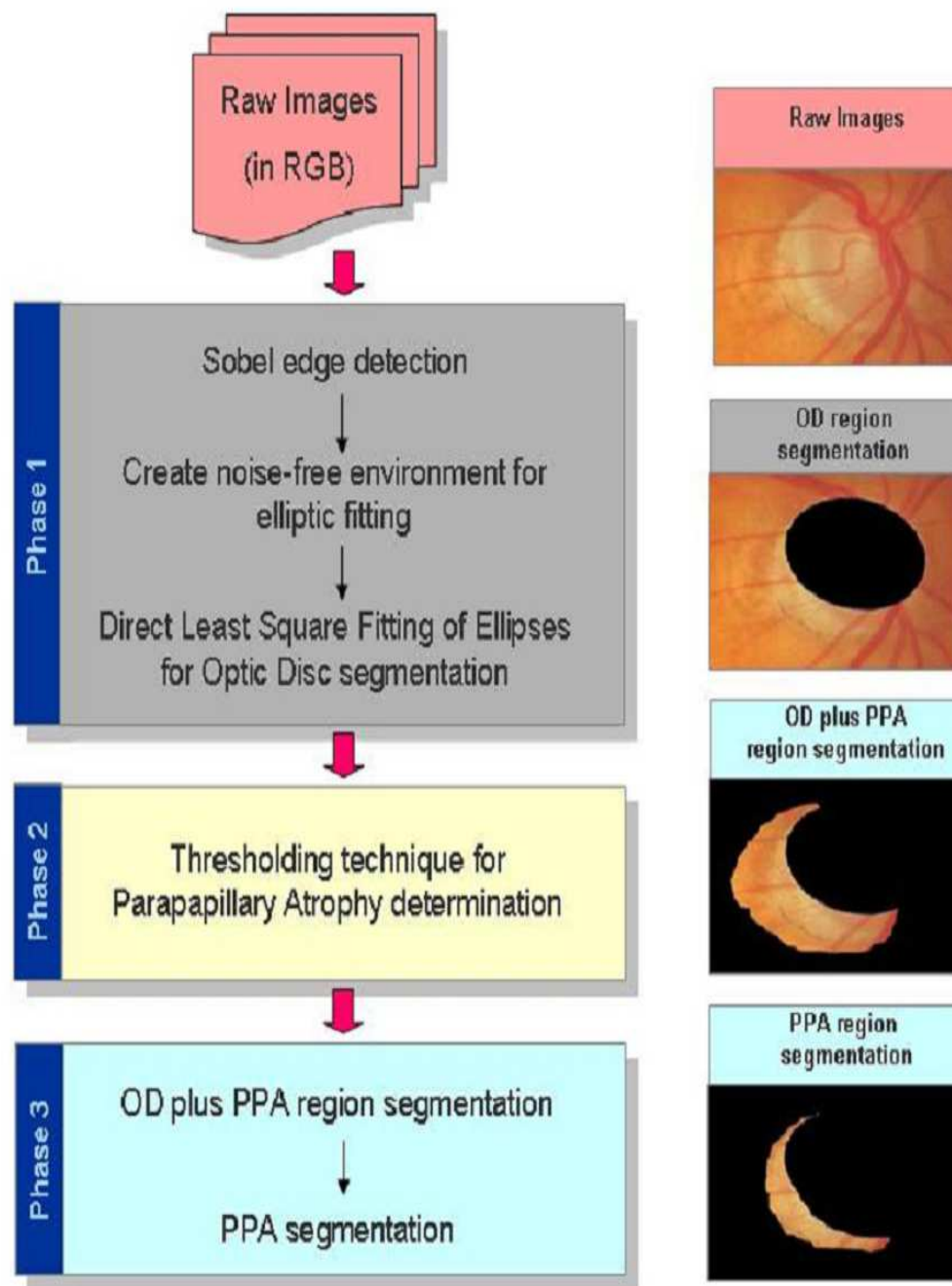
Figure 7.1: *A flow chart for segmentation of the OD and PPA. The scheme consists of three main phases: OD segmentation (gray), PPA detection (pale yellow) and PPA segmentation (cyan).*

A. Sobel edge detection

A Sobel edge detection operator is applied to the red channel of the cropped image, generating an edge map.

B. Create noise-free environment for elliptic fitting

The OD is planned to be extracted using a Direct Least Square Fitting algorithm of an Ellipse (DLSFE) [124]. This algorithm yields an elliptical solution that minimises the sum of squared algebraic distances from the image edge points to the fitted ellipse. However, this ellipse fitting technique is susceptible to noise and requires pre-processing to remove unwanted pixels from the fundus image before fitting. Therefore, a two-stage pre-processing technique is used to eliminate noise: the first stage locates and extracts retinal vessels in the Hue channel of the image; the second stage utilises a clustering technique with the nearest neighbour rule [126] to isolate the OD (and the PPA) from the background.

C. Direct Least Square Fitting of Ellipses for Optic Disc segmentation

Upon completion (A & B), a DLSFE is fitted to estimate the OD boundary. To reduce fitting errors, the proposed method fit the OD region iteratively until the centre of fitting result is within a pre-determined "tolerance" distance from the centre of cropped image (ROI).

Phase 2: PPA detection

With the OD removed, the PPA detection module then determines the presence of PPA in the temporal zone using prior knowledge about the nature of PPA. Note that the temporal zone is one of the four zones in the fundus image (see Figure 7.2), in which PPA normally first develops.

A. Thresholding technique for Parapillary Atrophy determination

The thresholding technique is applied to detect the brighter pixels in temporal zone of the image (See Figure 7.2) in the blue channel where the PPA appears most clearly. That is because the OD is clinically divided into four zones: Temporal, Superior, Nasal and Inferior. Figure 7.2, 7.3a and 7.3f give examples of a right-eye image and a left-eye image, respectively. Figure 7.3b and 7.3g give examples of original fundus images in blue channel.
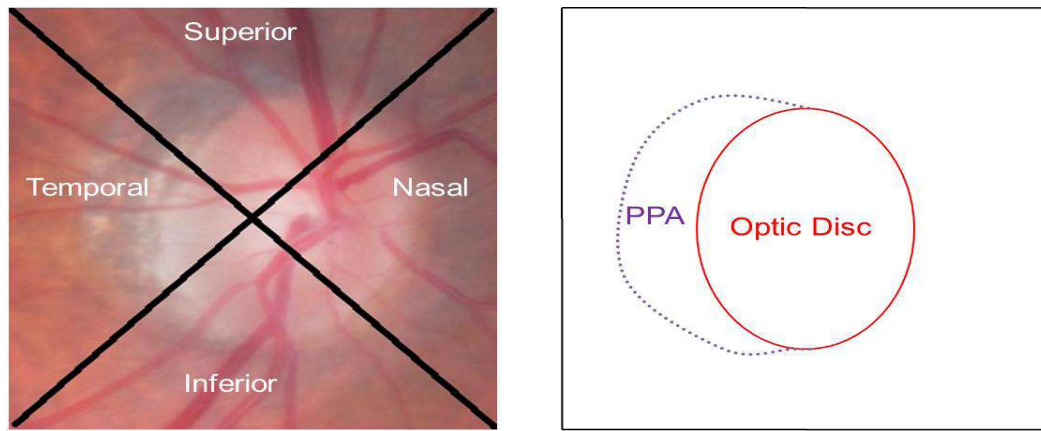
Figure 7.2: *(a) Original colour retinal fundus image of a right eye. Annotations describe the four different zones of a retina; (b) the OD boundary and the PPA region.*

The temporal and nasal zones must be exchanged if the image is of a left-eye. As aforementioned, the OD and PPA account for the brighter region of the image (around top 12%). If the OD region (estimated from Phase 1) is removed, PPA can be detected by the presence of bright pixels in the temporal zone (Figure 7.3c and 7.3h). Therefore, PANDORA has been designed with the capability to produce a mask to black out the nasal,inferior and superior area (Figure 7.3d and 7.3i). Finally, Figure 7.3e and 7.3j give the detection result as image with/without PPA, respectively.

Phase 3: PPA Segmentation

Once detected, the PPA region is then segmented using a combination of image processing techniques: thresholding, a scanning filter and multi-seed region growing methods [120].

In this phase, an automated scheme [120] mentioned in detail in Chapter 6 for the extraction and quantification of the PPA region was adopted.

A. OD plus PPA region segmentation

The scheme used an initial segmentation and estimation of the OD-plus-PPA boundary based upon a Modified Chan-Vase analysis [121] of the blue channel. The OD region is then removed from the OD- plus-PPA using the result obtained from Phase 1, leaving the first order estimation of the PPA region.

B. PPA segmentation

A multi-seed region growing method is subsequently used to refine the actual PPA boundary [120].

95
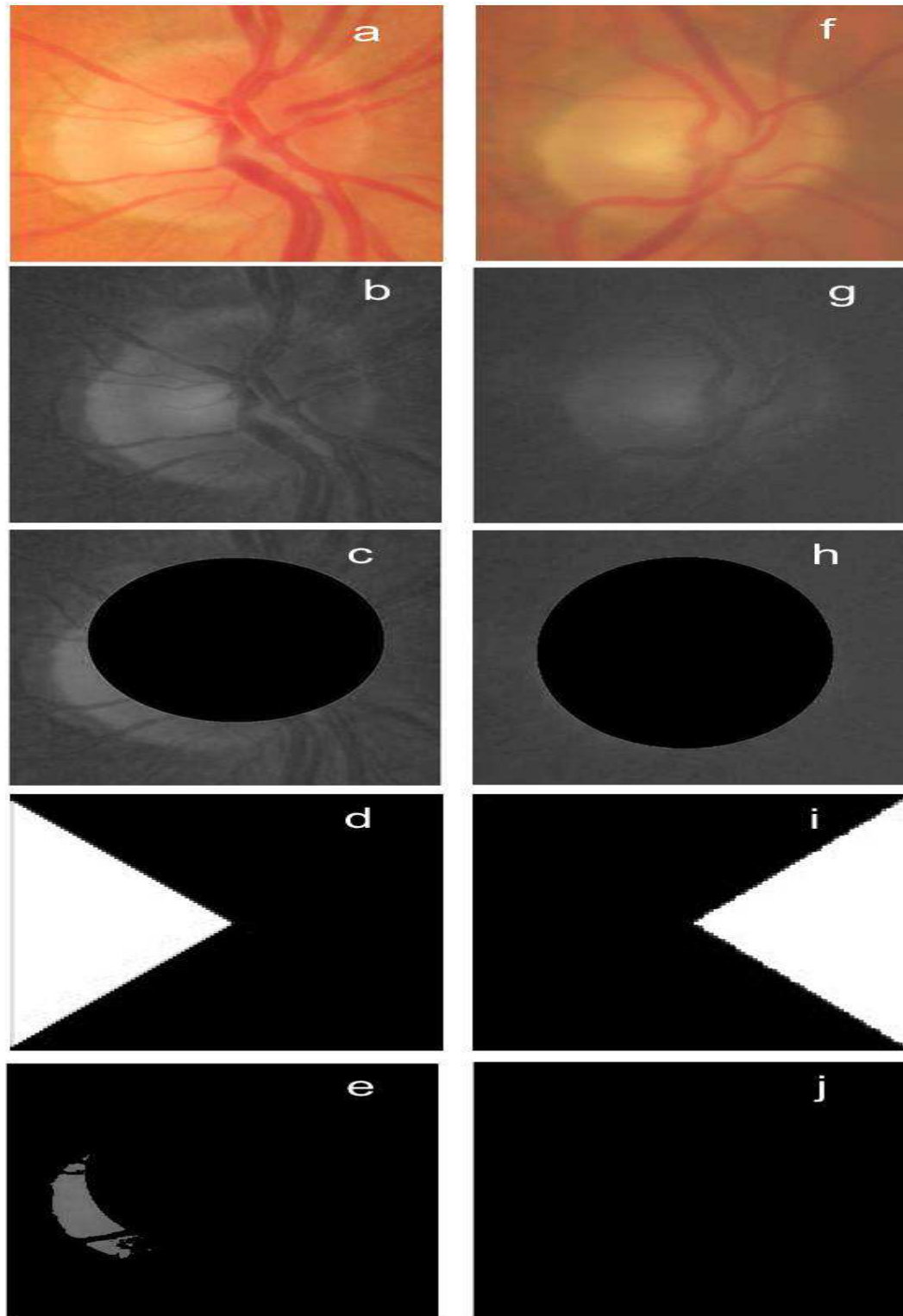
Figure 7.3: *Process of PPA detection: (a) and (f) Examples of an original fundus right-eye image and an original fundus left-eye image, respectively. (b) and (g) Examples of original fundus images in blue channel (c) and (h) OD segmentation results from Phase 1 (d) Left mask (i) Right mask (e) and (j) shown the detection result as image with/without PPA, respectively.*

PANDORA combines these techniques and exploits both global and local information for PPA and OD segmentation. The results permit the OD and PPA to be assessed to derive three physiological parameters (all in pixels):

(a) The size of the Optic Disc

(b) The length of minor/major Optic Disc axis

(c) The size of the PPA

The segmentation results also reveal the shape of PPA which may be of importance in understanding the development process of PPA.

7.2.2   Experimental Results

A total of 133 colour fundus images (including 31 poor quality images as determined by an ophthalmologist, Augustinus Laude) from 101 subjects were randomly selected from the LBC database. The human assessor observed the scleral ring on the images to identify the limits and size of the OD. Thereafter, the human assessor identified the region of PPA by the observation of brightness and texture. Without knowing the results from PANDORA, the human assessor identified images with PPA (82 images with PPA; 51 images without PPA) and provided a "ground truth" estimate of the OD and PPA region in each image. The assessor first observed in full colour space (RGB) the scleral ring and the retinal vessel bending to identify the boundary of the OD. Subsequently, the region of PPA was identified according to the brightness and texture of image pixels. PANDORA does not divide the PPA region into different zones but views them as one. A random subsample of 30 images with PPA and 20 images without PPA was drawn to evaluate PANDORA The area enclosed by the ground estimate/the segmentation result from PANDORA is counted pixel by pixel with the Matlab software development tool to quantify the size of each region. PANDORA achieved a PPA detection rate of 89.47%. Figure 7.4 and 7.5 show six samples from the OD segmentation results of fundus images without and with PPA respectively.

The first column gives examples of the best results achieved while the second column shows the worst. The ground estimate is enclosed by black spots and the OD segmentation result by a blue solid line.

Figure 7.6 shows six samples of the PPA segmentation results from PANDORA. The segmentation result is enclosed by red triangles and the ground truth estimate by a solid black line. The
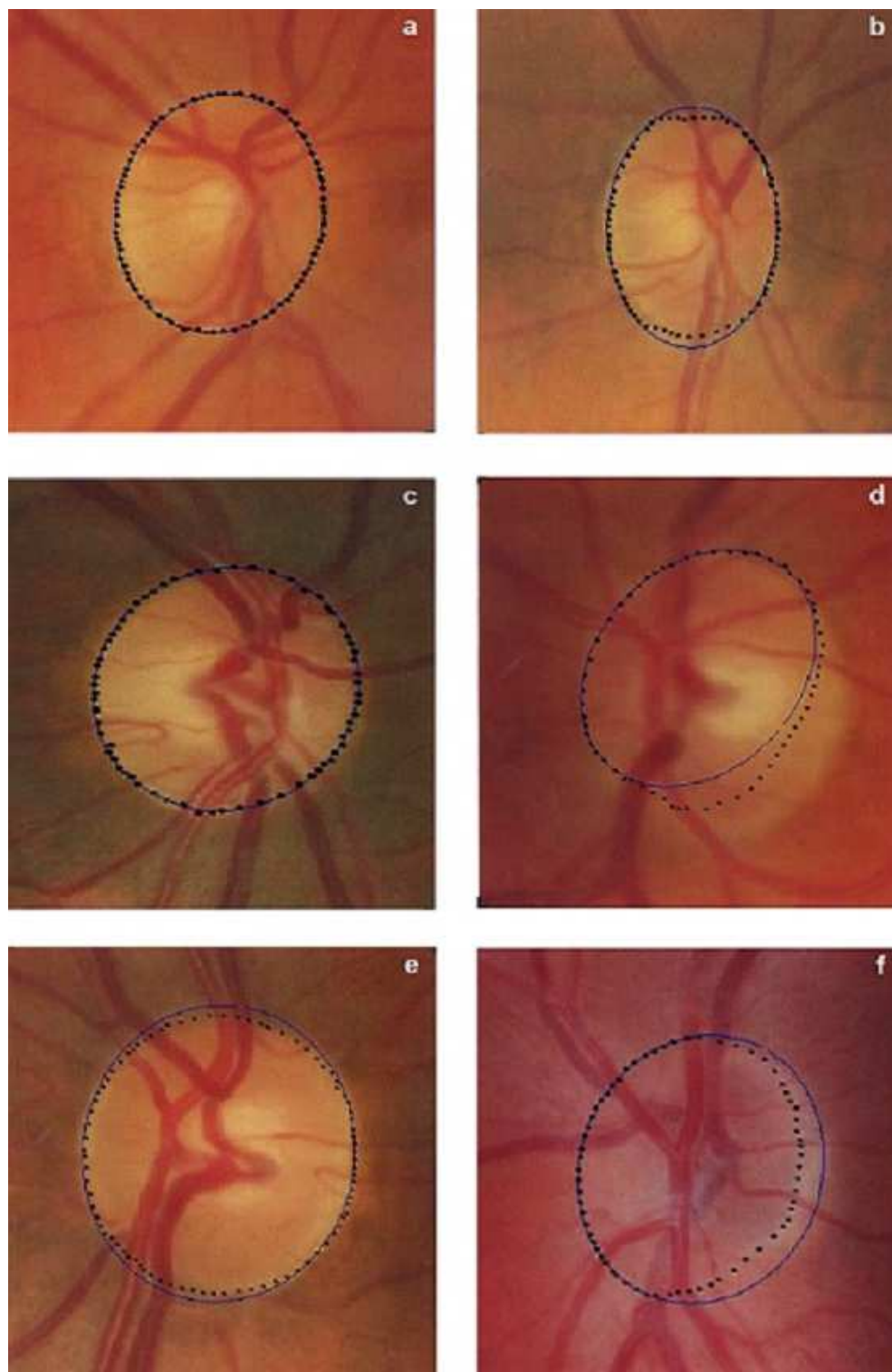
Figure 7.4: *Segmentation results on the images without PPA from PANDORA. Images on the left column (a), (c), (e) represents the best results; Images on the right column (b), (d), (f) represents the worst results. The ground truth estimate is drawn on the black spots while the estimated OD region is outlined by the blue solid line, respectively.*
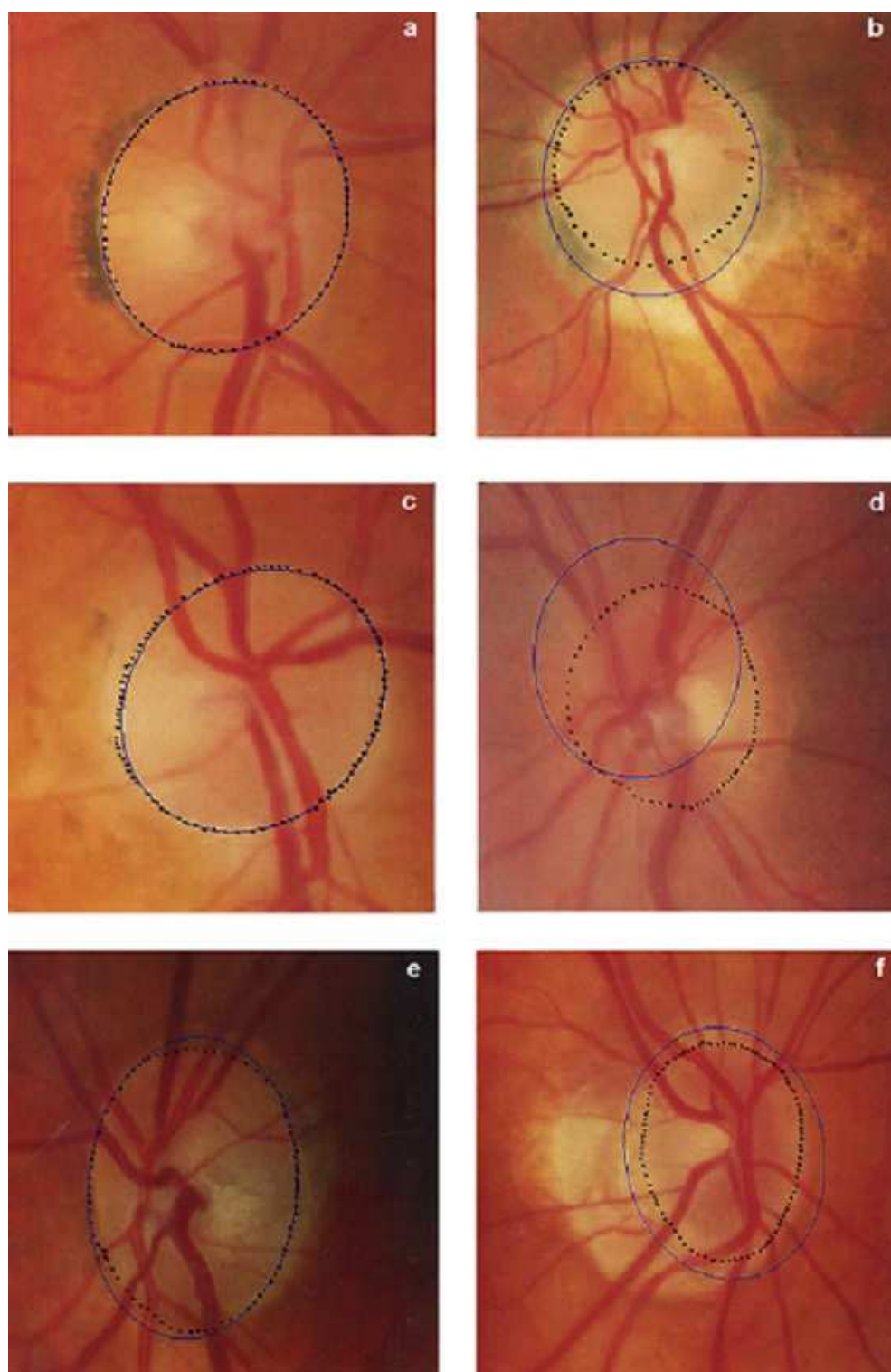
Figure 7.5: *Segmentation results on the images with PPA from PANDORA. Images on the left column (a), (c), (e) represents the best results; Images on the right column (b), (d), (f) represents the worst results. The ground truth estimate is drawn on the black spots while the estimated OD region is outlined by the blue solid line, respectively.*
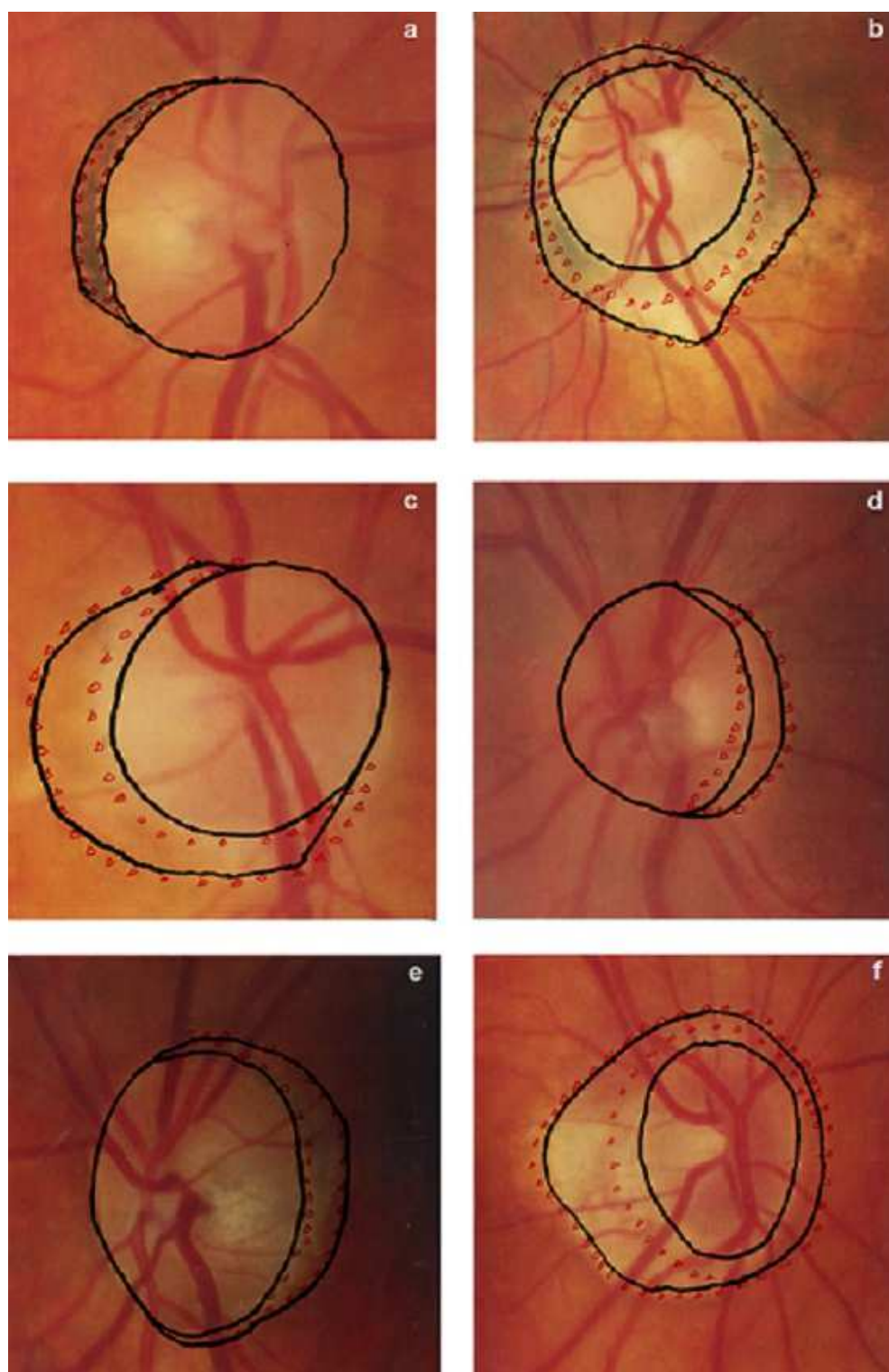
Figure 7.6: *PPA segmentation results on the images from PANDORA. Images on the left column (a), (c), (e) represents the best results; Images on the right column (b), (d), (f) represent the worst results. The ground truth estimate is enclosed by the black solid line while the estimated PPA region is enclosed by the red triangle, respectively.*

results indicate that PANDORA is able to detect and capture the boundary separating the OD and PPA regions reasonably well despite its poorly-defined nature. Apart from the variation in the colour, size and shape of the OD and PPA, there are additional factors to take into account (shown in figure 7.4 and 7.5). The OD boundary and the blood vessels do not always have a sharp contrast, making it difficult to remove all the background noise completely before fitting an ellipse. The presence of PPA further complicates this process (see figure 7.5b, d, f).

The examples given in the second column (b, f) of Figure 7.5 show over-estimates of the OD region. This, in effect, reduces the possible PPA area (shown in Figure 7.6b, f). Conversely, under-estimation of the OD region could also lead to inaccurate segmentation of the PPA region, as shown in Figure 7.6c-e. Therefore, the use of multi-seed region growing method in Phase 3 to refine PPA boundary is necessary to eliminate any contribution from the OD (refer to Figure 7.6c).

7.2.3 Validity of the Proposed Method

There are two main functions of PANDORA: to determine the presence of PPA, and to quantify the area of PPA and OD. Two different validation methods were therefore adopted. Firstly, we calculated the mean accuracy of PANDORA's PPA detection as well its *Specificity* and *Sensitivity*. The Specificity, defined as the number of true negatives divided by the sum of false positives and true negatives indicates how well a tool can correctly identify negatives. The Sensitivity, defined as the number of true positives divided by the sum of false negatives and true positives indicates how well a tool can identify actual positives. Based on the PPA detection results, PANDORA is able to achieve a sensitivity and specificity of 0.83 and 1, respectively. Secondly, in terms of area estimation, the accuracy is measured by comparing the segmentation results against the ophthalmologist's ground truth estimate of OD/PPA region. PANDORA is assessed by a simple yet effective measure (M) of the matching between two estimates, which is defined as:

$$M = \frac{N(R \bigcap T)}{N(R \bigcup T)} \tag{7.3}$$

here R and T represent the segmentation result and the ground estimate respectively and N(.) denotes the number of pixels within the targeted region. Table 8.1 summarises the segmentation

results on 50 images.

	Images with PPA		Images with no PPA	
Results	PPA	OD	PPA	OD
Mean accuracy (%)	73.57	81.31	-	95.32
Standard Deviation	11.62	10.45	-	4.36

Table 7.1: *The Statistical Results of PPA and OD Segmentation in 50 Trials*

7.2.4 Discussions

This chapter has introduced PANDORA, a novel automated retinal imaging tool for both detecting the presence of PPA and quantifying OD and PPA using 2D colour fundus images. Experimental results showed that PANDORA achieves a high PPA detection rate (89.47%) despite the wide variation in fundus image quality. These results are in comparable with those reported in [59] in which the detection rate is 87.5%, sensitivity 0.85 and specificity 0.9 of the database (40 images with PPA; 40 images without PPA) from Singapore Eye Research Institute (SERI).
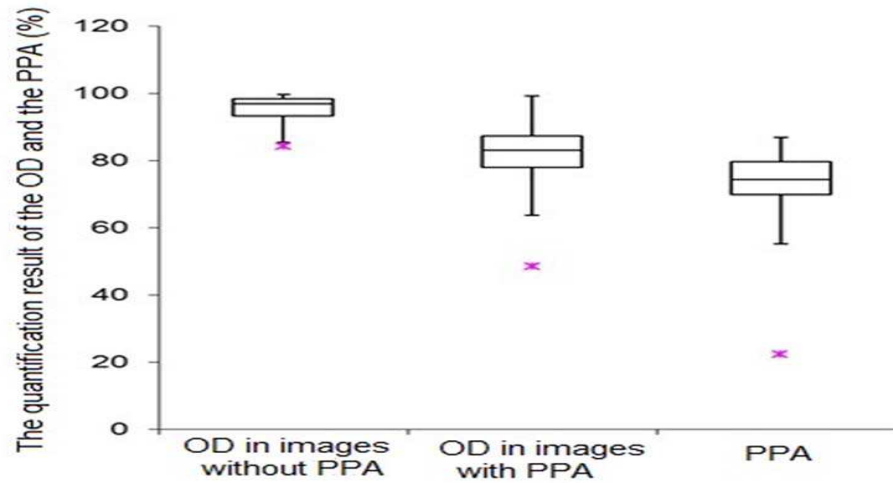
Figure 7.7: *Box plots for the quantification result of the OD and the PPA on the images with the PPA or without the PPA. The Lower Outliers are denoted as red star. The bars specify the ranges of quantification results, and the boxes specify the first and third quartiles with the median represented by the centre lines.*

Figure 7.7 shows the segmentation results of the OD and PPA regions for images with and without PPA. As expected, the results indicate that PANDORA segments the OD better in im-

ages without PPA than in those with PPA, as the OD is the sole bright object. The OD region may be over-/under-estimated when there is no clear boundary, as is often the case in images with PPA. That is, β-zone PPA sometimes appears brighter than the OD region or of similar brightness to the OD. On the other hand, α-zone PPA appears a little bit "dark" or "gray" compared with the OD region. As a result, the OD region may be over-/under-estimated when there is no clear boundary, as is often the case in images with PPA.

PANDORA has four primary advantages over alternative approaches. Firstly, it both detects the presence of PPA and allows quantification of PPA region automatically from 2D colour fundus images alone. Previous studies [7, 59] were limited to the detection of PPA. The size of the PPA region was quantified manually [6, 10]. PANDORA is therefore the first automated tool to detect the presence of PPA and quantify the size of PPA region (including both zones of PPA). It is also envisaged that PANDORA could help clinicians to track the development of PPA if fundus images of a patient were recorded over a period of time. Secondly, PANDORA improves the tool [119, 120] proposed in previous chapters by using an OD segmentation approach based on an edge map, which estimates the OD/PPA boundary more accurately. Therefore it can describe the actual shape of the regions, allowing more detailed study of the relationship between PPA and different ocular diseases. The previous approach, which was based on the 'snake' algorithm, suffered from a random offset in defining the boundary and could only give an estimate of the size. Thirdly, PANDORA has been fully automated, reducing the dependency on a human assessor and minimising problems related to human errors such as habituation. PANDORA's physiological measurements offer additional information for clinicians studying ophthalmic or systemic diseases. Fourthly, PANDORA is intrinsically more appropriate for large-scale screening programs owing to utilization of the OD and PPA borders on the 2D fundus image as an alternative to expensive OCT equipment. Digital fundus cameras [16] acquire fundus images quickly, without the time-consuming procedures of the OCT machine. These cameras are relatively cheap and have become a standard examination tool in ophthalmology clinics. Therefore, working on 2D fundus images is both a cost- and time- effective way and more convenient to the users, compared with OCT instruments.

There remain three limitations within this method: Firstly, PANDORA is susceptive to noise due to an ill-defined boundary, from overlapping blood vessels and from lighting artefacts. Creating a noise-free edge map for ellipse fitting is essential, to avoid under-/over-estimation of the

actual region. In this chapter, a naive thresholding technique to extract retinal blood vessels from the fundus images was used. Techniques such as artificial neural networks [127–129] will be explored in future development to improve the robustness in retinal vessel segmentation. Secondly, the proposed tool utilises only the brightness of the pixels to detect the presence of PPA. Adding texture information, for instance, should improve the detection rate. Thirdly, the OD is not always perfectly elliptical, despite its general appearance. The assumption made in this work (i.e. OD is always elliptical or circular [121]) helps to estimate the boundary of the OD, especially when it is poorly defined (i.e. appears as broken lines in the edge map). Admittedly, this assumption could also limit the fit to the real OD size and shape (e.g. Figure 7.4d). While more complex segmentation algorithms might be able to describe a non-elliptical shape better, it will remain difficult to estimate a poorly defined boundary. As such, we argue that the principle of Occam's razor may be best applied.

7.3 Chapter Summary

PPA has been linked to degenerative myopia and glaucoma, both of which can lead to loss of sight. Early detection and quantification offer an opportunity for medical intervention to halt/slow the development of ophthalmic diseases. However, existing methods are manual and subjective. They also require multi-modal imaging systems (i.e. 2D standard laser ophthalmoscope plus optical coherence tomography) which are not widely available. In this chapter, a tool that can detect PPA and quantify its size automatically using 2D colour fundus images alone was demonstrated. The presence of PPA is detected with an accuracy of 89.47% in 133 images. The sensitivity and specificity of PPA detection are 0.83 and 1 respectively. The proposed tool also achieved an accuracy of 81.31% (S.D.=10.45) and 95.32% (S.D.=4.36) in estimating the OD region in images with and without PPA. The accuracy of PPA segmentation is 73.57% (S.D.=11.62), compared with the "gold standard" defined by an experienced ophthalmologist. Conventionally, the size of the PPA region is quantified manually [6, 10]. PANDORA therefore provides the first automated tool to detect the presence of PPA and further to quantify the size of PPA region, including α-and β-zone of PPA, which allows clinicians to track PPA progression if PANDORA is performed on the images of a specific patient taken at different times. Further development of PANDORA (e.g. segregating the PPA region into alpha- and beta-zone) will allow a wider study of the development of PPA and its significance in disease diagnosis.

Chapter 8
Summary and Conclusions

In this chapter, a summary of the achievement of this thesis is first presented. Subsequently, some limitations of the work and conclusions are drawn by revisiting the original objective of this thesis. The chapter ends with a list of possibilities for future work.

8.1 Summary

Figure 8.1 shows the research progress in this thesis, starting with literature reviews both in medical and in image processing (Chapter 1,2) and next some preparatory works (Chapter 3, 4) and then three different novel techniques applied on the segmentation and quantification of the OD and PPA (Chapter 5,6,7) and finally a summary of the work (Chapter 8).

Firstly, the literature review showed there was a growing technological trend where more computer-aided tools for retinal image analysis were being developed as important screening tools for early detection of ophthalmic diseases. These were developed by many image processing techniques. These systems must be developed on clinical knowledge for the sake of getting reasonable results. The method for PPA detection and evaluation methods for the segmentation of biomedical objects have been reviewed and the approaches for the OD detection and segmentation were listed.

Before the development of the proposed approaches as an effective imaging tool for early diagnosis, the background knowledge, both of image pre-processing and segmentation techniques, needed to be fostered.

This thesis has three main hybrid approaches, namely "Colour Morphology technique with Chan-Vese Snake," and "A Combination of techniques and Modified Chan-Vese Snake," and "Modified Chan-Vese and Edge detection techniques," for the segmentation of the OD and PPA.
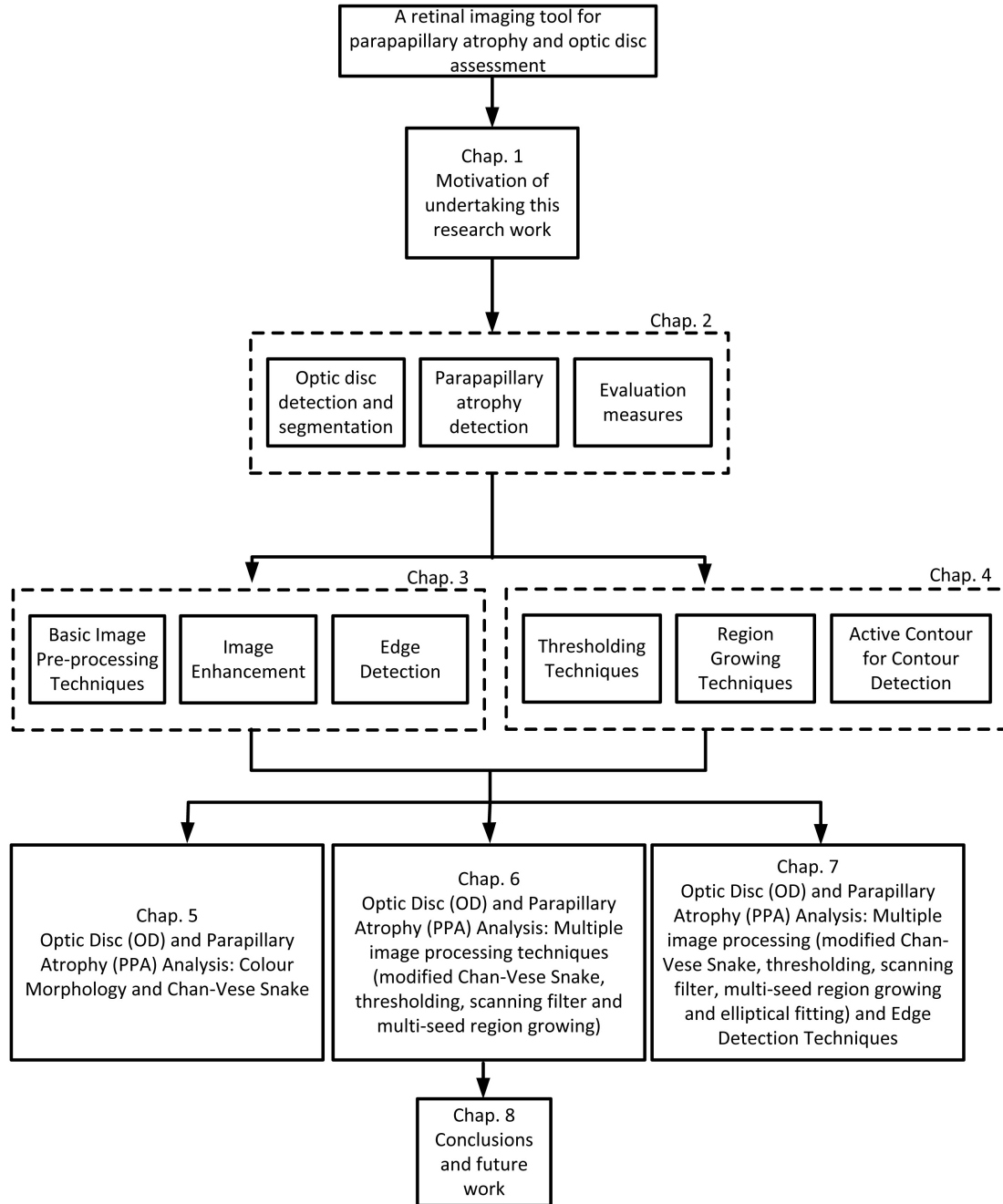
Figure 8.1: *Flowchart illustrating the research progress in this PhD thesis.*

On the approach of colour morphology technique with Chan-Vese Snake

In chapter 5, a novel technique, MOCV, to estimate the OD and PPA automatically is introduced. The introduced methodology exploits both the red and blue channels of the image to maximise the information on features (PPA) whilst keeping interference (blood vessels) to a minimum. A technique named "snake without edges"(Chan-Vese Snake) is used to estimate the contour of the OD and PPA. The proposed approach is evaluated against the reference boundary drawn by an ophthalmologist. Experimental results on 20 images show that the method can repeatedly detect the boundary automatically and the mean accuracy is as high as 86.65% (S.D.=8.97) which represents a major improvement from the results reported in the literature.

On the approach of a combination of techniques and modified Chan-Vese Snake

A computer-aided measuring tool, named 'MULIPT', to automatically detect and quantify both the PPA and the OD regions in 2D images of the retina is described in chapter 6. The OD region is segmented using a Chan-Vese model with a shape restraint. This region is then removed from the image (OD+PPA) which has been cropped by a modified Chan-Vese approach, producing a first order estimation of the PPA region. Its boundary is subsequently refined by using thresholding, scanning filter and multi-seed region growing methods. Dual channels (blue and red) in the Red-Green-Blue space are utilised to minimise the interference effects of blood vessels and artifacts. The proposed software was tested on 94 randomly selected images with PPA from 66 subjects of a well-characterised cohort database. The proposed algorithm achieved a mean accuracy level of 94.0% (S.D.=5.88) and 93.8% (S.D.=5.26) in estimating the "SIZE" of the PPA and OD respectively, compared with the ground estimate defined by an ophthalmologist. In terms of correlation between the data of ground estimate and our estimation, a correlation coefficient of 0.98 for both the PPA and the OD was obtained. The tool proposed in this chapter could also provide additional information, namely transverse and conjugate diameter of OD, which may be useful for eye screening purpose.

On the approach of modified Chan-Vese Snake and edge detection techniques

Chapter 7 describes a computer-aided measuring tool, named 'PANDORA', for automated detection and quantification of both the PPA and the OD regions in 2D retinal fundus images.

The OD region is segmented using a combination of edge detection and ellipse fitting methods. The PPA region is identified by the presence of bright pixels in the temporal zone of the OD, and segmented using a sequence of techniques, including a modified Chan-Vese approach, thresholding, scanning filter and multi-seed region growing methods. This tool has been tested with 133 colour retinal images (82 with PPA; 51 without PPA) drawn randomly from the LBC database, together with a "ground truth" estimate from an ophthalmologist. The PPA detection rate is 89.47% with a sensitivity and specificity of 0.83 and 1, respectively. The accuracy in defining the OD region is 81.31% (S.D.=10.45) when PPA is present, and 95.32% (S.D.=4.36) when PPA is absent, and the accuracy in defining PPA region is 73.57% (S.D.=11.62). PANDORA differs from the tool described in Chapter 6 as it could estimate the OD/PPA boundary better and hence describe the actual shape of the regions, allowing more detailed study about the relationship of PPA with different ocular diseases. The tool proposed in Chapter 6 suffered from random offset in defining boundary and could only give an estimate of the size. PANDORA demonstrated for the first time how to quantify the actual shape of OD and PPA regions using 2D fundus images, enabling ophthalmologists to study ocular diseases related to PPA using a standard fundus camera.

In addition, the PANDORA, the mean accuracy of OD segmentation in images with/without PPA of the proposed method in 50 trials are 81.31(S.D.=10.45) and 95.32% (S.D.=4.36) respectively, which are comparable to the best state-of-the-art performacne as listed in Table **??**. It should be mentioned that Gradient Vector Flow (GVF) Snake and the method proposed in Chapter 6 have a much lower OD segmentation accuracy in the images with PPA (e.g., 48.65% and 68.35% respectively) because they face a convergence problem whenever the boundary of a region is not celar (in this case, PPA region).

	Images with PPA		Images without PPA	
Methods	M.A.(%)	S.D.	M.A. (%)	S.D.
GVF Sanke	48.65	11.23	91.31	5.23
MULIPT	68.35	10.42	93.27	5.47
PANDORA	81.31	10.45	95.32	4.36

Table 8.1: *Comparison of the OD segmentation methods in 50 Trials*

Based on the aforementioned detection and segmentation results, some conclusions can be drawn and are described in the following section.

8.2 Conclusions

The thesis examined the suggestion that

An automated optic nerve features detection and segmentation system based upon a combination of image processing techniques to emulate a human expert could approach the performance of the human visual system.

After an investigation, it was found that the software tool, which is implemented by a combination of image processing techniques, can detect the presence of PPA and can make that measurement of the OD and PPA region without human intervention in a 2D fundus image. In addition, the tool not only detected the OD region, estimated its size and actual shape of its regions, it also provided readings of the transverse and conjugate diameter- two commonly used parameters in retinal image analysis. Moreover, using the software, the normalised PPA size (i.e., the ratio between the PPA and the OD size) could be derived and could explore its association with different eye diseases or conditions and establish a better understanding about the significance of the PPA development. Finally, the tool could not only reduce the dependence on the human assessor and thus potentially avoid problems associated with human errors such as habituation, it could also be more cost effective for larger scale population-based screening.

There remain some limitations within the proposed tools, however:

Firstly, the problem of underestimation of the actual size. That is because one of the software methods, which is developed by snakes relative techniques, stopped at undesired points on encountering irregular dark pixels before the OD boundary in good-quality images and less consistently in poor-quality images.

Secondly, the proposed model is susceptive to noise due to an ill-defined boundary, from overlapping blood vessels and from lighting artefacts.

Thirdly, the proposed method utilises only the brightness of the pixels to detect the presence of PPA. Adding texture information for instance should improve the detection rate.

Fourthly, due to the limitation of getting ground estimates from the medical partner, the databases used to test the proposed software tools are smaller than desired. The potential of any future application would depend on testing with enough data to ensure statistical significance.

Finally, the OD is not always perfectly elliptical, despite its general appearance. The assumption made in this work (i.e. the OD is always circular or elliptical) helps to estimate the boundary of the OD, especially when it is poorly defined (i.e. appears as broken lines in the edge map). Admittedly, this assumption could also limit the fit to the real OD size and shape.

8.3   Practical Usage of PANDORA

In common with many classification systems, PANDORA carries a risk of false negatives in identification of the OD and PPA. In its current form, PANDORA is best used as a pre-processing ("set up") tool for human classification. If (1) to (3) below can cause the false negative rate to drop, it would be possible to use PANDORA as an autonomous classifier.

1) Apply image fusion technologies to this application to get more accurate results.

2) Validate the tool by introducing some false positive images within a bigger database.

3) Use previous records. False positives can be reduced if new examinations are compared with older ones from a previous examination. Even in the best test, false positive results are a risk.

Ultimately, a decision must be made as to what is an acceptable rate of false positives.

8.4   Future Work

Future developments of the system include improving the accuracy of PPA detection, both the OD and PPA segmentation and differentiation between different types of PPA. It would also be ideal if the software could describe a non-elliptical shape better and could address the above limitations. More complex segmentation algorithms would need to take into consideration additional local information (e.g., texture) and explore further the image fusion from multiple channels. Creating more noise-free edge maps for ellipse fitting would be another task, in order to avoid under-/over-estimation of the actual region detected by an edge detection based software tool. Moreover, development of the system segregating the PPA region into α- and β-zone would be essential. There is a plan to evaluate different types of PPA on a bigger database in the near future and also to study its significance in disease diagnosis. The systems are also still promising as the higher quality images are available to present day medics because the higher quality images the systems could get, the better results the systems could have. Compared with expensive retinal imaging equipment (e.g. OCT), the fundus cameras are affordable to optome-

try centre. The developed systems could therefore be promoted as an important part of periodic optometric examinations which is a routine preventive health care.

Appendix A
Publications

Journal papers

• Cheng-Kai Lu, Tong Boon Tang, Augustinus Laude, Baljean Dhillon,Alan F. Murray,
" Noise reduction method for fitting Elliptical object on medical images," *IET Electronics Letters*
(In preparation) (IF = 0.965, Rank: 131/244, 53.68%)

• Cheng-Kai Lu, Tong Boon Tang, Augustinus Laude, Baljean Dhillon,Alan F. Murray,
"PANDORA: A Retinal Imaging Tool for Assessment of the Optic Disc and Parapapillary
Atrophy," *Journal of biomedical optics* (Accepted) (IF = 3.157, Rank: 7/71, Top 9.85%)

• Cheng-Kai Lu, Tong Boon Tang, Augustinus Laude, Ian J. Deary, Baljean Dhillon, Alan F.
Murray,"Quantification of Parapapillary Atrophy and Optic Disc," *Investigative Ophthalmology
and Visual Science* ,vol. 52, 4671-4677, June 2011. (IF = 3.466, Rank : 5/56, Top 8.92%)

Refereed Conference Paper

• Cheng-Kai Lu, Tong Boon Tang, Augustinus Laude, Baljean Dhillon, Alan F. Murray,
"Automatic Parapapillary Atrophy Shape Detection and Quantification in Colour Fundus
Images," in 2010 *IEEE Biomedical Circuits and Systems Conference (BIOCAS)*, 3-5th
November, Paphos, Cyprus, PP.86-89.

Book Chapter

• Cheng-Kai Lu, Tong Boon Tang, Augustinus Laude, Ian J. Deary, Baljean Dhillon, Alan F.
Murray, " Computer-Aided Assessment of Optic Nerve, " *in MULTI-MODALITY STATE-OF-
THE-ART: HUMAN EYE IMAGING AND MODELING* (In printing)

Abstracts

• A. Laude, C.-K. Lu, T.B. Tang, A.F. Murray, R.D. Henderson, I.J. Deary, B. Dhillon," Bound-
ary Detection of Optic Disc and Parapapillary Atrophy From Color Fundus Images Using Dual-
Channel Color Morphology and Snakes," *Association for Research in Vision and Ophthalmology
(ARVO). Abstract A549*, 2010. (It has been chosen as e-Poster.)

Quantification of Parapapillary Atrophy and Optic Disc

Cheng-Kai Lu,[1] Tong Boon Tang,[1] Augustinus Laude,[2,3] Ian J. Deary,[4] Baljean Dhillon,[2] and Alan F. Murray[1]

PURPOSE. A computer-aided measuring tool was devised to automatically detect and quantify both the parapapillary atrophy (PPA) and the optic disc (OD) regions in two-dimensional color fundus images of the retina.

METHODS. The OD region was segmented using the Chan-Vese model with a shape restraint. This region was then removed from the image (OD+PPA), which was cropped in a modified Chan-Vese approach, producing a first-order estimation of the PPA region. Its boundary is subsequently refined by using thresholding, a scanning filter, and multiseed region-growing methods. Dual channels (blue and red) in the red-green-blue space are used to minimize the interference effects of blood vessels and artifacts.

RESULTS. The software was tested on 94 randomly selected images of eyes with PPA from 66 subjects of a well-characterized cohort database. Our proposed algorithm achieved a mean accuracy level of 93.8% (SD 5.26) and 94.0% (SD 5.88) in estimating the size of the PPA and OD respectively, compared with the ground estimate defined by an ophthalmologist. In terms of correlation between the data of the ground estimate and our estimation, we obtained a correlation coefficient of 0.98 for both the PPA and the OD.

CONCLUSIONS. This software offers a means of quantifying the size of PPA on two-dimensional fundus images for the first time. The proposed algorithm is capable of detecting and quantifying PPA and OD regions repeatedly, with a mean accuracy of >93%, and could also provide additional information, such as the transverse and conjugate diameter of OD, which may be useful in eye-screening. (*Invest Ophthalmol Vis Sci.* 2011;52:4671–4677) DOI:10.1167/iovs.10-6572

Certain ophthalmic diseases (e.g., progressive glaucoma) and eye conditions (e.g., myopia) have been associated with the development of retinal pigment epithelium parapapillary atrophy (PPA).[1] Although thinning and degeneration in retinal tissue are generally irreversible, early detection and medical intervention may offer an opportunity to reduce or limit their progression.[2] More recently, there has been a growing interest in the potential role of PPA in detecting eye diseases at an early stage.[3–9]

Ophthalmoscopically, the PPA is divided into the β zone, located adjacent to the optic disc (OD) border and showing visible sclera as well as large choroidal vessels, and the α zone, located more peripherally and characterized by irregular hyper- and hypopigmentation. This classification of β- and α-PPA was first developed by Jonas et al.[10] and has now been accepted into common use, providing the motivation for studies to better understand the development of the PPA. For instance, Healey et al.[3] investigated the association between β-PPA and both environment and genes. They found that the presence of β-PPA appeared to be under strong genetic control, with only a fraction of this genetic effect shared with genes involved in myopia. Tezel et al.[4] studied the relationship between PPA and the OD in patients with glaucoma or visual field damage, by manually quantifying the size of the PPA and OD regions. The presence and the progression of PPA were found to be associated with subsequent OD or visual field changes in patients with ocular hypertension. Honrubia and Calonge[5] further found that, in patients with ocular hypertension, the presence of PPA could imply a risk of glaucomatous deterioration, as it has a significant association with the presence of defects in the retinal nerve fiber layer (RNFL). Xu et al.[6] investigated the association of PPA with glaucoma in a population-based study. They found that β-PPA appeared to be larger and occurred more frequently in glaucomatous eyes than in normal eyes of Chinese adults, but no significant difference was found between chronic open-angle and primary angle-closure glaucoma.[6]

Uhm et al.[7] used a commercial software package (Photoshop; Adobe Systems Inc., San Jose, CA) to measure the size of PPA and the OD regions in assessing how closely PPA is related to functional and structural glaucomatous optic nerve damage. They discovered that the severity of glaucomatous optic nerve damage and visual field defects were related to the increases in the size of PPA and concluded that PPA could be useful for the diagnosis and progression of glaucomatous nerve damage.[7]

There are ophthalmic techniques, such as retinal tomography (HRT; Heidelberg Engineering, Heidelberg, Germany) and optical coherence tomography (OCT), that can provide a colorless or pseudocolor 3-D visualization of the PPA and the OD.[11] They require a trained technician or ophthalmologist to manually identify the OD boundary on the image before the PPA and OD variables can be estimated from the image contour based on three-dimensional depth information.[8] Furthermore, several automatic segmentation schemes[12–23] have been developed for the assessment of the OD and parapapillary features, such as RNFL thickness.

The HRT and the OCT have been used in several studies about the PPA. One such application was by Uchida et al.,[13] who investigated the association between PPA and the progression of glaucoma. However, two-dimensional color fundus imaging may be preferred by many clinicians for estimating the size of the OD and PPA, because the image from HRT or OCT is generated via computer processing rather than a direct recording of the object of interest.
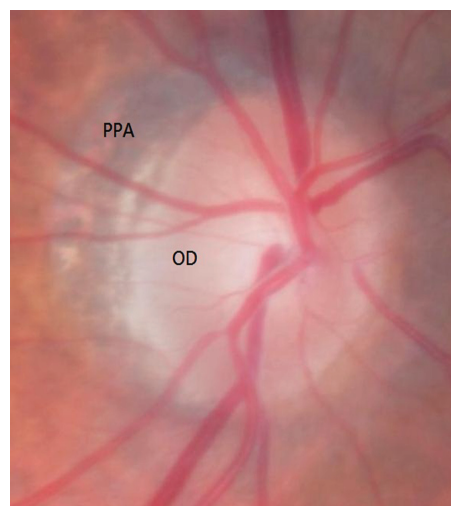
FIGURE 1.   Original fundus image with the OD and PPA.

An alternative tool to detect and quantify the PPA and the OD automatically from color fundus images would reduce the workload of the human assessor and could facilitate a wider investigation about the potential importance of PPA in ophthalmic disease diagnosis involving facilities where access to HRT or OCT is limited. Moreover, in large clinical studies and pathologic monitoring programs, such a computerized tool can also improve repeatability, therefore avoiding problems associated with fatigue and habituation, and tends to be more cost effective.

A novel approach to automatically segment and quantify the OD and PPA region from color fundus images is proposed in this article. The methodology exploits both the red and blue channels of the color fundus image to maximize extraction of information on the features (PPA), while keeping interference (blood vessels) to a minimum. A combination of several techniques, including scanning filter, autothresholding, and region-growing, as well as the Chan-Vese (C-V) model with a shape restraint is used to segment and quantify the regions of the OD and PPA.

METHODS

We used color retinal images drawn from a subsample of the Lothian Birth Cohort (LBC), a 1936 study.[24] The participants comprise surviving members of the Scottish Mental Survey of 1947 ($n = 70,805$) who were born in 1936 and currently reside in the Edinburgh area (Lothian) of Scotland. Eight hundred sixty-six of them were successfully traced and participated in a series of investigations that included having retinal photographs taken at the Wellcome Trust Clinical Research Facility, Western General Hospital, NHS Lothian, Scotland. Their mean age at the time of the photography was 72 years. The research complied with the Declaration of Helsinki and was approved by the Lothian (Scotland A) Research Ethics Committee.

The computer program in this work was implemented in commercial software (MatLab; MathWorks Inc., Natick, MA). The images were evaluated by an ophthalmologist (AL) who was masked to the image processing findings. The intensity variation between the bright objects (i.e., the OD and the PPA) and the blood vessels of the retinal image was relatively high (Fig 1). Conversely, the blood vessels were in general at a lower intensity level with respect to the background.

Our proposed algorithm combined a collection of image-processing techniques (Figure 2). Fundus images were initially preprocessed in two channels of the RGB space to reduce the interference of blood vessels and to better distinguish the regions of OD and PPA. The OD region could be reliably detected in the red channel, as it appeared brighter than the rest of the image, while the blood vessels appeared least influential.[20] We also found that the region consisting of both the OD and the PPA (hereafter referred to as the region of OD-plus-PPA) was most well-defined in the blue channel. Consequently, the region of OD-plus-PPA was first segmented by a modified C-V model in the blue channel. Then, a variant of the C-V model with a shape restraint was applied to segment the OD region in the red channel. In this case, the restraint was based on an ellipse reflecting the actual shape of an OD. Removing the OD region from the region of OD-plus-PPA produced the first-order estimation of the PPA region. Moving back to the blue channel, the segmented image was then equally divided into four zones automatically.

Based on the autoset thresholds acquired from each zone, the image was then filtered to reduce the influence of crossing vessels and artifacts. Finally, the PPA was extracted by using a multiseed region-growing method.[25]

Chan-Vese Model

The C-V model is a type of active contour model or "snake" that can trace the outline of an object from an image by minimizing an energy

FIGURE 2.   Flow chart shows the extraction of the PPA and the OD regions.

114

function associated with the current object contour.[26] It combines methods including curve evolution, Mumford-Shah function,[27] and level sets for applicat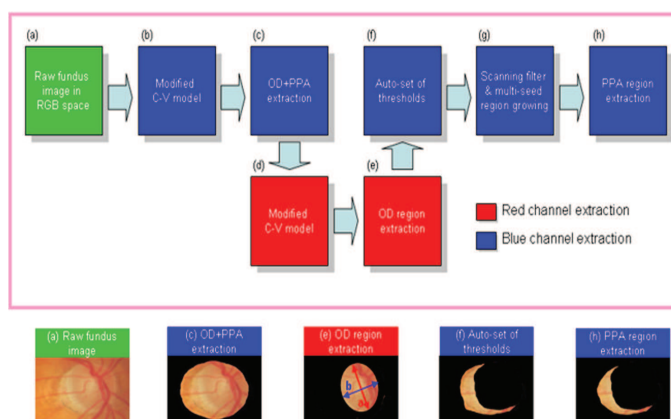ions such as shape recognition, edge detection, and image segmentation. In this work, we used it to identify topological changes, corners, and cusps associated with the presence of PPA. The C-V model has been enhanced to detect objects whose boundaries are not all necessarily well-defined. The step size of the energy function was selected carefully, to ensure that the snake would stop at the desired boundary. More details on the C-V model are given in Supplementary Material S1 (http://www.iovs.org/lookup/suppl/doi:10.1167/iovs.10-6572/-/DCSupplemental).

Segmentation with the Modified C-V Model

As the OD region appears to be more or less an ellipse, we adopted the model of Tang et al.[28] which integrated the C-V model with an elliptical shape restraint. More details on the model are given in Supplementary Material S2 (http://www.iovs.org/lookup/suppl/doi:10.1167/iovs.10-6572/-/DCSupplemental) We also used it to segment the OD-plus-PPA region. However, the PPA region may sometimes appear in an irregular shape, and so we had to modify the rules slightly for the evolution of the C-V model. The set of starting C-V model points, also known as the initial mask, was arranged to be in an ellipse as per normal. However, the model was then allowed to deform freely as it edged closer to the boundary of OD-plus-PPA with each subsequent iteration. This method allowed the model to produce an enclosed but not necessarily elliptical shape, which was always bigger than the exact region of the OD-plus-PPA.

Next, Tang's C-V model was employed to detect the OD region. To accurately segment the OD, we introduced two modifications to the model. First, Tang's equation B-3[28] was restored to its original form (of an ellipse):

$$\frac{da(t)}{dt} = - \int_\omega [\alpha(u_0 - c_1)^2 - (1 - \alpha)$$
$$\times (u_0 - c_2)^2]\delta(\varphi)A^2(1/a^3)dxdy. \quad (1)$$

Second, we introduced a new way to automatically detect the center of the OD for more accurate segmentation. We divided the image into four subregions. Then, we adopted the approach used in Tang's model to estimate the initial mask center (x_0, y_0). The initial function in the equation B-2[28] was chosen as:

$$\phi_0(x,y) = 1 - (\sqrt{(x - x_0)^2 + (y - y_0)^2})/R \quad (2)$$

where R is the estimated radius of the OD and can be defined as

$$R = min\{min[x_0 / 2,(w - x_0) / 2],min[y_0 / 2,(b - y_0)/2]\} \quad (3)$$

where w and b are the width and height of the image, respectively.

Then, our algorithm calculated automatically the offset, f_x and f_y, of the initial mask center, based on the histogram of intensity value of each four regions. The updated initial mask center is thus

$$(x_0', y_0') = (x_0 + f_x, y_0 + f_y). \quad (4)$$

Autosetting of Thresholds and Scanning Filter

To eliminate the unwanted pixels in the oversized OD-plus-PPA region, we acquired threshold values from the histogram of intensity values in the four subregions. In this context, the threshold was set by the brightest 30% of all pixels in each region, thus producing a better-defined OD-plus-PPA region. We then subtracted the OD region and obtained the first-order estimation of the PPA region as illustrated in Figure 2f.

The PPA region is a nonhomogeneous area divided into multiple sections by a few crossing blood vessels. We therefore proposed the use of a scanning 1×3 filter to create a path through the vessels for the following region-growing model to reach different sections of the PPA.

Multi-initial Seed Region-Growing

The seeded region-growing technique was first introduced by Adams and Bischof.[25] It starts with several initial seeds and then adds adjacent points as new seeds, beginning with the points of lowest priority. The priority is defined by a distance function. The distance of each pixel to a contiguous region[22] is defined by:

$$R(x,\delta_i) = [I(x) - mean_j \in \delta_i(I(j))] \quad (5)$$

where $I(x)$ is the gray image value of the point x(element) δ and δ_i, the region labeled i. Above all, setting both the right initial seed and distance function is the most important step in PPA extraction.

Our algorithm automatically placed one initial seed in each of the four subregions and set an optimal distance function for each subregion. Each seed was then allowed to grow until the regional threshold distance set by equation 5 was met. Finally, we combined the results at all four subregions to produce an integrated PPA region. By combining the techniques listed above, our methodology permitted the full use of both global and local information for PPA and OD segmentation.

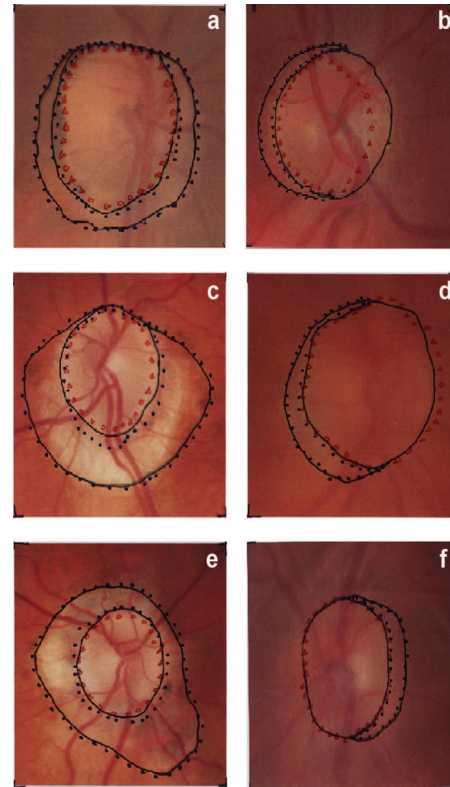**FIGURE 3.** Segmentation results from the proposed algorithm. Shown are (**a**, **c**, **e**) good-quality and (**b**, **d**, **f**) poor-quality images. *Black solid line*: the ground estimate; *black dots* and the *red markings*: the estimated PPA and OD regions, respectively.

RESULTS

A total of 94 color fundus images (including 18 poor-quality images, as determined by an independent and experienced human assessor, AL) from 66 subjects were randomly selected from the Lothian Birth Cohort (LBC) database. Without knowing the segmentation results from the proposed tool, the human assessor provided the ground estimate of the OD and the PPA region in the images. Subsequently, the area enclosed by the ground estimate was counted pixel by pixel (Photoshop; Adobe Systems Inc.) to quantify the size of each region. The count was repeated with the segmentation results from the tool.

Figure 3 shows six samples from the segmentation results of the proposed tool. The first column depicts the results obtained from good-quality images, and the second column depicts the results from poor-quality images. The ground estimate is enclosed by the black solid line. The results of estimated PPA and OD region are enclosed by the spots and red markings, respectively. Figure 4a shows the comparison of the OD area (in arbitrary pixel unit), based on the ground estimate, and the estimated OD area, determined by the proposed tool in the 94 trials, along with the line of best fit. Figure 4b shows a similar graph but for the PPA area size estimation.

The results suggest that the proposed algorithm or estimation model was able to detect the general boundary of OD and PPA. However, it tended to terminate the snake evolution prematurely on all good-quality images; hence, the results appeared to underestimate the actual size. This underestimation was consistent in the case of poor-quality images, in which the intensity variation/resolution in defining the boundary of OD was limited. Figure 3d shows a good example of when the model missed the mark by pushing the boundary into the scleral rim. Overall, it appears that most of the results in the 94 trials are underestimations. This is confirmed by the gradients (both <1) of the best-fit lines in Figures 4a and 4b. We therefore calibrated our estimation model by using these values as scaling factors. The final estimation results are plotted in Figures 4c and 4d. As shown, a correlation coefficient of 0.98 (max = 1) was achieved in the size estimation of both the OD and PPA regions. This result suggests that our estimation is not stochastic but is fairly consistent with the ground estimate defined by an ophthalmologist (i.e., the best-fit line is defined by the equation $y = x$).

Validity of the Tool

In this section, we use three methods to validate our estimation model. First, we calculated the mean accuracy (MA) of our estimation model, which is given by:

$$MA = \left(1 - \frac{\sum_{i=1}^{n}\left(\frac{S_a - S_e}{S_a}\right)}{n}\right) \times 100\% \qquad (6)$$

where S_a represents the actual size (ground estimate) of PPA or OD, while S_e represents the estimated size (by our model) of PPA or OD. The numerical value n is the total number of images analyzed in our experiment. Before calibration, our estimation model achieved a mean (SD) accuracy level of 90.0% (6.20%) and 88.2% (5.85%), in defining the size of OD and PPA, respectively. With the same set of color fundus images, our estimation model after calibration achieved a mean (SD) accuracy level of 94.0% (5.88%) and 93.8% (5.26%). Table 1 summarizes the estimation results.

Second, we calculated the sensitivity of our estimation model at different tolerance levels. In this context, tolerance level refers to the percentage of estimation error being acceptable. When the estimation result by our model falls within the

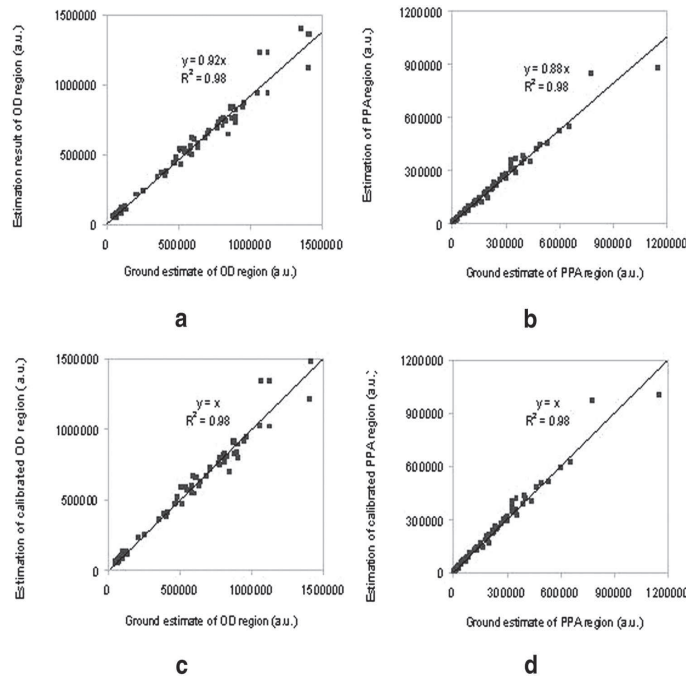

FIGURE 4. The correlation between the ground estimate (*x*-axis) and the results obtained by the proposed tool (*y*-axis) in quantifying the size of each region, in arbitrary pixel units. (**a**, **b**) Direct estimation results from the tool; (**c**, **d**) estimation results of the OD and PPA region after calibration, such that $y = x$. The correlation coefficient was 0.98 in all cases.

TABLE 1. The Results of PPA and OD Segmentation in 94 Trials

Results	Before Calibration		After Calibration	
	PPA	OD	PPA	OD
Mean accuracy, %	88.2	90.0	93.8	94.0
Standard deviation	5.85	6.20	5.26	5.88
Correlation coefficient, R^2	0.98	0.98	0.98	0.98

range of tolerance, we count it as one correct prediction, and vice versa. The sensitivity is defined as the percentage of correction prediction over the total number of images analyzed in our experiment. Our model after calibration achieved a sensitivity of 75.5% (tolerance, ±10%) and 90.4% (tolerance, ±15%) in estimating the size of OD region. As expected, the sensitivity level is lower when the tolerance is smaller and when our model is not calibrated (Fig. 5a). The scatterplots in Figure 5b show a similar trend. After calibration, the sensitivity of our model for the PPA region was 84.0% (tolerance, ±10%) and 92.6% (tolerance, ±15%), respectively.

Third and finally, we evaluated the robustness of the calibration method for our estimation model. We randomly selected 70 of the 94 images and derived the suitable scaling factor to calibrate the segmentation results, according to the aforementioned methodology. Then, we used the remaining 24 images to obtain the accuracy of the calibrated model. In this case (labeled RA), the mean (SD) accuracy was 94.0% (5.77%) and 94.3% (4.53%) in defining the size of OD and PPA, respectively, in the 24 test images. We repeated this experiment by (1) calibrating our model with images that had the largest (70/94; 74.5%) PPA and had remaining images from the dataset—that is, those with the smallest (24/94; 21.3%) PPA as test images, and (2) calibrating with the smallest (74.5%) PPA and testing with the largest (21.3%) PPA. The earlier (labeled HI) achieved a mean (SD) accuracy of 92.7% (7.53%) and 92.8% (4.93%) for size estimation of the OD and PPA regions, respectively. On the other hand, the latter (labeled LO) achieved a mean (SD) accuracy of 93.7% (6.98%) and 93.4% (6.57%) for the OD and PPA. Table 2 summarizes the results, including the previous results from calibrating with all 94 images (labeled AL). As expected, the model performed the worst when it was calibrated with the largest PPA images and tested with the smallest PPA images. However, the mean accuracy of our model is still greater than 92.7%.

DISCUSSION

We have developed automated software to measure the size of PPA and the OD in two-dimensional fundus images. Our experimental results with a very wide variety of fundus images showed that the proposed algorithm was not only robust for automatic PPA shape detection and area quantification, but it could also provide the transverse and conjugate diameter of the OD as well as PPA-to-OD ratio, which may be useful in early detection and grading of eye conditions such as glaucoma.

The automatic detection and the quantification of OD in fundus images are particularly important tasks in retinal image analysis for two reasons: First, the OD has attributes similar to the PPA, both in terms of contrast and brightness, making their boundary detection a difficult task. Second, the OD is often seen as a landmark that can be used for a coarse localization of the area of interest in retinal images, reducing the search area during the preprocessing stage.

Several schemes for automatic segmentation of the OD have been reported.[11,14–19,21–23] The OD can be detected either by finding a large cluster of pixels with high intensity[22,23] or by the highest intensity variation at the gray level[11,21]; however, difficulties are often encountered when exudates coexist within the retinal image, because exudates also have a higher intensity level than the surrounding regions of the OD. Walter et al.[19] developed a combined approach of watershed transformation and morphologic filtering to detect OD, but found that morphologic filtering could not completely remove the distortion caused by overlying retinal vessels. Another approach used an area-thresholding algorithm to localize the OD,[18] before detecting its boundary by means of a Hough transform (HT) (i.e., best fitting circle based on the gradient information of the image). However, this approach proved to be time consuming and relied on certain forms of the OD that were not always encountered. Principal component analysis (PCA) for automatic detection of the OD has been reported[17] and could be used, even in the presence of bright lesions on the fundus image, although this approach could also be time-consuming. Alternatively, Osareh et al.[16] used a template-matching algorithm to detect the disc boundary automatically. Although morphologic preprocessing helped to reduce the interference effects of blood vessels, it could not remove them completely. Moreover, such processing blurred the OD boundary, making the detection unreliable. The C-V method[15] and level setting methods[14] have also been applied to OD boundary segmentation. The major advantage of these algorithms is their ability to compensate discontinuities in the boundary of the image fea-
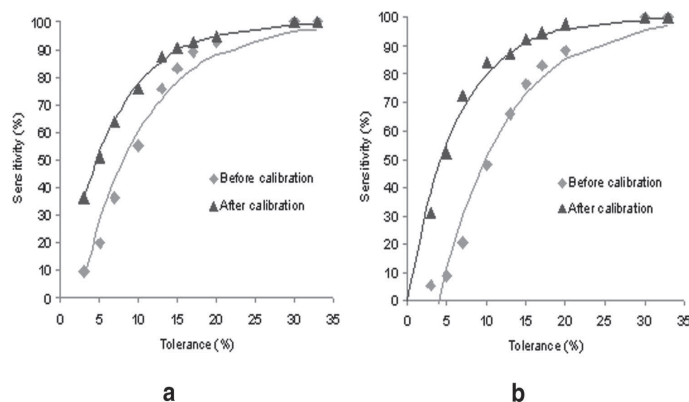

FIGURE 5. The sensitivity of the proposed tool in defining the size of (**a**) the OD and (**b**) the PPA regions at different tolerance levels in the 94 trials. The slopes represent the best fit for the scatterplots.

TABLE 2. The Statistical Data of PPA and OD Segmentation Results in Different Combinations of Calibration and Test Images

	OD				PPA			
	HI	**RA**	**LO**	**AL**	**Hi**	**RA**	**LO**	**AL**
Scaling factor	0.92	0.91	0.90	0.92	0.88	0.87	0.89	0.88
Correlation coefficient	0.97	0.98	0.99	0.98	0.97	0.97	0.99	0.98
Mean accuracy, %	92.7	94.0	93.7	94.0	92.8	94.3	93.4	93.8
Standard deviation	7.53	5.77	6.98	5.88	4.93	4.53	6.57	5.26

All images were taken from the same set of LBC images.

ture to be located. However, those approaches have to be carefully initialized and can achieve only good segmentation results when the region has homogenous intensity values and a well-defined boundary.

In this work, we explored a dual-channel approach with a modified C-V model to segment the PPA and the OD individually. The proposed algorithm particularly is designed to address the aforementioned challenges on how to maximize information extraction of features (OD/PPA) while keeping interference (blood vessels) to a minimum.

In comparison to the works by other groups, there are three main merits of the proposed tool. First, our software tool could measure the PPA region automatically in two-dimensional color fundus images. This tool is the first tool that can make that measurement without human intervention. In previous studies, investigators had to manually measure the PPA region in either 2-D [3–9] or 3-D [13] images, which were constructed by specially written planimetry computer programs. Second, the proposed tool not only detected the OD region and estimated its size, it also provided readings of the transverse and conjugate diameter—two commonly used parameters in retinal image analysis. Using this tool, we could further derive the normalized PPA size (i.e., the ratio between the PPA and the OD size) to explore its association with different eye diseases or conditions and establish a better understanding about the significance of the PPA development. Third, this tool has been automated, which means that not only could it reduce the dependence on the human assessor and thus potentially avoid problems associated with human errors such as fatigue, it could also be more cost effective for larger scale population-based screening.

There remain some limitations within our method, however: First, our software stopped at undesired points on encountering irregular dark pixels before the OD boundary in good-quality images and less consistently in poor-quality images. This problem results in underestimation of the actual size. Second, the proposed algorithm estimates the *sizes* of OD and PPA regions, providing a means to measure the extent of PPA. It would be ideal if the software could also define the *absolute shapes*, allowing the patterns in PPA progression to be studied in different eye conditions. A possible way to address these above limitations would be to take into consideration additional local information (e.g., texture) and explore further the image fusion from multiple channels.

CONCLUSIONS

We have demonstrated that PPA on a retinal image can be quantified by means of computer-aided software. Our proposed algorithm or estimation model, after calibration, achieved an accuracy of 94.0% (SD 5.88%) and 93.8% (5.26%) in defining the size of the OD and PPA, respectively, compared with the gold standard experienced human assessor. Our model also showed high reliability in estimating the size, with the correlation coefficient reaching 0.98 for both cases (OD

and PPA). In terms of sensitivity, our model achieved 75.5% and 84.0% (tolerance, ±10%) in size estimation of the OD and PPA region, and higher when we increased the tolerance level. We have also investigated the robustness of our calibration method and found that our model consistently achieved a mean accuracy of more than 92.7%. In addition, the proposed software could also provide ophthalmologists additional information, namely transverse and conjugate diameter of the OD as well as the ratio between the OD and PPA size, with potential application in eye-screening programs. The methods developed so far are therefore promising as the basis for a fully automated prescreening technique that will prioritize images for subsequent expert human assessment.

References

1. Damms T, Dannheim F. Sensitivity and specificity of optic disc parameters in chronic glaucoma. *Invest Ophthalmol Vis Sci.* 1993; 34:2246–2250.
2. Heijl A, Leske MC, Bengtsson B, Hyman L, Hussein M. Reduction of intraocular pressure and glaucoma progression: results from the Early Manifest Glaucoma Trial. *Arch Ophthalmol.* 2002;120:1268–1279.
3. Healey PR, Mitchell P, Gilbert CE, et al. The inheritance of peripapillary atrophy. *Invest Ophthalmol Vis Sci.* 2007;48:2529–2534.
4. Tezel G, Kolker AE, Kass MA, Wax MB, Gordon M, Siegmund KD. Parapapillary chorioretinal atrophy in patients with ocular hypertension. I. An evaluation as a predictive factor for the development of glaucomatous damage. *Arch Ophthalmol.* 1997;115:1503–1508.
5. Honrubia F, Calonge B. Evaluation of the nerve fiber layer and peripapillary atrophy in ocular hypertension. *Int Ophthalmol.* 1989;13:57–62.
6. Xu L, Wang Y, Yang H, Jonas JB. Differences in parapapillary atrophy between glaucomatous and normal eyes: the Beijing Eye Study. *Am J Ophthalmol.* 2007;144:541–546.
7. Uhm KB, Lee DY, Kim JT, Hong C. Peripapillary atrophy in normal and primary open-angle glaucoma. *Korean J Ophthalmol.* 1998; 12:37–50.
8. Laemmer R, Horn FK, Viestenz A, Link B, Juenemann AG, Mardin CY. Measurement of autofluorescence in the parapapillary atrophic zone in patients with ocular hypertension. *Graefes Arch Clin Exp Ophthalmol.* 2007;245:51–58.
9. Kolar R, Laemmer R, Jan J, Mardin Ch Y. The segmentation of zones with increased autofluorescence in the junctional zone of parapapillary atrophy. *Physiol Meas.* 2009;30:505–516.
10. Jonas JB, Nguyen XN, Gusek GC, Naumann GO. Parapapillary chorioretinal atrophy in normal and glaucoma eyes. I. Morphometric data. *Invest Ophthalmol Vis Sci.* 1989;30:908–918.
11. Xu J, Chutatape O, Sung E, Zheng C, Kuan PCT. Optic disk feature extraction via modified deformable model technique for glaucoma analysis. *Pattern Recogn.* 1998;40:2063–2076.
12. Ehrlich JR, Radcliffe NM. The role of clinical parapapillary atrophy evaluation in the diagnosis of open angle glaucoma. *Clin Ophthalmol.* 2010;4:971–976.
13. Uchida H, Ugurlu S, Caprioli J. Increasing peripapillary atrophy is associated with progressive glaucoma. *Ophthalmology.* 1998;105:1541–1545.

Quantification of Parapapillary Atrophy in the Optic Disc   4677

14. Liu J , Wong DWK, Lim JH, et al. ARGALI: an automatic cup-to-disc ratio measurement system for glaucoma analysis using level-set image processing. *Proceedings of the 13th International Conference on Biomedical Engineering*. Vol 23. Berlin: Springer; 2009: 559 - 562.

15. Echegaray S, Soliz P, Luo W. Automatic initialization of level set segmentation for application to optic disc margin identification. *Proceedings of the 22nd International Conference of Computer-Based Medical Systems*. Piscataway, NJ: IEEE Press; 2009;1 - 4.

16. Osareh A, Mirmehdi M, Thomas B, Markham R. Comparison of colour spaces for optic disc localisation in retinal images. *Proceedings of the 16th International Conference on Pattern Recognition*. Piscataway, NJ: IEEE Press; 2002:743 - 746.

17. Li H, Chutatape O. Automated feature extraction in color retinal images by a model based approach. *IEEE Trans Biomed Eng*. 2004;51:246 - 254.

18. Niemeijer M, Abramoff MD, van Ginneken B. Segmentation of the optic disc, macula and vascular arch in fundus photographs. *IEEE Trans Med Imaging*. 2007;26:116 - 127.

19. Walter T, Klein JC, Massin P, Erginay A. A contribution of image processing to the diagnosis of diabetic retinopathy: detection of exudates in color fundus images of the human retina. *IEEE Trans Med Imaging*. 2002;21:1236 - 1243.

20. Xu J, Chutatape O, Chew P. Automated optic disk boundary detection by modified active contour model. *IEEE Trans Biomed Eng*. 2007;54:473 - 482.

21. Sinthanayothin C, Boyce JF, Cook HL, Williamson TH. Automated localisation of the optic disc, fovea, and retinal blood vessels from digital colour fundus images. *Br J Ophthalmol*. 1999;83:902 - 910.

22. Tamura S, Okamoto Y, Yanashima K. Zero-crossing interval correction in tracing eye-fundus blood vessels. *Pattern Recogn*. 1988; 21:227 - 233.

23. Liu Z, Chutatape O, Krishnan SM. Automatic image analysis of fundus photograph. *Proceedings of the 19th Annual International Conference IEEE Engineering in Medicine and Biological Society*. Piscataway, NJ: IEEE Press; 1997;524 - 525.

24. Deary IJ, Gow AJ, Taylor MD, et al. The Lothian Birth Cohort 1936: a study to examine influences on cognitive ageing from age 11 to age 70 and beyond. *BMC Geriatr*. 2007;7:28.

25. Adams R, Bischof L. Seeded region growing. *IEEE Trans Pattern Anal Mach Intell*. 1994;16:641 - 647.

26. Chan TF, Vese LA. Active contours without edges. *IEEE Trans Image Process*. 2001;10:266 - 277.

27. Mumford D, Shah J. Optimal approximation by piecewise smooth functions and associated variational problems. *Commun Pure Appl Math*. 1989;42:577 - 685.

28. Tang Y, LX, von Freyberg A, Goch G. Automatic segmentation of the papilla in a fundus image based on the C-V model and a shape restraint. *Proceedings of the 18th International Conference on Pattern Recognition*. Piscataway, NJ: IEEE Press; 2006: 183 - 186.

Automatic Parapapillary Atrophy Shape Detection and Quantification in Colour Fundus Images

Cheng-Kai Lu,Tong Boon Tang and Alan F. Murray
School of Engineering
The University of Edinburgh
Edinburgh, UK
{C.Lu, Tong-Boon.Tang, A.F.Murray}@ed.ac.uk

Augustinus Laude and Baljean Dhillon
Princess Alexandra Eye Pavilion
NHS-Lothian
Edinburgh, UK
draugustinuslaude@yahoo.com.sg &
Bal.Dhillon@luht.scot.nhs.uk

Abstract— **Parapapillary atrophy (PPA) in the retina has been associated with eye diseases (e.g. glaucoma) and certain eye conditions (e.g. myopia). However, no computer-aided measuring tool thus far is available to quantify the extent of the PPA. In this paper, a novel approach to automatically segment and quantify the optic disc (OD) and PPA is proposed. The methodology exploits both the red and blue channels of the colour image to maximise information extraction of features (PPA) whilst keeping interference (blood vessels) to a minimum. A combination of several techniques, including scanning filter, thresholding, region growing as well as modified Chan-Vese (C-V) model with a shape constraint is used to segment and quantify the OD and PPA. Our proposed approach is evaluated against the reference boundary drawn by an ophthalmologist. Experimental results show that our method can repeatedly detect both the sizes of the OD and PPA region automatically, and achieved a mean accuracy level of 91.3% and 92.5% in defining the size of the OD and PPA, respectively. Moreover, the correlation coefficient of the ground truth and the results from proposed method is 0.98 for both the PPA and OD.**

Index Terms— Optic disc, parapapillary atrophy, fundus image, glaucoma, Chan-Vese models.

I. INTRODUCTION

In the assessment of eyes, ophthalmologists pay much attention to changes or abnormalities detected on colour and shape of the parapapillary atrophy (PPA) and the optic disc (OD)**,** which are two major features of the retina. Consequently, the identification, shape analysis and quantification of the PPA and the OD region in the fundus images are of primary importance for the detection of certain conditions such as glaucoma.

To date, various methods have been investigated for the detection of the OD and the focus of those works is either to locate the centre of the OD [2] or to detect the boundary of the OD in fundus images. In [3], the OD was detected by a combination of watershed transformation and morphological filtering techniques. In [4], an area-thresholding was first applied to localise the OD. Its boundary was then detected by means of the Hough Transform (H.T.), i.e. best fitting a circle based on the gradient information of the image. However, this approach proved time consuming and relied on certain forms of the OD that were not always encountered. Besides the aforementioned methods, there exist other techniques such as the point distribution model [5] and principal component analysis (PCA) for automatic detection of the OD [6]. Alternatively, Osareh et al. [7] used template matching to detect the disc boundary automatically. Although the morphological pre-processing (e.g. opening/closing) helped to reduce the effects of blood vessels, it could not remove them completely. Moreover, such processing blurred the OD boundary, making the boundary detection unreliable. In [8], OD was localised by capitalizing on its high variation on gray level image. This approach worked well, but only if there was none or very little PPA. The presence of the PPA could complicate the detection of the OD as it also appeared bright in the fundus images.

A novel method for automated quantification of both the sizes of the OD and PPA region is proposed in this paper based on a hybrid image processing technique. In particular, we aimed to address the aforementioned challenge on how to minimise the influence of blood vessels without sacrificing accuracy. In the presence of PPA, the common practice of working on single colour channel or gray-level was only adequate for locating the OD but not for defining its boundary. Therefore, the original fundus images were initially pre-processed in two different channels in RGB space to reduce the interference of blood vessels and to distinguish the regions of OD and PPA separately. Thereafter, the region of PPA-plus-OD was segmented by Chan-Vese (C-V) model on the blue channel. In order to segment OD appropriately, the C-V model with elliptic constraints needs to be employed. The segmented image was then divided into multi-zone automatically. Based on the auto-set thresholds

acquired from each zone, the segmented image was then filtered to reduce the influence of crossing vessels and artefact. Finally, PPA was derived from using a multi-seed region growing method.

Simulation results with a very wide variety of fundus images showed that the method presented in this paper is not only very effective for automatic PPA shape detection and region quantification, but can also provide the transverse and conjugate diameter of OD as well as the PPA-to-OD ratio, which can be useful information for early detection and grading of certain eye conditions such as glaucoma.

The rest of this paper is organised as follows. In Section II, the methodology for segmenting OD region and PPA region is presented. Section III presents the simulation results before a conclusion of this study is provided.

Fig.2 Original fundus image with the OD plus PPA
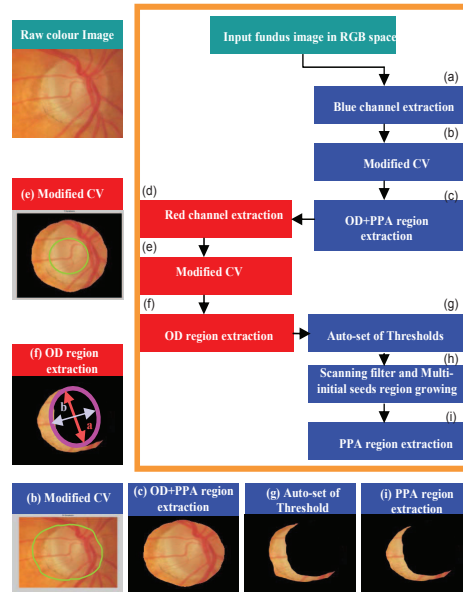
II. PROPOSED METHODOLOGY

Fig.1 Flow chart of the extraction of PPA and the OD region. The green lines in (b) and (e) represent the final mask and the initial mask of two different region extractions.

The steps used in our proposed method are shown in Fig. 1 and will be explained in details in the following subsections. Fig.2 shows an example of original fundus image. The intensity variation between the bright objects (i.e. the OD and PPA) and the blood vessels is relatively high. Conversely, the blood vessels are generally at a lower intensity level with respect to the background.
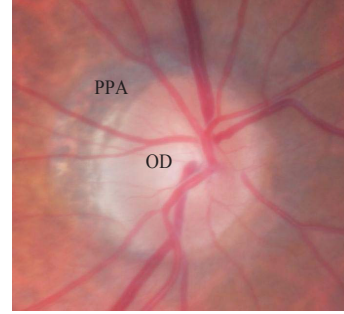
To isolate the OD, PPA and other bright parts separately is a non-trivial task. Pre-processing of the image is essential. The C-V model only worked well on an image with homogeneous regions enclosed by intense gradient information. Applying them directly to our fundus images is extremely difficult, as the area of the OD and PPA is invariably fragmented into multiple regions by the blood vessels. Previous work [3-8] used gray-level morphology to remove the blood vessels to create a relatively homogeneous region before applying the C-V model on the image. Similar morphological operations are equally applicable to the red and blue channels. We worked specifically on these two channels because we found that the blood vessels are least influential in the Red channel and the region of PPA-plus-OD is most well-defined in the Blue channel.

A. OD+PPA region and OD extraction using Modified C-V model

The original C-V model [9] combined the methods such as curve evolution, Mumford-Shah function and level sets for image segmentation. Because the OD appears more or less an ellipse or a circle, Tang [10] proposed a modified C-V model which included an elliptic shape constraint. The new "fitting energy" function E is then:

$$\inf_{c_1,c_2,\varphi} \{E[c_1,c_2,\varphi\,|\,u_0] = \alpha \int_\Omega (u_0-c_1)^2 H(\varphi) + (1-\alpha)\int_\Omega (u_0-c_2)^2 (1-H(\varphi))\} \quad (1)$$

Subject to

$$\varphi = 1 - [((x-x_0)\cos\theta + (y-y_0)\sin\theta)^2/a^2 + (-(x-x_0)\sin\theta + (y-y_0)\cos\theta)^2/b^2]^{1/2} \quad (2)$$

where Lipschitz function $\phi:\Omega\to\Re$ of R^2, $\alpha > 0$ is fixed parameters, $H(\varphi)$ is the Heaviside function. In addition, x_0, y_0, θ, major axis 'a', minor axis 'b' are the parameters of the ellipse at $\phi=0$. The evolutions related to the Euler-Lagrange equations are:

$$\frac{da(t)}{dt} = -\int_\Omega [\alpha(u_0 - c_1)^2 - (1-\alpha)(u_0 - c_2)^2]\delta(\varphi)A(1/a^3)dxdy \qquad (3)$$

$$\frac{db(t)}{dt} = -\int_\Omega [\alpha(u_0 - c_1)^2 - (1-\alpha)(u_0 - c_2)^2]\delta(\varphi)B^2(1/b^3)dxdy \qquad (4)$$

$$\frac{dx_0(t)}{dt} = -\int_\Omega [\alpha(u_0 - c_1)^2 - (1-\alpha)(u_0 - c_2)^2]\delta(\varphi)Ldxdy \qquad (5)$$

$$\frac{dy_0(t)}{dt} = -\int_\Omega [\alpha(u_0 - c_1)^2 - (1-\alpha)(u_0 - c_2)^2]\delta(\varphi)Mdxdy \qquad (6)$$

$$\frac{d\theta(t)}{dt} = -\int_\Omega [\alpha(u_0 - c_1)^2 - (1-\alpha)(u_0 - c_2)^2]\delta(\varphi)Ndxdy \qquad (7)$$

Here, $\delta(\varphi)$ is the Dirac function and

$$c_1 = (\int_\Omega u_0 H(\varphi)dxdy)/(\int_\Omega H(\varphi)dxdy)$$
$$c_2 = (\int_\Omega u_0(1 - H(\varphi))dxdy)/(\int_\Omega (1 - H(\varphi))dxdy)$$

$$A = (x - x_0)\cos\theta + (y - y_0)\sin\theta$$
$$B = -(x - x_0)\sin\theta + (y - y_0)\cos\theta$$
$$L = A\cos\theta/a^2 - B\sin\theta/b^2$$
$$M = A\sin\theta/a^2 + B\cos\theta/b^2$$
$$N = AB[1/b^2 - 1/a^2]$$

Therefore, the steady solution of Eq(2-7) at time T :

$$1 = [((x - x_0(T))\cos(\theta(T)) + (y - y_0(T))\sin(\theta(T)))^2/(a(T))^2 \\ + (-(x - x_0(T))\sin(\theta(T)) + (y - y_0(T))\cos(\theta(T)))^2/(b(T))^2]^{1/2} \qquad (8)$$

In our application, we imported this methodology to extract the OD and an over-sized PPA-plus-OD region. But we slightly modify the rules for the evolution of the C-V models because of the fact that PPA region may sometimes also appear in an irregular shape when segmenting the PPA-plus-OD region in the blue channel.

In Tang's C-V model, the mask always evolved with an elliptic shape. But, for PPA-plus-OD segmentation, we only set up an ellipse as the initial mask. The model was then allowed to produce an enclosed but not necessary elliptical in shape region (mask), which is always bigger than actual region of PPA-plus-OD in the red channel.

Next, Tang's C-V model was used to detect the OD region. In order to segment OD properly, we introduced two modifications to the model. Firstly, Eq(3) was restored to the original form (of an ellipse):

$$\frac{da(t)}{dt} = -\int_\Omega [\alpha(u_0 - c_1)^2 - (1-\alpha)(u_0 - c_2)^2]\delta(\varphi)A^2(1/a^3)dxdy \qquad (9)$$

Secondly we introduced a new way to detect the centre of the OD for better segmentation. First, we divided the raw image into four sub-regions. Then, we estimated the initial mask centre (x_0, y_0). Our software automatically set up offset, f_x and f_y, of the detected OD centre (x_c, y_c), based on the histogram of intensity value of each four regions.

$$(x_0, y_0) = (x_c + f_x, y_c + f_y) \qquad (10)$$

The initial function in Eq (2) was chosen as

$$\varphi_0(x, y) = 1 - (\sqrt{(x - x_0)^2 + (y - y_0)^2})/R \qquad (11)$$

Here, R is the estimating radius of the OD and could be simply taken as:

$$R = \min\{\min\{x_0/2, (w - x_0)/2\}, \min\{y_0/2, (h - y_0)/2\}\} \qquad (12)$$

where, w and h are the width and height of an image respectively.

B. Auto-Set of Thresholds

In order to remove the unwanted pixels of the over-sized PPA+OD region, we acquired threshold values from the histogram of intensity values in the four sub-regions. In this context, the threshold was set by the brightest 30% of all pixels in each region. This gave a better-defined PPA+OD region. We then subtracted the OD and obtained the first order estimation of the PPA region as illustrated in Fig.1(g).

C. Scanning filter and Multi-Initial Seed Region Growing

The seeded region growing technique was first introduced by Adams and Bischof [11]. It starts with several initial seeds and then adds adjacent points as new seeds, beginning by the points of lowest priority. The priority is defined by a distance function. In [11] the distance of the pixel to a contiguous region is defined by:

$$R(x, \delta_i) = [I(x) - mean_j \in \delta_i(I(j))] \qquad (13)$$

where $I(x)$ is the image I value in $x \in \delta$ and δ_i the region labelled i. Setting both the right initial seed and distance function is vital to the PPA extraction in the subsequent stage.

Since the PPA region is a non-homogeneous region with a few crossing vessels, we adopted the 'multi-seed' idea from [11], and proposed using a scanning [1x3] filter to create a passage through the vessels for region growing. The algorithm automatically places an initial seed at each sub-region and set an optimal distance function for each region. Finally, we integrated the segmented result of the PPA region as a whole image. By combining the techniques listed above, our methodology permits the full use of both global and local information for PPA and OD segmentation.

III. RESULTS

For our experiments, we used colour fundus images from the Lothian Birth Cohort (LBC) database [12]. Fig.3(a) shows the experimental results obtained from the good quality fundus images whilst Fig.3(b) shows results of poor quality or faint images.
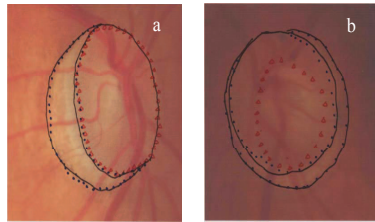
88

Fig 3. Segmented results on (a) good quality image, and (b) poor quality image

In Fig.3, the ground truth is drawn on the black solid line. The result of estimated PPA and OD region are enclosed by the blue dotted line and red triangle line, respectively. The results of randomly selected fundus images in forty trials are shown in Fig.4 and Fig.5. The estimated size and ground truth of the OD and PPA (in arbitrary unit) are represented in the Y-axis and X-axis, respectively.
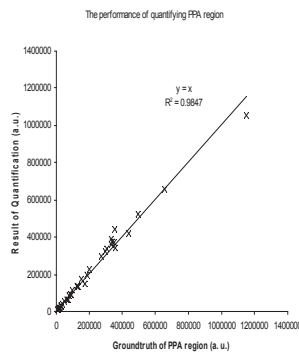

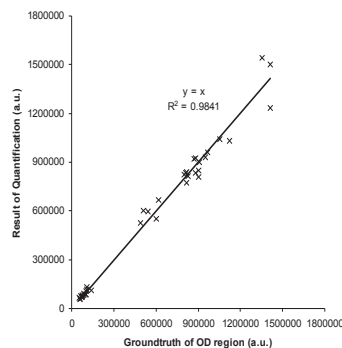Fig 4. The performance of quantifying the PPA region.

Fig 5. The performance of quantifying the OD region.

IV. CONCLUSION

A total of 40 images of 25 subjects with PPA, including eight faint images, were randomly selected for test. Our proposed method achieved 91.3% and 92.5% accuracy in defining the size of PPA and OD respectively, compared to the gold standard of a human expert (AL). In terms of correlation between the data of ground truth and our estimation, we obtained 0.98 for both the PPA and the OD. Moreover, our method can provide additional information, namely transverse and conjugate diameter of the OD as well as the ratio between the OD and PPA. Further work to test out this method in a larger sample set is indicated, in an effort to develop an automated screening system for diagnosis of eye conditions associated with PPA in the community.

ACKNOWLEDGMENT

REFERENCES

[1] K. H. Lim, Registration of new blindness in Singapore for 1985- 1995. *Med. J. Singapore*, vol 39, pp. 104-106, 1998.

[2] M. Lalonde, M. Beaulieu, and L. Gagnon, "Fast and Robust Optic Disk Detection using Pyramidal Decomposition and Hausdorff-Based Template Matching," *IEEE Trans. Med. Imaging*, vol. 20, No. 11, pp. 1193-1200, 2001.

[3] T. Walter, J.-C. Klein, P. Massin, and A. Erginay, "A contribution of image processing to the diagnosis of diabetic retinopathy—Detection of exudates in color fundus images of the human retina," *IEEE Trans. Med. Imaging*, vol. 21, No. 10, pp. 1236–1243, 2002

[4] S.Tamura and Y. Okamoto, "Zero-crossing interval correction in tracing eye-fundus blood vessels," *Pattern Recogn*, vol. 21, No.3, pp. 227–233, 1988.

[5] M. Niemeijer, M. D. Abramoff, and B. van Ginneken, "Segmentation of the optic disc, macula and vascular arch in fundus photographs," *IEEE Trans. Med. Imaging*, vol. 26, No. 1, pp. 116–127, 2007.

[6] H. Li, and O. Chutatape, "Automated feature extraction in color retinal images by a model based approach," *IEEE Trans. Biomed. Eng,* vol. 51, No. 2, pp. 246–254, 2004.

[7] A. Osareh, M. Mirmehd, B. Thomas, and R. Markham, "Comparison of colour spaces for optic disc localisation in retinal images," in *Proc. 16th Int. Conf. Pattern Recognition*, vol. 1, pp. 743–746, Aug. 2002.

[8] J. Xu, O. Chutatape, and P. Chew, "Automated Optic Disk Boundary Detection by Modified Active Contour Model", *IEEE Trans. Biomed. Eng.,* vol. 54, No. 3, pp. 473–482, March 2007.

[9] T. F. Chan, and L. A Vese , "Active contours without edges," *IEEE Trans. Image Processing*, vol. 10, No. 2, pp. 266-277, 2001.

[10] Yandong Tang, Xiaomao Lu, Axel von Freyberg, and Gert Goch, " Automatic Segmentation of the Papilla in a Fundus Image Based on the C-V model and a Shape Restraint," in *Proc. Int. Conf. Pattern Recognition (ICPR)*, Hong Kong, vol.1,pp.183-186, 18 september, 2006.

[11] R. Adams, and L. Bischof, "Seeded region growing", *IEEE Trans. Pattern Analysis and Machine Intelligence*, vol. 16, No. 6, pp. 641-647, 1994.

[12] I. J. Deary et al, "The Lothian Birth Cohort 1936: a study to examine influences on cognitive ageing from age 11 to age 70 and beyond," *BMC Geriatr.*, 7, 28, 2007.

89

Presentation Abstract

Program#/Poster#:	1800/A549
Abstract Title:	**Boundary Detection of Optic Disc and Parapapillary Atrophy From Color Fundus Images Using Dual-Channel Color Morphology and Snakes**
Presentation Start/End Time:	Monday, May 03, 2010, 1:45 PM - 3:30 PM
Session Number:	261
Session Title:	Image Post Processing⑥
Location:	Hall B/C
Reviewing Code:	244 image post processing and analysis methodologies (Poster Only) - MOI
Author Block:	*A. Laude[1,2], C.-K. Lu[3], T.B. Tang[3], A.F. Murray[3], R.D. Henderson[4], I.J. Deary[4], B. Dhillon[1].* [1]Department of Ophthalmology, Princess Alexandra Eye Pavilion, Edinburgh, United Kingdom; [2]Department of Ophthalmology, National Heatlhcare Group Eye Institute, Tan Tock Seng Hospital, Singapore; [3]School of Engineering, Edinburgh University, Edinburgh, United Kingdom; [4]Department of Psychology, Centre for Cognitive Ageing and Cognitive Epidemiology, Edinburgh, United Kingdom.
Keywords:	548 image processing, 624 optic disc, 473 computational modeling
Abstract Body:	**Purpose:** The presence of parapapillary atrophy (PPA) representing chorio-retinal atrophy around the optic disc (OD) has been associated with certain relatively common eye conditions (eg. Glaucoma and myopia). However, the significance of its development and extent has not been fully established. Although often detected in color fundus photography, there is to date no computer-aided measuring tool available for its accurate detection and measurement. We describe a novel approach to automatically segment the OD and PPA and compare this against the performance by an ophthalmologist. **Methods:** Pre-processing techniques were initially applied to color fundus images on the red and blue channels separately in order to segment the OD and the OD-plus-PPA respectively. Average filtering was performed within an initial mask to create an enclosed homogeneous area. The OD and OD-plus-PPA boundaries were then further segmented by using a free-form deformable model called 'snakes without edges', based on

124

techniques of curve evolution, level sets and 'Mumford-Shah functional'. We carefully selected the step size of the energy function to ensure that our snakes stopped at the desired boundaries. PPA was then derived from the subtraction of the OD from the OD-plus-PPA. We applied this technique on fundus images taken from a database of a well-characterized cohort and compared the accuracy of boundary detection against the manually-labeled ground truth information drawn by an ophthalmologist.

Results: Of the 33 randomly selected images of 25 subjects with PPA, 27 were of sufficient quality for analysis. Our proposed algorithm achieved a mean accuracy level of 86.6% *(S.D.*=5.9) in detecting OD, 87.1% *(S.D.*=6.5) in detecting OD-plus-PPA and 73.5% *(S.D.*=12.8) in detecting PPA.

Conclusions: Our proposed algorithm achieved good accuracy compared to the gold standard of a human expert. Further work to test out this algorithm in a larger sample is indicated. Possible application includes semi-automated screening systems for diagnosis of eye conditions associated with PPA in the community.

CommercialRelationships: **A. Laude:** None. **C.-K. Lu:** None. **T.B. Tang:** None. **A.F. Murray:** None. **R.D. Henderson:** None. **I.J. Deary:** None. **B. Dhillon:** None.

References

[1] D. T. Morris and C. Donnison, "Identifying the neuroretinal rim boundary using dynamic contours," *Image and Vision Computing*, vol. 17, no. 3, pp. 169–174, 1999.

[2] W. K. Pratt, *Digital Image Processing: Piks Scientific Inside*. John Wiley & Sons, Feb. 2007.

[3] T. Damms and F. Dannheim, "Sensitivity and specificity of optic disc parameters in chronic glaucoma.," *Investigative Ophthalmology & Visual Science*, vol. 34, pp. 2246 –2250, June 1993.

[4] W. M. Budde and J. B. Jonas, "Influence of cilioretinal arteries on neuroretinal rim and parapapillary atrophy in glaucoma," *Investigative Ophthalmology & Visual Science*, vol. 44, pp. 170–174, Jan. 2003. PMID: 12506071.

[5] J. R. Ehrlich and N. M. Radcliffe, "The role of clinical parapapillary atrophy evaluation in the diagnosis of open angle glaucoma," *Clinical Ophthalmology (Auckland, N.Z.)*, vol. 4, pp. 971–976, 2010. PMID: 20856591 PMCID: 2938276.

[6] H. Uchida, S. Ugurlu, and J. Caprioli, "Increasing peripapillary atrophy is associated with progressive glaucoma," *Ophthalmology*, vol. 105, pp. 1541–1545, Aug. 1998. PMID: 9709771.

[7] N. M. Tan, J. Liu, D. W. Wong, J. H. Lim, Z. Zhang, S. Lu, H. Li, S. M. Saw, L. Tong, and T. Y. Wong, "Automatic detection of pathological myopia using variational level set," in *Annual International Conference of the IEEE Engineering in Medicine and Biology Society, 2009. EMBC 2009*, pp. 3609–3612, IEEE, Sept. 2009.

[8] J. B. Jonas, "Clinical implications of peripapillary atrophy in glaucoma," *Current Opinion in Ophthalmology*, vol. 16, pp. 84–88, Apr. 2005. PMID: 15744137.

[9] A. Heijl, M. C. Leske, B. Bengtsson, L. Hyman, B. Bengtsson, M. Hussein, and for the Early Manifest Glaucoma Trial Group, "Reduction of intraocular pressure and glaucoma progression: Results from the early manifest glaucoma trial," *Arch Ophthalmol*, vol. 120, pp. 1268–1279, Oct. 2002.

[10] P. R. Healey, P. Mitchell, C. E. Gilbert, A. J. Lee, D. Ge, H. Snieder, T. D. Spector, and C. J. Hammond, "The inheritance of peripapillary atrophy," *Investigative Ophthalmology & Visual Science*, vol. 48, pp. 2529 –2534, June 2007.

[11] G. Tezel, A. E. Kolker, M. B. Wax, M. A. Kass, M. Gordon, and K. D. Siegmund, "Parapapillary chorioretinal atrophy in patients with ocular hypertension. II. an evaluation of progressive changes," *Archives of Ophthalmology*, vol. 115, pp. 1509–1514, Dec. 1997. PMID: 9400783.

[12] F. Honrubia and B. Calonge, "Evaluation of the nerve fiber layer and peripapillary atrophy in ocular hypertension," *International Ophthalmology*, vol. 13, pp. 57–62, Jan. 1989.

[13] L. Xu, Y. Wang, H. Yang, and J. B. Jonas, "Differences in parapapillary atrophy between glaucomatous and normal eyes: the beijing eye study," *American Journal of Ophthalmology*, vol. 144, pp. 541–546, Oct. 2007. PMID: 17651676.

[14] K. B. Uhm, D. Y. Lee, J. T. Kim, and C. Hong, "Peripapillary atrophy in normal and primary open-angle glaucoma," *Korean Journal of Ophthalmology: KJO*, vol. 12, pp. 37–50, June 1998. PMID: 9753950.

[15] R. Laemmer, F. K. Horn, A. Viestenz, B. Link, A. G. Juenemann, and C. Y. Mardin, "Measurement of autofluorescence in the parapapillary atrophic zone in patients with ocular hypertension," *Graefe's Archive for Clinical and Experimental Ophthalmology = Albrecht Von Graefes Archiv Fr Klinische Und Experimentelle Ophthalmologie*, vol. 245, pp. 51–58, Jan. 2007. PMID: 16896917.

[16] R. Kolr, R. Laemmer, J. Jan, and C. Y. Mardin, "The segmentation of zones with increased autofluorescence in the junctional zone of parapapillary atrophy," *Physiological Measurement*, vol. 30, pp. 505–516, May 2009.

[17] J. B. Jonas, X. N. Nguyen, G. C. Gusek, and G. O. Naumann, "Parapapillary chorioretinal atrophy in normal and glaucoma eyes. i. morphometric data," *Investigative Ophthalmology & Visual Science*, vol. 30, pp. 908–918, May 1989. PMID: 2722447.

[18] J. B. Jonas and W. M. Budde, "Diagnosis and pathogenesis of glaucomatous optic neuropathy: morphological aspects," *Progress in Retinal and Eye Research*, vol. 19, pp. 1–40, Jan. 2000. PMID: 10614679.

[19] E. J. Lee, T. Kim, R. N. Weinreb, K. H. Park, S. H. Kim, and D. M. Kim, "-Zone parapapillary atrophy and the rate of retinal nerve fiber layer thinning in glaucoma," *Investigative Ophthalmology & Visual Science*, vol. 52, pp. 4422–4427, June 2011. PMID: 21474770.

[20] A. Emdadi, Y. Kono, P. A. Sample, G. Maskaleris, and R. N. Weinreb, "Parapapillary atrophy in patients with focal visual field loss," *American Journal of Ophthalmology*, vol. 128, pp. 595–600, Nov. 1999.

[21] J. Xu, O. Chutatape, E. Sung, C. Zheng, and P. Chew Tec Kuan, "Optic disk feature extraction via modified deformable model technique for glaucoma analysis," *Pattern Recognition*, vol. 40, pp. 2063–2076, July 2007.

[22] I. J. Deary, A. J. Gow, M. D. Taylor, J. Corley, C. Brett, V. Wilson, H. Campbell, L. J. Whalley, P. M. Visscher, D. J. Porteous, and J. M. Starr, "The lothian birth cohort 1936: a study to examine influences on cognitive ageing from age 11 to age 70 and beyond," *BMC Geriatrics*, vol. 7, p. 28, Dec. 2007. PMID: 18053258 PMCID: 2222601.

[23] K. Anderson, A. El-Sheikh, and T. Newson, "Application of structural analysis to the mechanical behaviour of the cornea.," *Journal of the Royal Society Interface*, vol. 1, pp. 3–15, Nov. 2004. PMID: 16849148 PMCID: 1618927.

[24] A. Elsheikh, B. Geraghty, P. Rama, M. Campanelli, and K. M. Meek, "Characterization of age-related variation in corneal biomechanical properties," *Journal of The Royal Society Interface*, vol. 7, pp. 1475 –1485, Oct. 2010.

[25] M. U. Akram and A. Tariq, "Automated optic disk localization and detection in colored retinal images," in *Proceedings of the 7th International Conference on Frontiers of Information Technology*, FIT '09, (New York, NY, USA), p. 36:136:5, ACM, 2009.

[26] N. Patton, T. M. Aslam, T. MacGillivray, I. J. Deary, B. Dhillon, R. H. Eikelboom, K. Yogesan, and I. J. Constable, "Retinal image analysis: concepts, applications and potential.," *Progress in Retinal and Eye Research*, vol. 25, no. 1, pp. 99–127, 2006.

[27] N. M. Tan, J. Liu, D. W. K. Wong, Z. Zhang, S. Lu, J. H. Lim, H. Li, and T. Y. Wong, "Classification of left and right eye retinal images," *Proceedings of SPIE*, vol. 7624, pp. 762438–762438–8, Mar. 2010.

[28] M. Lalonde, M. Beaulieu, and L. Gagnon, "Fast and robust optic disc detection using pyramidal decomposition and hausdorff-based template matching," *IEEE Transactions on Medical Imaging*, vol. 20, pp. 1193–1200, Nov. 2001.

[29] M. D. Abrmoff, W. L. M. Alward, E. C. Greenlee, L. Shuba, C. Y. Kim, J. H. Fingert, and Y. H. Kwon, "Automated segmentation of the optic disc from stereo color photographs using physiologically plausible features," *Investigative Ophthalmology & Visual Science*, vol. 48, pp. 1665 –1673, Apr. 2007.

[30] J. Xu, H. Ishikawa, G. Wollstein, R. A. Bilonick, K. R. Sung, L. Kagemann, K. A. Townsend, and J. S. Schuman, "Automated assessment of the optic nerve head on stereo disc photographs," *Investigative Ophthalmology & Visual Science*, vol. 49, pp. 2512 – 2517, June 2008.

[31] S. Tamura, Y. Okamoto, and K. Yanashima, "Zero-crossing interval correction in tracing eye-fundus blood vessels," *Pattern Recogn.*, vol. 21, p. 227233, May 1988.

[32] A. Pinz, S. Bernogger, P. Datlinger, and A. Kruger, "Mapping the human retina," *IEEE Transactions on Medical Imaging*, vol. 17, pp. 606–619, Aug. 1998.

[33] M. Niemeijer, M. D. Abramoff, and B. van Ginneken, "Segmentation of the optic disc, macula and vascular arch in fundus photographs," *IEEE Transactions on Medical Imaging*, vol. 26, pp. 116–127, Jan. 2007.

[34] R. A. Abdel-Ghafar, T. Morris, T. Ritchings, and I. Wood, "Detection and characterisation of the optic disk in glaucoma and diabetic retinopathy," *Medical Image Understanding and Analysis*, pp. 2–5, Sept. 2004.

[35] H. Li and O. Chutatape, "Fundus image features extraction," in *Proceedings of the 22nd Annual International Conference of the IEEE Engineering in Medicine and Biology Society, 2000*, vol. 4, pp. 3071–3073 vol.4, IEEE, 2000.

[36] Z. Liu, C. Opas, and S. M. Krishnan, "Automatic image analysis of fundus photograph," in *Proceedings of the 19th Annual International Conference of the IEEE Engineering in Medicine and Biology Society, 1997*, vol. 2, pp. 524–525 vol.2, IEEE, Nov. 1997.

[37] J. Xu, O. Chutatape, and P. Chew, "Automated optic disk boundary detection by modified active contour model," *IEEE Transactions on Biomedical Engineering*, vol. 54, pp. 473–482, Mar. 2007.

[38] C. Sinthanayothin, J. F. Boyce, H. L. Cook, and T. H. Williamson, "Automated localisation of the optic disc, fovea, and retinal blood vessels from digital colour fundus images," *British Journal of Ophthalmology*, vol. 83, no. 8, pp. 902 –910, 1999.

[39] H. Li and O. Chutatape, "Automatic location of optic disk in retinal images," in *2001 International Conference on Image Processing, 2001. Proceedings*, vol. 2, pp. 837–840 vol.2, IEEE, Oct. 2001.

[40] H. Li and O. Chutatape, "Automated feature extraction in color retinal images by a model based approach," *IEEE Transactions on Biomedical Engineering*, vol. 51, pp. 246–254, Feb. 2004.

[41] Gagnon, M. Lalonde, M. Beaulieu, and M. C. Boucher, "Procedure to detect anatomical structures in optical fundus images," *Proceedings of SPIE*, vol. 4322, pp. 1218–1225, 2001.

[42] T. Kanade, J. Kittler, J. M. Kleinberg, F. Mattern, J. C. Mitchell, O. Nierstrasz, C. Pandu Rangan, B. Steffen, M. Sudan, D. Terzopoulos, D. Tygar, M. Y. Vardi, G. Weikum, P. M. D. S. Pallawala, W. Hsu, M. L. Lee, and K. A. Eong, "Automated optic disc localization and contour detection using ellipse fitting and wavelet transform," in *Computer Vision - ECCV 2004* (T. Pajdla and J. Matas, eds.), vol. 3022, pp. 139–151, Berlin, Heidelberg: Springer Berlin Heidelberg, 2004.

[43] A. Hoover and M. Goldbaum, "Locating the optic nerve in a retinal image using the fuzzy convergence of the blood vessels," *IEEE Transactions on Medical Imaging*, vol. 22, pp. 951–958, Aug. 2003.

[44] E. Trucco and P. J. Kamat, "Locating the optic disk in retinal images via plausible detection and constraint satisfaction," in *2004 International Conference on Image Processing, 2004. ICIP '04*, vol. 1, pp. 155– 158 Vol. 1, IEEE, Oct. 2004.

[45] M. Foracchia, E. Grisan, and A. Ruggeri, "Detection of optic disc in retinal images by means of a geometrical model of vessel structure," *IEEE Transactions on Medical Imaging*, vol. 23, pp. 1189–1195, Oct. 2004.

[46] A. Ruggeri, M. Forrachia, and E. Grisan, "Detecting the optic disc in retinal images by means of a geometrical model of vessel network," in *Proceedings of the 25th Annual International Conference of the IEEE Engineering in Medicine and Biology Society, 2003*, vol. 1, pp. 902– 905 Vol.1, IEEE, Sept. 2003.

[47] T. Walter, J. C. Klein, P. Massin, and A. Erginay, "A contribution of image processing to the diagnosis of diabetic retinopathy-detection of exudates in color fundus images of the human retina," *IEEE Transactions on Medical Imaging*, vol. 21, pp. 1236–1243, Oct. 2002.

[48] E. Corona, S. Mitra, M. Wilson, T. Krile, Y. H. Kwon, and P. Soliz, "Digital stereo image analyzer for generating automated 3-D measures of optic disc deformation in glaucoma," *IEEE Transactions on Medical Imaging*, vol. 21, pp. 1244–1253, Oct. 2002.

[49] K. Lee, M. Niemeijer, M. K. Garvin, Y. H. Kwon, M. Sonka, and M. D. Abramoff, "Segmentation of the optic disc in 3-D OCT scans of the optic nerve head," *IEEE Transactions on Medical Imaging*, vol. 29, pp. 159–168, Jan. 2010. PMID: 19758857.

[50] L. B-P, "Clinical update: Comprehensive. oct," *EyeNet Magazine*, 2006.

[51] S. Kavitha, S. Karthikeyan, and K. Duraiswamy, "Early detection of glaucoma in retinal images using cup to disc ratio," in *2010 International Conference on Computing Communication and Networking Technologies (ICCCNT)*, pp. 1–5, IEEE, July 2010.

[52] G. D. Joshi, J. Sivaswamy, and S. R. Krishnadas, "Optic disk and cup segmentation from monocular color retinal images for glaucoma assessment," *IEEE Transactions on Medical Imaging*, vol. 30, pp. 1192–1205, June 2011. PMID: 21536531.

[53] H. Li and O. Chutatape, "A model-based approach for automated feature extraction in fundus images," in *Ninth IEEE International Conference on Computer Vision, 2003. Proceedings*, pp. 394–399 vol.1, IEEE, Oct. 2003.

[54] J. Novo, M. G. Penedo, and J. Santos, "Optic disc segmentation by means of GA-Optimized topological active nets," in *Proceedings of the 5th international conference on Image Analysis and Recognition*, ICIAR '08, (Berlin, Heidelberg), p. 807816, Springer-Verlag, 2008.

[55] A. Osareh, M. Mirmehdi, B. Thomas, and R. Markham, "Comparison of colour spaces for optic disc localisation in retinal images," in *16th International Conference on Pattern Recognition, 2002. Proceedings*, vol. 1, pp. 743– 746 vol.1, IEEE, 2002.

[56] S. Echegaray, P. Soliz, and W. Luo, "Automatic initialization of level set segmentation for application to optic disc margin identification," in *22nd IEEE International Symposium on Computer-Based Medical Systems*, pp. 1–4, IEEE, Aug. 2009.

[57] J. Liu, D. W. K. Wong, J. H. Lim, H. Li, N. M. Tan, Z. Zhang, T. Y. Wong, and R. Lavanya, "ARGALI: an automatic Cup-to-Disc ratio measurement system for glaucoma analysis using level-set image processing," in *13th International Conference on Biomedical Engineering* (C. T. Lim and J. C. H. Goh, eds.), vol. 23, pp. 559–562, Berlin, Heidelberg: Springer Berlin Heidelberg.

[58] C. Muramatsu, T. Nakagawa, A. Sawada, Y. Hatanaka, T. Yamamoto, and H. Fujita, "Automated determination of cup-to-disc ratio for classification of glaucomatous and normal eyes on stereo retinal fundus images," *Journal of Biomedical Optics*, vol. 16, pp. 096009–096009–7, Sept. 2011.

[59] J. Liu, D. Wong, J. Lim, N. Tan, Z. Zhang, H. Li, F. Yin, B. Lee, S. Saw, L. Tong, and T. Wong, "Detection of pathological myopia by PAMELA with Texture-Based features through an SVM approach," *Journal of Healthcare Engineering*, vol. 1, pp. 1–12, Jan. 2010.

[60] R. C. Gonzalez, R. E. Woods, and S. L. Eddins, *Digital Image processing using MATLAB*. Dorling Kindersley, Sept. 2004.

[61] F. Adrian and R. Alan, "Colour space conversions," *Technical report, Westminster University, London*, Aug. 1998.

[62] H. R. Kang, *Computational Color Technology*. SPIE Press, May 2006.

[63] H. C. Andrews, A. G. Tescher, and R. P. Kruger, "Image processing by digital computer," *IEEE Spectrum*, vol. 9, pp. 20–32, July 1972.

[64] E. L. Hall, R. P. Kruger, S. J. Dwyer, D. L. Hall, R. W. Mclaren, and G. S. Lodwick, "A survey of preprocessing and feature extraction techniques for radiographic images," *IEEE Transactions on Computers*, vol. C-20, pp. 1032– 1044, Sept. 1971.

[65] E. L. Hall, "Almost uniform distributions for computer image enhancement," *IEEE Transactions on Computers*, vol. C-23, pp. 207– 208, Feb. 1974.

[66] H. Robert, "Image enhancement by histogram transformation," *Computer Graphics and Image Processing*, vol. 6, pp. 184–195, Apr. 1977.

[67] D. J. Ketcham, "Real-time image enhancement techniques," *Society of Photo-Optical Instrumentation Engineers (SPIE) Conference Series*, vol. 74, pp. 120–125, 1976.

[68] S. M. Pizer, E. P. Amburn, J. D. Austin, R. Cromartie, A. Geselowitz, T. Greer, B. T. H. Romeny, and J. B. Zimmerman, "Adaptive histogram equalization and its variations," *Computer Vision, Graphics, and Image Processing*, vol. 39, no. 3, pp. 355–368, 1987.

[69] Lucchese, S. K. Mitra, and S. Barbara, "Color image segmentation: A State-of-the-Art survey," *Citeseer*, vol. 67, no. 2, pp. 207–221, 2001.

[70] H.-C. Chen, W.-J. Chien, and S.-J. Wang, "Contrast-based color image segmentation," *IEEE Signal Processing Letters*, vol. 11, pp. 641 – 644, July 2004.

[71] Y. Kuan, C. Kuo, and N. Yang, "Color-Based image salient region segmentation using novel region merging strategy," *Multimedia, IEEE Transactions on*, vol. 10, pp. 832 – 845, Aug. 2008.

[72] D. Comaniciu and P. Meer, "Mean shift: a robust approach toward feature space analysis," *IEEE Transactions on Pattern Analysis and Machine Intelligence*, vol. 24, pp. 603– 619, May 2002.

[73] J. Shi and J. Malik, "Normalized cuts and image segmentation," *IEEE Transactions on Pattern Analysis and Machine Intelligence*, vol. 22, pp. 888–905, Aug. 2000.

[74] C. Carson, S. Belongie, H. Greenspan, and J. Malik, "Blobworld: image segmentation using expectation-maximization and its application to image querying," *IEEE Transactions on Pattern Analysis and Machine Intelligence*, vol. 24, pp. 1026– 1038, Aug. 2002.

[75] J. Gauch, "Image segmentation and analysis via multiscale gradient watershed hierarchies," *IEEE Transactions on Image Processing*, vol. 8, pp. 69–79, Jan. 1999.

[76] W. Ma and B. S. Manjunath, "EdgeFlow: a technique for boundary detection and image segmentation," *IEEE Transactions on Image Processing*, vol. 9, pp. 1375–1388, Aug. 2000.

[77] G. Iannizzotto and L. Vita, "Fast and accurate edge-based segmentation with no contour smoothing in 2-D real images," *IEEE Transactions on Image Processing*, vol. 9, pp. 1232–1237, July 2000.

[78] H. Cheng, X. Jiang, and J. Wang, "Color image segmentation based on homogram thresholding and region merging," *Pattern Recognition*, vol. 35, pp. 373–393, Feb. 2002.

[79] K. S. Chenaoua, A. Bouridane, and F. Kurugollu, "Unsupervised histogram based color image segmentation," in *Proceedings of the 2003 10th IEEE International Conference on Electronics, Circuits and Systems, 2003. ICECS 2003*, vol. 1, pp. 240– 243 Vol.1, IEEE, Dec. 2003.

[80] S. Cheng, "Region-growing approach to colour segmentation using 3-D clustering and relaxation labelling," *IEE Proceedings - Vision, Image, and Signal Processing*, vol. 150, no. 4, p. 270, 2003.

[81] Y. Chang and X. Li, "Adaptive image region-growing," *IEEE Transactions on Image Processing*, vol. 3, pp. 868–872, Nov. 1994.

[82] M. D. G. Montoya, C. Gil, and I. Garcia, "The load unbalancing problem for region growing image segmentation algorithms," *Journal of Parallel and Distributed Computing*, vol. 63, pp. 387–395, Apr. 2003.

[83] S. Y. Wan and W. E. Higgins, "Symmetric region growing," *IEEE Transactions on Image Processing*, vol. 12, pp. 1007– 1015, Sept. 2003.

[84] J. F. Haddon and J. F. Boyce, "Image segmentation by unifying region and boundary information," *IEEE Transactions on Pattern Analysis and Machine Intelligence*, vol. 12, pp. 929–948, Oct. 1990.

[85] T. Pavlidis and Y. T. Liow, "Integrating region growing and edge detection," *IEEE Transactions on Pattern Analysis and Machine Intelligence*, vol. 12, pp. 225–233, Mar. 1990.

[86] C. Chu and J. K. Aggarwal, "The integration of image segmentation maps using region and edge information," *IEEE Transactions on Pattern Analysis and Machine Intelligence*, vol. 15, pp. 1241–1252, Dec. 1993.

[87] M. Wani and B. Batchelor, "Edge-region-based segmentation of range images," *IEEE Transactions on Pattern Analysis and Machine Intelligence*, vol. 16, pp. 314–319, Mar. 1994.

[88] N. Ahuja, "A transform for multiscale image segmentation by integrated edge and region detection," *IEEE Transactions on Pattern Analysis and Machine Intelligence*, vol. 18, pp. 1211–1235, Dec. 1996.

[89] J. Fan, D. K. Yau, A. K. Elmagarmid, and W. G. Aref, "Automatic image segmentation by integrating color-edge extraction and seeded region growing," *IEEE Transactions on Image Processing*, vol. 10, pp. 1454–1466, Oct. 2001.

[90] T. Gevers, "Adaptive image segmentation by combining photometric invariant region and edge information," *IEEE Transactions on Pattern Analysis and Machine Intelligence*, vol. 24, pp. 848–852, June 2002.

[91] A. Tremeau and P. Colantoni, "Regions adjacency graph applied to color image segmentation," *IEEE Transactions on Image Processing*, vol. 9, pp. 735–744, Apr. 2000.

[92] P. F. Felzenszwalb and D. P. Huttenlocher, "Efficient Graph-Based image segmentation," *Int. J. Comput. Vision*, vol. 59, p. 167181, Sept. 2004.

[93] D. Comaniciu and P. Meer, "Robust analysis of feature spaces: color image segmentation," in *, 1997 IEEE Computer Society Conference on Computer Vision and Pattern Recognition, 1997. Proceedings*, pp. 750–755, IEEE, June 1997.

[94] E. J. Pauwels and G. Frederix, "Finding salient regions in images : Non-Parametric clustering for image segmentation and grouping," *Computer Vision and Image Understanding*, vol. 75, no. 1-2, pp. 73–85, 1999.

[95] Y. Deng and B. S. Manjunath, "Unsupervised segmentation of color-texture regions in images and video," *IEEE Transactions on Pattern Analysis and Machine Intelligence*, vol. 23, pp. 800–810, Aug. 2001.

[96] W. Zhao and R. Chellappa, *Face Processing: Advanced Modeling and Methods*. Elsevier, Dec. 2006.

[97] C. R. Brice and C. L. Fennema, "Scene analysis using regions," *Artificial Intelligence*, vol. 1, no. 34, pp. 205–226, 1970.

[98] M. D. Heath, S. Sarkar, I. C. Society, T. Sanocki, K. W. Bowyer, and S. Member, "A robust visual method for assessing the relative performance of edge-detection algorithms," *IEEE Transactions on Pattern Analysis and Machine Intelligence*, vol. 19, pp. 1338–1359, 1997.

[99] R. Adams and L. Bischof, "Seeded region growing," *IEEE Transactions on Pattern Analysis and Machine Intelligence*, vol. 16, pp. 641–647, June 1994.

[100] M. Kass, A. Witkin, and D. Terzopoulos, "Snakes: Active contour models," *International Journal of Computer Vision*, vol. 1, pp. 321–331, Jan. 1988.

[101] D. J. Williams and M. Shah, "A fast algorithm for active contours and curvature estimation," *CVGIP: Image Underst.*, vol. 55, pp. 14–26, Jan. 1992.

[102] K. M. Lam and H. Yan, "Locating head boundary by snakes," in *, 1994 International Symposium on Speech, Image Processing and Neural Networks, 1994. Proceedings, IS-SIPNN '94*, pp. 17–20 vol.1, IEEE, Apr. 1994.

[103] A. R. Mirhosseini and H. Yan, "An optimally fast greedy algorithm for active contours," in *, Proceedings of 1997 IEEE International Symposium on Circuits and Systems, 1997. ISCAS '97*, vol. 2, pp. 1189–1192 vol.2, IEEE, June 1997.

[104] C. Xu and J. L. Prince, "Snakes, shapes, and gradient vector flow," *IEEE Transactions on Image Processing*, vol. 7, pp. 359–369, Mar. 1998.

[105] K. M. Lam and H. Yan, "Fast greedy algorithm for active contours," *Electronics Letters*, vol. 30, pp. 21–23, Jan. 1994.

[106] C. Chuang and W. Lie, "A downstream algorithm based on extended gradient vector flow field for object segmentation," *IEEE Transactions on Image Processing*, vol. 13, pp. 1379–1392, Oct. 2004.

[107] T. F. Chan and L. A. Vese, "Active contours without edges," *IEEE Transactions on Image Processing*, vol. 10, pp. 266–277, Feb. 2001.

[108] A. A. Amini, T. E. Weymouth, and R. C. Jain, "Using dynamic programming for solving variational problems in vision," *IEEE Transactions on Pattern Analysis and Machine Intelligence*, vol. 12, pp. 855–867, Sept. 1990.

[109] A. A. Amini, S. Tehrani, and T. E. Weymouth, "Using dynamic programming for minimizing the energy of active contours in the presence of hard constraints," in , *Second International Conference on Computer Vision*, pp. 95–99, IEEE, Dec. 1988.

[110] L. D. Cohen, "On active contour models and balloons," *CVGIP: Image Underst.*, vol. 53, pp. 211–218, Mar. 1991.

[111] L. D. Cohen and I. Cohen, "Finite element methods for active contour models and balloons for 2D and 3D images," *IEEE Transactions on Pattern Analysis and Machine Intelligence*, vol. 15, pp. 1131—1147, 1993.

[112] V. Caselles, R. Kimmel, and G. Sapiro, "Geodesic active contours," *Int. J. Comput. Vision*, vol. 22, p. 6179, Feb. 1997.

[113] J. Deng and H. T. Tsui, "A fast level set method for segmentation of low contrast noisy biomedical images," *Pattern Recogn. Lett.*, vol. 23, p. 161169, Jan. 2002.

[114] S. Osher and J. A. Sethian, "Fronts propagating with curvature dependent speed: Algorithms based on Hamilton-Jacobi formulations," *JOURNAL OF COMPUTATIONAL PHYSICS*, vol. 79, no. 1, pp. 12—49, 1988.

[115] S. Osher and R. P. Fedkiw, "Level set methods: An overview and some recent results," *Journal of Computational Physics*, vol. 169, no. 2, pp. 463–502, 2001.

[116] F. Precioso and M. Barlaud, "B-spline active contour with handling of topology changes for fast video segmentation," *EURASIP J. Appl. Signal Process.*, vol. 2002, p. 555560, Jan. 2002.

[117] G. Sapiro and A. Tannenbaum, "Affine invariant scale-space," *International Journal of Computer Vision*, vol. 11, pp. 25–44, Aug. 1993.

[118] M. F., C. Heneghan, and J. P. Thiran, "Identification of the optic disk boundary in retinal images using active contours," in *Irish Machine Vision and Image Processing Conference*, pp. 103–115, 1999.

[119] C. Lu, T. B. Tang, F. M. Alan, A. Laude, and B. Dhillon, "Automatic parapapillary atrophy shape detection and quantification in colour fundus images," in *2010 IEEE Biomedical Circuits and Systems Conference (BioCAS)*, pp. 86–89, IEEE, Nov. 2010.

[120] C. Lu, T. B. Tang, A. Laude, I. J. Deary, B. Dhillon, and A. F. Murray, "Quantification of parapapillary atrophy and optic disc," *Investigative Ophthalmology & Visual Science*, vol. 52, pp. 4671 –4677, June 2011.

[121] Y. Tang, X. Li, A. von Freyberg, and G. Goch, "Automatic segmentation of the papilla in a fundus image based on the C-V model and a shape restraint," in *18th International Conference on Pattern Recognition, 2006. ICPR 2006*, vol. 1, pp. 183–186, IEEE.

[122] V. F. Leavers, *Shape Detection in Computer Vision Using the Hough Transform*. Springer-Verlag, Dec. 1992.

[123] I. J. Yuen H.K. and K. J., "Shape using volumetric. primitives," *Image and Vision Computing*, vol. 1, no. 7, pp. 31–37, 1970.

[124] A. Fitzgibbon, M. Pilu, and R. B. Fisher, "Direct least square fitting of ellipses," *IEEE Transactions on Pattern Analysis and Machine Intelligence*, vol. 21, pp. 476–480, May 1999.

[125] R. M. Haralick and L. G. Shapiro, *Computer and Robot Vision*. Prentice Hall, June 2002.

[126] S. Arya, D. M. Mount, N. S. Netanyahu, R. Silverman, and A. Y. Wu, "An optimal algorithm for approximate nearest neighbor searching fixed dimensions," *J. ACM*, vol. 45, p. 891923, Nov. 1998.

[127] J. V. Soares, J. J. Leandro, R. M. Cesar, H. F. Jelinek, and M. J. Cree, "Retinal vessel segmentation using the 2-D gabor wavelet and supervised classification," *IEEE Transactions on Medical Imaging*, vol. 25, pp. 1214–1222, Sept. 2006.

[128] D. Marin, A. Aquino, M. E. Gegundez-Arias, and J. M. Bravo, "A new supervised method for blood vessel segmentation in retinal images by using Gray-Level and moment Invariants-Based features," *IEEE Transactions on Medical Imaging*, vol. 30, pp. 146–158, Jan. 2011.

[129] X. You, Q. Peng, Y. Yuan, Y.-m. Cheung, and J. Lei, "Segmentation of retinal blood vessels using the radial projection and semi-supervised approach," *Pattern Recognition*, vol. 44, pp. 2314–2324, Nov. 2011.